B U L L E T I N

DE LA SOCIÉTÉ DES SCIENCES ET DES LETTRES DE ŁÓDŹ

SÉRIE:
RECHERCHES SUR LES DÉFORMATIONS

Volume LXIII, no. 2

B U L L E T I N

DE LA SOCIÉTÉ DES SCIENCES ET DES LETTRES DE ŁÓDŹ

SÉRIE:
RECHERCHES SUR LES DÉFORMATIONS

Volume LXIII, no. 2

ŁÓDŹ 2013

ŁÓDZKIE TOWARZYSTWO NAUKOWE
PL-90-505 Łódź, ul. M. Curie-Skłodowskiej 11
tel. (42) 66-55-459, fax (42) 66 55 464
sprzedaż wydawnictw: tel. (42) 66 55 448, http://sklep.ltn.lodz.pl
e-mail: biuro@ltn.lodz.pl; http://www.ltn.lodz.pl/

**Wydano z pomocą finansową Ministerstwa Nauki
i Szkolnictwa Wyższego**

PL ISSN 0459–6854

Wydanie 1.
Nakład 200 egz.
Skład komputerowy: Zofia Fijarczyk
Druk i oprawa: Drukarnia Wojskowa
Łódź, ul. Gdańska 130
tel. +48 42 6366171

The journal appears in the bases *Copernicus* and *EBSCOhost*

INSTRUCTION AUX AUTEURS

1. La présente Série du Bulletin de la Société des Sciences et des Lettres de Łódź comprend des communications du domaine des mathématiques, de la physique ainsi que de leurs applications liées aux déformations au sense large.
2. Toute communications est présentée à la séance d'une Commission de la Société par un des members (avec deux opinions de spécialistes designés par la Rédaction). Elle doit lui être adressée directement par l'auteur.
3. L'article doit être écrit en anglais, français, allemand ou russe et débuté par un résumé en anglais ou en langue de la communication présentée. Dans tous les travaux écrits par des auteurs étrangers le titre et le résumé en polonais seront préparés par la rédaction. Il faut fournir le texte original qui ne peut contenir plus de 15 pages (plus 2 copies).
4. Comme des articles seront reproduits par un procédé photographique, les auteurs sont priés de les préparer avec soin. Le texte tapé sur un ordinateur de la classe IBM PC avec l'utilisation d'un imprimante de laser, est absolument indispensable. Il doit être tapé préférablement en *AMS-TEX* ou, exceptionnellement, en *Plain-TEX* ou *LATEX*. Après l'acceptation de texte les auteurs sont priés d'envoyer les disquettes (PC). Quelle que soient les dimensions des feuilles de papier utilisées, le texte ne doit pas dépasser un cadre de frappe de 12.3×18.7 cm (0.9 cm pour la page courante y compris). Les deux marges doivent être le la même largeur.
5. Le nom de l'auteur (avec de prénom complet), écrit en italique sera placé à la 1ère page, 5.6 cm au dessous du bord supérieur du cadre de frappe; le titre de l'acticle, en majuscules d'orateur 14 points, 7.1 cm au dessous de même bord.
6. Le texte doit être tapé avec les caractères Times 10 points typographiques et l'interligne de 14 points hors de formules longues. Les résumés, les rénvois, la bibliographie et l'adresse de l'auteurs doivent être tapés avec le petites caractères 8 points typographiques et l'interligne de 12 points. Ne laissez pas de "blancs" inutiles pour respecter la densité du texte. En commençant le texte ou une formule par l'alinéa il faut taper 6 mm ou 2 cm de la marge gauche, respectivement.
7. Les texte des thèorémes, propositions, lemmes et corollaries doivent être écrits en italique.
8. Les articles cités seront rangés dans l'ordre alphabétique et précédés de leurs numéros placés entre crochets. Après les références, l'auteur indiquera son adress complète.
9. Envoi par la poste: protégez le manuscript à l'aide de cartons.
10. Les auteurs recevront une copie de fascicule correspondant à titre gratuit.

Adresse de la Rédaction de la Série:
Département de la Physique d'etat solide
de l'Université de Łódź
Pomorska 149/153, PL-90-236 Łódź, Pologne

Name and surname of the authors

TITLE – INSTRUCTION FOR AUTHORS SUBMITTING THE PAPERS FOR BULLETIN

Summary

Abstract should be written in clear and concise way, and should present all the main points of the paper. In particular, new results obtained, new approaches or methods applied, scientific significance of the paper and conclusions should be emphasized.

1. General information

The paper for BULLETIN DE LA SOCIÉTÉ DES SCIENCES ET DES LETTRES DE ŁÓDŹ should be written in LaTeX, preferably in LaTeX 2e, using the style (the file **bull.cls**).

2. How to prepare a manuscript

To prepare the LaTeX 2e source file of your paper, copy the template file **instr.tex** with **Fig1.eps**, give the title of the paper, the authors with their affiliations/addresses, and go on with the body of the paper using all other means and commands of the standard class/style 'bull.cls'.

2.1. Example of a figure

Figures (including graphs and images) should be carefully prepared and submitted in electronic form (as separate files) in Encapsulated PostScript (EPS) format.

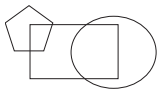

Fig. 1: The figure caption is located below the figure itself; it is automatically centered and should be typeset in small letters.

2.2. Example of a table

Tab. 1: The table caption is located above the table itself; it is automatically centered and should be typeset in small letters.

Description 1	Description 2	Description 3	Description 4
Row 1, Col 1	Row 1, Col 2	Row 1, Col 3	Row 1, Col 4
Row 2, Col 1	Row 2, Col 2	Row 2, Col 3	Row 2, Col 4

2.3. "Ghostwriting" and "guest authorship" are strictly forbiden

The printed version of an article is primary (comparing with the electronic version). Each contribution submitted is sent for evaluation to two independent referees before publishing.

3. How to submit a manuscript

Manuscripts have to be submitted in electronic form, preferably via e-mail as attachment files sent to the address **zofija@uni.lodz.pl**. If a whole manuscript exceeds 2 MB composed of more than one file, all parts of the manuscript, i.e. the text (including equations, tables, acknowledgements and references) and figures, should be ZIP-compressed to one file prior to transfer. If authors are unable to send their manuscript electronically, it should be provided on a disk (DOS format floppy or CD-ROM), containing the text and all electronic figures, and may be sent by regular mail to the address: **Department of Solid State Physics, University of Lodz, Bulletin de la Société des Sciences et des Lettres de Łódź, Pomorska 149/153, 90-236 Łódź, Poland**.

References

[1]

Affiliation/Address

TABLE DES MATIÈRES

PL ISSN 0459-6854

B U L L E T I N

DE LA SOCIÉTÉ DES SCIENCES ET DES LETTRES DE ŁÓDŹ

2013 Vol. LXIII

Recherches sur les déformations no. 2

pp. 9–22

Lyubov V. Kulavets', Oksana M. Mulyava and Myroslav M. Sheremeta

ON BELONGING OF CHARACTERISTIC FUNCTIONS OF PROBABILITY LAWS TO A CONVERGENCE CLASS

Summary

It is investigated the condition on a probability law, under which its characteristic function belongs to a convergence class.

Keywords and phrases: probability law, characteristic function, convergence class

1. Introduction

A non-decreasing function F continuous on the left on $(-\infty, +\infty)$ is said [1, p. 10] to be a *probability law* if

$$\lim_{x\to+\infty} F(x) = 1 \quad \text{and} \quad \lim_{x\to-\infty} F(x) = 0,$$

and the function

$$\varphi(z) = \int_{-\infty}^{+\infty} e^{izx} dF(x)$$

defined for real z is called [1, p. 12] a *characteristic function* of this law. If φ has an analytic continuation on the disk $\mathbb{D}_R = \{z : |z| < R\}$, $0 < R \le +\infty$, then we call φ a characteristic function of the law F analytic in $\mathbb{D}_R$. Further we always assume that $\mathbb{D}_R$ is the maximal disk of the analyticity of φ. It is known [1, p. 37–38] that φ is a characteristic function of the law F analytic in $\mathbb{D}_R$ if and only if for every $r \in [0, R)$

$$W_F(x) =: 1 - F(x) + F(-x) = O(e^{-rx}), \quad x \to +\infty. \tag{1}$$

Hence it follows that

$$\varliminf_{x\to+\infty}\frac{1}{x}\ln\frac{1}{W_F(x)}=R. \tag{2}$$

For $0\le r<R$ we put $M(r,\varphi)=\max\{|\varphi(z)|:\ |z|=r\}$. If a characteristic function $\varphi\neq\text{const}$ is entire then [1, p. 45] there exists

$$\varlimsup_{r\to+\infty} r^{-1}\ln M(r,\varphi)>0,$$

that is φ has the growth not below of normal type of the order $\varrho=1$. Therefore, if we define a convergence class [2, p. 62] by condition

$$\int_{r_0}^{+\infty} r^{-(\varrho+1)}\ln M(r,\varphi)dr<+\infty, \tag{3}$$

we need to assume that $\varrho>1$. For the function φ analytic in $\mathbb{D}=\mathbb{D}_1$ of order

$$\varrho=\varlimsup_{r\uparrow 1}\frac{\ln\ln M(r,\varphi)}{-\ln(1-r)}>0$$

a *convergence class* is defined [3] by the condition

$$\int_{r_0}^{1}(1-r)^{\varrho-1}\ln M(r,\varphi)dr<+\infty. \tag{4}$$

As $\varrho=2$ this condition is sufficient [4, p. 50] in order that φ belongs to the class of MacLane.

In the paper [5] it is asserted that an entire characteristic function φ of the order $\varrho>1$ of the probability law F belongs to convergence class if and only if

$$\int_{x_0}^{+\infty}\left(\frac{1}{x}\ln\frac{1}{W_F(x)}\right)^{1-\varrho}dx<+\infty. \tag{5}$$

For a characteristic function φ of the order $\varrho>0$ analytic in $\mathbb{D}$ in [6] is proved that in order that φ belongs to convergence class it is necessary and, in the case when the function

$$v(x)=\ln\frac{1}{W_F(x)}$$

is continuously differentiable and v' increases, it is sufficient that

$$\int_{x_0}^{+\infty}\left\{\left(1+\frac{1}{x}\ln W_F(x)\right)^{+}\right\}^{\varrho+1}dx<+\infty. \tag{6}$$

Here we examine a problem of the belonging of analytic characteristic function of probability law to a convergence Φ-class, which is considered in the papers [7–9]. For this purpose we have to use the next lemma.

Lemma 1. *If φ is a characteristic function of probability law F analytic in $\mathbb{D}_R$, $0<R\le+\infty$ then for every $r\in[0,R)$ and all $x\ge 0$ the following inequalities are true:*

$$W_F(x)e^{xr}\le 2M(r,\varphi)$$

and

$$M(r,\varphi) \le r\int\limits_0^\infty W_F(x)e^{xr}dx + 1 + W_F(+0).$$

For $R = +\infty$ these inequalities are proved in [1, pp. 54–55] and for $R < +\infty$ the proof is analogous.

We put

$$\mu(r,\varphi) = \sup\{W_F(x)e^{xr} : x \ge 0\}$$

and

$$I(r,\varphi) = \int\limits_0^\infty W_F(x)e^{xr}dx$$

and suppose that $M(r,\varphi) \uparrow +\infty$ as $r \uparrow R$. Then by Lemma 1

$$\ln \mu(r,\varphi) \le (1+o(1)) \ln M(r,\varphi) \le (1+o(1)) \ln I(r,\varphi), \quad r \uparrow R. \tag{7}$$

Therefore, the problem of belonging of $\ln M(r,\varphi)$ to that or other convergence class is transferred to the problem of belonging of $\ln \mu(r,\varphi)$ to this convergence class and the estimates $I(r,\varphi)$ by $\mu(r,\varphi)$.

2. Properties of the function $\ln \mu(r,\varphi)$

It is clear that $W_F(x) \searrow 0$ $(x \to +\infty)$. Therefore, if $R = +\infty$ and $x_0 = \sup\{x : W_F(x) > 0\} < +\infty$ then

$$\mu(r,\varphi) = \sup\{W_F(x)e^{xr} : 0 \le x \le x_0\} \le W_F(0)e^{x_0 r}$$

and since $\mu(r,\varphi) \ge W_F(x_0)e^{x_0 r}$ we have

$$\lim_{r\to+\infty} r^{-1} \ln \mu(r,\varphi) = x_0.$$

If $R = +\infty$ and $W_F(x) > 0$ for all $x \ge 0$ then

$$\lim_{r\to+\infty} r^{-1} \ln \mu(r,\varphi) = +\infty.$$

If $R < +\infty$ then the function $\ln \mu(r,\varphi)$ may be bounded. It is easy to show that $\mu(r,\varphi) \le K < +\infty$ for all $r \in [0, R)$ if and only if $W_F(x)e^{xR} \le K < +\infty$ for all $x \ge 0$. Thus, $\mu(r,\varphi) \uparrow +\infty$ as $r \uparrow R$ if and only if

$$\overline{\lim_{x\to+\infty}} W_F(x)e^{xR} = +\infty. \tag{8}$$

From the definition of $\mu(r,\varphi)$ it follows that the function $\ln \mu(r,\varphi)$ is convex on $[0, R)$.

For $r \in [0, R)$ and $\varepsilon > 0$ we put

$$\nu(r,\varphi;\varepsilon) = \sup\{x \ge 0 : \ln W_F(x) + rx \ge \ln \mu(r,\varphi) - \varepsilon\}.$$

Clearly, for fixed $r \in [0, R)$ the function $\nu(r, \varphi; \cdot)$ is nondecreasing on $(0, +\infty)$. Therefore, there exists a quantity

$$\nu(r, \varphi) = \lim_{\varepsilon \downarrow 0} \nu(r, \varphi; \varepsilon).$$

Lemma 2. *The function ν is nondecreasing on $[0, R)$ and $(\ln \mu(r, \varphi))' = \nu(r, \varphi)$ for all $r \in (0, R)$ with the exception of an at most countable set.*

Proof. At first we prove that for arbitrary $r \in (0, R)$ and $\varepsilon > 0$ the set

$$E(r, \varepsilon) = \{x \geq 0 : |x - \nu(r, \varphi)| < \varepsilon, \ln W_F(x) + rx \geq \ln \mu(r, \varphi) - \varepsilon\}$$

is non-empty. Indeed, for fixed $r \in (0, R)$ and $\varepsilon > 0$ there exists $\delta \in (0, \varepsilon)$ such that

$$|\nu(r, \varphi) - \sup\{x \geq 0 : \ln W_F(x) + \sigma x \geq \ln \mu(r, \varphi) - \delta\}| < \varepsilon/2 \tag{9}$$

and there exists $x_0 \geq 0$ such that

$$\ln f(x_0) + \sigma x_0 \geq \ln \mu(r, \varphi) - \delta \tag{10}$$

and

$$|x_0 - \sup\{x \geq 0 : \ln f(x) + rx \geq \ln \mu(r, \varphi) - \delta\}| < \varepsilon/2. \tag{11}$$

From (9)–(11) we obtain

$$|x_0 - \nu(r, \varphi)| < \varepsilon, \quad \ln W_F(x_0) + rx_0 \geq \ln \mu(r, \varphi) - \varepsilon,$$

that is $x_0 \in E(r, \varepsilon)$ and the set $E(r, \varepsilon)$ is non-empty.

Since $E(r, \varepsilon)$ is non-empty for arbitrary $r \in (0, R)$ and $\varepsilon > 0$, by the axiom of choice for each $\varepsilon > 0$ there exists a function $\nu_\varepsilon(r) \geq 0$ such that for all $r \in (0, R)$

$$\ln \mu(r, \varphi) \geq \ln W_F(\nu_\varepsilon(r)) + r\nu_\varepsilon(r) \geq \ln \mu(r, \varphi) - \varepsilon \tag{12}$$

and

$$|\nu_\varepsilon(r) - \nu(r, \varphi)| < \varepsilon. \tag{13}$$

Suppose that $r_1, r_2 \in (0, R)$. By definition

$$\ln \mu(r_1, \varphi) \geq \ln W_F(\nu_\varepsilon(r_2)) + r_1\nu_\varepsilon(r_2). \tag{14}$$

From (12) we have

$$\ln \mu(r_2, \varphi) \leq \varepsilon + \ln W_F(\nu_\varepsilon(r_2)) + r_2\nu_\varepsilon(r_2), \tag{15}$$

and combining (14) and (14) we obtain

$$\ln \mu(r_2, \varphi) - \ln \mu(r_1, \varphi) \leq (r_2 - r)\nu_\varepsilon(r_2) + \varepsilon,$$

whence passing to the limit as $\varepsilon \to 0$ and taking into account (13) we get

$$\ln \mu(r_2, \varphi) - \ln \mu(r_1, \varphi) \leq (r_2 - r_1)\nu(r_2, \varphi). \tag{16}$$

Since r_1 and r_2 are arbitrary, we can interchange them and obtain also the inequality

$$\ln \mu(r_1, \varphi) - \ln \mu(r_2, \varphi) \leq (r_1 - r_2)\nu(r_1, \varphi). \tag{17}$$

Suppose that $r_1 < r_2$. Then from (16) and (17) we get

$$\nu(r_1,\varphi) \le \frac{\ln \mu(r_2,\varphi) - \ln \mu(r_1,\varphi)}{r_2 - r_1} \le \nu(r_2,\varphi). \tag{18}$$

Inequality (18) implies that the function $\nu(r,\varphi)$ is nondecreasing and, thus, continuous with the exception of an at most countable set of points. Passing to the limit in (18) as $r_1 \to r_2$ (and afterwards $r_2 \to r_1$), we obtain the equality $(\ln \mu(r,\varphi))' = \nu(r,\varphi)$. Lemma 2 is proved.

This lemma implies the following result.

Corollary 1. *For all* $0 < r_0 < r < R$

$$\ln \mu(r,\varphi) = \ln \mu(r_0,\varphi) + \int_{r_0}^{r} \nu(x,\varphi)dx. \tag{19}$$

From (19) it follows that if $\mu(r,\varphi) \uparrow +\infty$ as $r \uparrow R$; then $\nu(r,\varphi) \nearrow +\infty$ as $r \uparrow R$, and (12) implies for each $\varepsilon > 0$ and all $r \in (0,\, R)$ the inequality

$$\frac{1}{\nu_\varepsilon(r,\varphi)} \ln \frac{1}{W_F(\nu_\varepsilon(r,\varphi))} \le r - \frac{\ln \mu(r,\varphi)}{\nu_\varepsilon(r,\varphi)} \le r$$

whence in view of the arbitrariness of ε we obtain

$$\frac{1}{\nu(r,\varphi)} \ln \frac{1}{W_F(\nu(r,\varphi))} \le r. \tag{20}$$

By $V(R)$ we denote a class of positive continuously differentiable on $(0,+\infty)$ function v such that $v'(x) \uparrow R$ as $x \to +\infty$. If

$$\ln \frac{1}{W_F(x)} = v(x) \in V(R)$$

then for every $r \in (0,\, R)$ the function $\ln W_F(x) + rx = -v(x) + rx$ has a unique point of the maximum $x = \nu(r,\varphi)$, which is increasing and continuous on $(0,\, R)$, and

$$\ln \mu(r,\varphi) = \max\{\ln W_F(x) + rx :\, x \ge 0\} = \ln W_F(\nu(r,\varphi)) + r\nu(r,\varphi). \tag{21}$$

3. Belonging of $\ln \mu(r,\varphi)$ to a convergence Φ-class

Let $0 < R \le +\infty$ and $\Omega(R)$ be a class of positive functions Φ unbounded on $(0,R)$ such that the derivative Φ' is positive, continuously differentiable and increasing to $+\infty$ on $(0,R)$. For $\Phi \in \Omega(R)$ we denote by ϕ the inverse function to Φ', and let

$$\Psi(r) = r - \frac{\Phi(r)}{\Phi'(r)}$$

be the function associated with Φ in the sense of Newton. As in [7], it is possible to show that the function Ψ is continuously differentiable and increasing to R on $(0,R)$ and the function ϕ is continuously differentiable and increasing to R on $(0,+\infty)$.

As in [8–10], we say that $\ln \mu(r,\varphi)$ *belongs to a convergence* Φ*-class* if

$$\int_{r_0}^{R} \frac{\Phi'(r)\ln \mu(r,\varphi)}{\Phi^2(r)}dr < +\infty. \tag{22}$$

Proposition 1. *Let*

$$0 < R \le +\infty, \qquad \Phi \in \Omega(R)$$

and

$$\frac{\Phi''(r)\Phi(r)}{(\Phi'(r))^2} \ge h > 0, \quad r \in [r_0,\, R), \tag{23}$$

and φ *be a characteristic function on probability law* F *analytic in* $\mathbb{D}_R$ *such that*

$$\ln \frac{1}{W_F(x)} = v(x) \in V(R).$$

If

$$\int_{x_0}^{\infty} \frac{dx}{\Phi'\left(\dfrac{1}{x}\ln \dfrac{1}{W_F(x)}\right)} < +\infty; \tag{24}$$

then $\ln \mu(r,\varphi)$ *belongs to a convergence* Φ*-class.*

Proof. At first we remark that the condition $v(x) \in V(R)$ implies the correlation $v(x) = (1+o(1))xR$ as $x \to +\infty$, that is

$$\frac{1}{x}\ln \frac{1}{W_F(x)} = (1+o(1))R \quad \text{as} \quad x \to +\infty$$

and the condition (2) holds.

From (23) it follows that

$$\int_{r_0}^{R} \frac{dr}{\Phi(r)} \le \frac{1}{h}\int_{r_0}^{R} \frac{\Phi''(r)dr}{(\Phi'(r))^2} = \frac{1}{h\Phi'(r_0)} < +\infty.$$

We put

$$B(x) = \int_{x}^{R} \frac{dr}{\Phi(r)}.$$

Then

$$B(x) \downarrow 0 \quad \text{as} \quad x \uparrow R, \quad B(x) \le \frac{1}{h\Phi'(x)},$$

and (24) implies

$$\int_{x_0}^{+\infty} B\left(\frac{1}{x}\ln \frac{1}{W_F(x)}\right)dx < +\infty. \tag{25}$$

From the condition

$$\ln \frac{1}{W_F(x)} = v(x) \in V(R)$$

it follows that there exists a function $\nu(r) = \nu(r, \varphi)$ increasing and continuous on $(0, R)$ such that (20) holds, and in view of (25) and decreasing of B

$$\int_{r_0}^{R} B(r)d\nu(r) \le \int_{r_0}^{R} B\left(\frac{1}{\nu(r)} \ln \frac{1}{W_F(\nu(r))}\right) d\nu(r) < +\infty. \tag{26}$$

But

$$+\infty > \int_{r_0}^{R} B(r)d\nu(r) = B(r)\nu(r)\Big|_{r_0}^{R} - \int_{r_0}^{R} \nu(r)B'(r)dr \ge \text{const} + \int_{r_0}^{R} \frac{\nu(r)}{\Phi(r)}dr.$$

Therefore, in view of (19)

$$\int_{r_0}^{R} \frac{\Phi'(r) \ln \mu(r, \varphi)}{\Phi^2(r)}dr = \int_{r_0}^{R} \ln \mu(r, \varphi)d\left(-\frac{1}{\Phi(r)}\right) \le \text{const} + \int_{r_0}^{R} \frac{\nu(r, \varphi)}{\Phi(r)}dr < +\infty,$$

i.e. $\ln \mu(r, \varphi)$ belongs to a convergence Φ-class. Proposition 1 is proved.

Remark 1. We did not succeed to build an example indicative on importance of the condition

$$\ln \frac{1}{W_F(x)} = V(x) \in \Omega(+\infty).$$

It seems to us that it is superfluous, but for this purpose at least for the case of entire functions it is necessary to prove the following statement: *for every function* v_1 *such that* $v_1(x) \nearrow +\infty$ *and*

$$\frac{v_1(x)}{x} \to +\infty \quad \textit{as} \quad x \to +\infty$$

there exists a function $v \in V(R)$ *such that* $v_1(x) = O(v(x))$ *as* $x \to +\infty$ *and*

$$\sup\{-v(x) + xr : x \ge 0\} \le K \sup\{-v_1(x) + xr : x \ge 0\}$$

or

$$\sup\{-v(x) + xr : x \ge 0\} \le K \sup\{-v_1(x) + xKr : x \ge 0\},$$

where $K = \text{const} > 0$.

Proposition 2. *Let* $0 < R \le +\infty$, $\Phi \in \Omega(R)$, $\Phi'(r)/\Phi(r)$ *be a function, nondecreasing on* $[r_0, R)$, *and*

$$\frac{\Phi''(r)\Phi(r)}{(\Phi'(r))^2} \le H < +\infty, \quad r \in [r_0, R). \tag{27}$$

Suppose that φ *is a characteristic function on probability law* F *analytic in* $\mathbb{D}_R$ *such that* (8) *holds. If* $\ln \mu(r, \varphi)$ *belongs to a convergence* Φ*-class then* (24) *holds.*

Proof. Since the function $\Phi'(r)/\Phi(r)$ is nondecreasing on $[r_0, R)$, the function

$$\frac{\Phi'(r)\ln\mu(r,\varphi)}{\Phi(r)}$$

is continuous and increasing to $+\infty$ on $[r_0, R)$. Therefore, there exists a function $r(x)$ increasing to $+\infty$ and continuous on $(x_0, +\infty)$ such that

$$\frac{\Phi'(r(x))\ln\mu(r(x),\varphi)}{\Phi(r(x))} = x,$$

and since in view of (22)

$$\int\limits_{r_0}^{R}(l(r)/\Phi(r))dr < +\infty,$$

we obtain

$$\int\limits_{x_0}^{\infty}\frac{x}{\Phi(r(x))}dr(x) = \int\limits_{x_0}^{\infty}\frac{l(r(x))}{\Phi(r(x))}dr(x) < +\infty.$$

As above, let $B(r) = \int\limits_r^R \frac{dx}{\Phi(x)}$. Using the l'Hospital rule we have

$$\lim_{r\to R} B(r)\Phi(r) = \lim_{r\to R}\frac{\int\limits_r^R\frac{dx}{\Phi(x)}}{1/\Phi(r)} = \lim_{r\to R}\frac{\Phi(r)}{\Phi'(r)} < +\infty.$$

Therefore,

$$xB(r(x)) = \frac{\Phi'(r(x))\ln\mu(r(x),\varphi)}{\Phi(r(x))} =$$

$$= \Phi(r(x))B(r(x))\frac{\Phi'(r(x))\ln\mu(r(x),\varphi)}{\Phi^2(r(x))} = O(1), \quad x\to+\infty,$$

and

$$\int\limits_{x_0}^{\infty}B(r(x))dx = xB(r(x))\Big|_{x_0}^{+\infty} - \int\limits_{x_0}^{\infty}xdB(r(x)) = \text{const} + \int\limits_{x_0}^{\infty}\frac{x}{\Phi(r(x))}dr(x) < +\infty.$$

From (27) it follows that

$$B(r) = \int\limits_r^R\frac{dr}{\Phi(r)} \geq \frac{1}{H}\int\limits_r^R\frac{\Phi''(r)dr}{(\Phi'(r))^2} = \frac{1}{H\Phi'(r)}.$$

Therefore,

$$\int\limits_{x_0}^{\infty}\frac{dx}{\Phi'(r(x))} < +\infty. \tag{28}$$

But $\ln\mu(r(x),\varphi) \geq \ln W_F(x) + xr(x)$, that is

$$r(x) \leq \frac{\ln\mu(r(x),\varphi)}{x} + \frac{1}{x}\ln\frac{1}{W_F(x)} = \frac{\Phi(r(x))}{\Phi'(r(x))} + \frac{1}{x}\ln\frac{1}{W_F(x)},$$

whence

$$\Psi(r(x)) \le \frac{1}{x} \ln \frac{1}{W_F(x)}.$$

For some $\xi = \xi(r)$ we have

$$0 \le \ln \Phi'(r) - \ln \Phi'(\Psi(r)) = \frac{\Phi''(\xi)}{\Phi'(\xi)}(r - \Psi(r)) = \frac{\Phi''(\xi)}{\Phi'(\xi)} \frac{\Phi(r)}{\Phi'(r} \le \frac{\Phi''(\xi)\Phi(\xi)}{(\Phi'(\xi))^2} \le H$$

i.e. $\Phi'(r) = O(\Phi'(\Psi(r)))$ as $r \uparrow R$ and, thus,

$$\Phi'(r(x)) \le K\Phi'(\Psi(r(x))) \le K\Phi' \left(\frac{1}{x} \ln \frac{1}{W_F(x)} \right),$$

where $K = \text{const} > 0$. Hence and from (28) we obtain (24). Proposition 2 is proved.

Remark 2. Let

$$0 < R < +\infty \quad \text{and} \quad \Phi(r) = A\left(\frac{1}{R - r} \right).$$

Then the function $\Phi'(r)/\Phi(r)$ is nondecreasing on $[r_0, R)$ if and only if the function $x^2 A'(x)/A(x)$ is nondecreasing on $[x_0, +\infty)$. The latter condition does not influence A on speed of growth but influences its smoothness. If $R = +\infty$ the function $\Phi'(r)/\Phi(r)$ is nondecreasing on $[r_0, R)$ if Φ does not increase slower than the exponential function. For the power functions this condition does not hold. It seems to us that the condition $\Phi'(r)/\Phi(r) \nearrow$ may be replaced by the condition $(\Phi'(r))^{1+\eta}/\Phi(r) \nearrow$ for some $\eta \in [0, 1)$.

4. Estimates of $\ln I(r, \varphi)$ by $\ln \mu(r, \varphi)$

We suppose that $\Phi \in \Omega(R)$ and

$$\Phi'(r) > \frac{1}{R - r}, \quad r_0 < r < R. \tag{29}$$

Then $r + 1/\Phi'(r) < R$,

$$I(r, \varphi) = \int_0^\infty W_F(x) e^{xr} dx = \int_0^\infty W_F(x) \exp\{x(r + 1/\Phi'(r))\} \exp\{x/\Phi'(r)\} dx \le$$

$$\le \mu(r + 1/\Phi'(r), \varphi)\Phi'(r)$$

and

$$\ln I(r, \varphi) \le \ln \mu(r + 1/\Phi'(r), \varphi) + \ln \Phi'(r)$$

for all $r_0 < r < R$. Therefore, if

$$\int_{r_0}^R \frac{\Phi'(r) \ln \Phi'(r)}{\Phi^2(r)} dr < +\infty, \tag{30}$$

then

$$\int\limits_{r_0}^{R} \frac{\Phi'(r)\ln\, I(r,\varphi)}{\Phi^2(r)}dr \le \int\limits_{r_0}^{R} \frac{\Phi'(r)\ln\, \mu(r+1/\Phi'(r),\varphi)}{\Phi^2(r)}dr + \text{const}.$$

Using this inequality it is easy to prove following proposition.

Proposition 3. *Let* $0 < R \le +\infty$, $\Phi \in \Omega(R)$, *the conditions* (27), (29), (30) *hold and* $\Phi'(r+1/\Phi'(r)) \le H_1\Phi'(r)$ *for all* $r \in [r_0,\, R)$, *where* $H_1 = \text{const} > 0$. *Let* φ *be a characteristic function on probability law* F *analytic in* $\mathbb{D}_R$. *If* $\ln\, \mu(r,\varphi)$ *belongs to a convergence* Φ*-class then* $\ln\, I(r,\varphi)$ *belongs to such class as well.*

Proof. Since $\Phi'(r+1/\Phi'(r)) \le H_1\Phi'(r))$, we have in view of (27) for some $\xi = \xi(r) \in (r,\, r+1/\Phi'(r))$

$$\left|\ln \frac{\Phi^2(r+1/\Phi'(r))}{\Phi'(r+1/\Phi'(r))} - \ln \frac{\Phi^2(r)}{\Phi'(r)}\right| = \left|2\frac{\Phi'(\xi)}{\Phi(\xi)} - \frac{\Phi''(\xi)}{\Phi'(\xi)}\right| \frac{1}{\Phi'(r)}$$

$$= \frac{\Phi'(\xi)}{\Phi(\xi)\Phi'(r)}\left|2 - \frac{\Phi''(\xi)\Phi(\xi)}{(\Phi'(\xi))^2}\right| \le H_1 \frac{\Phi'(\xi)}{\Phi(\xi)\Phi'(\xi)}\left|2 - \frac{\Phi''(\xi)\Phi(\xi)}{(\Phi'(\xi))^2}\right| \to 0, \quad r \uparrow R$$

that is

$$\frac{\Phi'(r)}{\Phi^2(r)} = (1+o(1))\frac{\Phi'(r+1/\Phi'(r))}{\Phi^2(r+1/\Phi'(r))}, \quad r \uparrow R.$$

From (27) it follows also that $\Phi''(r) = o((\Phi'(r))^2)$ as $r \uparrow R$, that is

$$1 - \Phi''(r)/(\Phi'(r))^2 \ge h_1 > 0.$$

Therefore, for some $r_1 \ge r_0$ in view of (30) we obtain

$$\int\limits_{r_1}^{R} \frac{\Phi'(r)\ln\, I(r,\varphi)}{\Phi^2(r)}dr \le \int\limits_{r_1}^{R} \frac{\Phi'(r)\ln\, \mu(r+1/\Phi'(r),\varphi)}{\Phi^2(r)}dr + \text{const}$$

$$\le 2\int\limits_{r_1}^{R} \frac{\Phi'(r+1/\Phi'(r))\ln\, \mu(r+1/\Phi'(r),\varphi)}{\Phi^2(r+1/\Phi'(r))} \frac{d(r+1/\Phi'(r))}{1-\Phi''(r)/(\Phi'(r))^2} + \text{const}$$

$$\le \frac{2}{h_1}\int\limits_{r_1}^{R} \frac{\Phi'(r+1/\Phi'(r))\ln\, \mu(r+1/\Phi'(r),\varphi)}{\Phi^2(r+1/\Phi'(r))} d(r+1/\Phi'(r)) + \text{const} < +\infty.$$

Proposition 3 is proved.

Remark 3. The condition (30) is significant. In [9] it is shown that this condition is near to necessary in order that the logarithms of the maximum modulus of an entire function and the maximal term of its power development belong to the same convergence Φ-class.

For $R = +\infty$ the inequality (29) is trivial. Clearly in the case $R < +\infty$ the condition (29) is natural.

Finally, the condition $\Phi'(r+1/\Phi'(r)) \le H_1\Phi'(r))$ for $r \in [r_0,\, R)$ is a condition on the smoothness of Φ'. If $R = +\infty$ then by Borel-Nevanlinna theorem [2, p. 120–121] $\Phi'(r+1/\Phi'(r)) \le (1+\varepsilon)\Phi'(r)$ for every $\varepsilon > 0$ and all $r \ge r_0$ outside of a set of finite measure.

5. Main result and colloraries

Hence we obtain a theorem on the belonging of the characteristic function φ of a probability law F analytic in $\mathbb{D}_R$ to convergence Φ-class, that is

$$\int\limits_{r_0}^{R} \frac{\Phi'(r)\ln\, M(r,\varphi)}{\Phi^2(r)}dr < +\infty.$$

At first we remark that if $\Phi'(r)/\Phi(r)$ be a function, nondecreasing on $[r_0,\, R)$ then $\Phi''(r)\Phi(r) - (\Phi'(r))^2 \ge 0$ and, thus, the condition (23) holds. Therefore, using the inequalities (7) from Propositions 1–3 we obtain the following main result:

Theorem. *Let $0 < R \le +\infty$, $\Phi \in \Omega(R)$, $\Phi'(r)/\Phi(r)$ be a function, nondecreasing on $[r_0,\, R)$, $\Phi'(r+1/\Phi'(r)) \le H_1\Phi'(r)$ for all $r \in [r_0,\, R)$, where $H_1 = \mathrm{const} > 0$, and the condition* (27) (29), (30) *hold. Suppose that φ is an analytic in $\mathbb{D}_R$ characteristic function on probability law F such that* (8) *holds.*

Then in order that φ belongs to a convergence Φ-class it is necessary and in the case, when

$$\ln\, \frac{1}{W_F(x)} = v(x) \in V(R),$$

it is sufficient that (24) *holds.*

We bring several colloraries to this theorem. At first we suppose that

$$0 < R < \infty, \quad 0 < \varrho < \infty \Phi(r) = (R-r)^{-\varrho}.$$

Then

$$\Phi'(r) = \varrho(R-r)^{-(\varrho+1)} > (R-r)^{-1}, \quad \frac{\Phi'(r)}{\Phi(r)} = \frac{1}{\varrho(R-r)} \uparrow +\infty \quad \text{as} \quad r \uparrow R,$$

$$\Phi'(r) > (R-r)^{-1}, \quad \Phi'(r+1/\Phi'(r)) = (1+o(1))\Phi'(r) \quad \text{as} \quad r \uparrow R$$

and

$$\Phi(r)\Phi''(r)(\Phi(r))^{-2} = \frac{\varrho+1}{\varrho}.$$

Thus, the fuction $\Phi(r) = (R-r)^{-\varrho}$ satisfies all conditions of the Theorem. We remark also that

$$\Phi'\left(\frac{1}{x}\ln\, \frac{1}{W_F(x)}\right) = \varrho\left(R - \frac{1}{x}\ln\, \frac{1}{W_F(x)}\right)^{-(\varrho+1)} = \left(\frac{\ln\,(W_F(x)e^{Rx})}{x}\right)^{-(\varrho+1)}.$$

Therefore, our Theorem implies the following collorary.

Corollary 2. *Let $0 < R < +\infty$, $0 < \varrho < \infty$ and φ be a characteristic function on probability law F analytic in $\mathbb{D}_R$, such that* (8) *holds. Then in order that*

$$\int\limits_{r_0}^{R} (R-r)^{\varrho-1} \ln M(r,\varphi)dr < +\infty,$$

it is necessary, and in the case when

$$\ln \frac{1}{W_F(x)} = v(x) \in V(R),$$

it is sufficient that

$$\int\limits_{x_0}^{\infty} \left(\frac{\ln (W_F(x)e^{Rx})}{x} \right)^{\varrho+1} dx < +\infty.$$

Now we suppose that $0 < \varrho < \infty$ and

$$\Phi(r) = \frac{1}{(R-r)^2} \exp\left\{ \frac{\varrho}{R-r} \right\}. \tag{31}$$

Then

$$\Phi'(r) = \left(\frac{2}{(R-r)^3} + \frac{\varrho}{(R-r)^4} \right) \exp\left\{ \frac{\varrho}{R-r} \right\} =$$

$$= \frac{(1+o(1))\varrho}{(R-r)^4} \exp\left\{ \frac{\varrho}{R-r} \right\}, \quad r \uparrow R,$$

$$\Phi''(r) = \frac{(1+o(1))\varrho^2}{(R-r)^6} \exp\left\{ \frac{\varrho}{R-r} \right\}, \quad r \uparrow R,$$

and, therefore,

$$\frac{\Phi'(r)}{\Phi(r)} = \frac{2}{R-r} + \frac{\varrho}{(R-r)^2} \uparrow +\infty, \quad \Phi'(r + 1/\Phi'(r)) = (1+o(1))\Phi'(r))$$

and

$$\frac{\Phi''(r)\Phi(r)}{(\Phi'(r))^2} = 1 + o(1),$$

as $r \uparrow R$. Thus, the function (31) satisfies all conditions of the Theorem and we obtain the following

Corollary 3. *Let $0 < R < +\infty$, $0 < \varrho < \infty$ and φ be a characteristic function on probability law F analytic in $\mathbb{D}_R$, such that* (8) *holds. Then in order that*

$$\int\limits_{r_0}^{R} \varrho \exp\left\{ -\frac{\varrho}{R-r} \right\} \ln M(r,\varphi)dr < +\infty,$$

it is necessary, and in the case when

$$\ln \frac{1}{W_F(x)} = v(x) \in V(R),$$

it is sufficient that

$$\int\limits_{x_0}^{\infty} \exp\left\{-\frac{\varrho x}{\ln\left(W_F(x)e^{Rx}\right)}\right\}\left(\frac{\ln\left(W_F(x)e^{Rx}\right)}{x}\right)^4 dx < +\infty.$$

Finally, let

$$R = +\infty, \quad 0 < \varrho < \infty \quad \text{and} \quad \Phi(r) = e^{\varrho r}.$$

Then

$$\Phi'(r) = \varrho e^{\varrho r}, \quad \Phi'(r)/\Phi(r) = 1/\varrho, \quad \Phi(r)\Phi''(r)(\Phi(r))^{-2} = 1$$

and

$$\Phi'(r + 1/\Phi'(r)) = (1 + o(1))\Phi'(r) \quad \text{as} \quad r \to +\infty,$$

that is all conditions of the Theorem hold, and we obtain the following

Corollary 4. *Let $0 < \varrho < \infty$ and φ be an entire characteristic function on probability law F. Then in order that*

$$\int\limits_{0}^{\infty} e^{-\varrho r} \ln M(r, \varphi)dr < +\infty,$$

it is necessary and, in the case when

$$\ln \frac{1}{W_F(x)} = v(x) \in V(+\infty),$$

it is sufficient that

$$\int\limits_{0}^{\infty} (W_F(x))^{\varrho/x} dx < +\infty.$$

References

[1] Ju. V. Linnik and I. V. Ostrovskii, *Decompositon of random variables and vectors*, Moscow: Nauka (1972), 479, in Russian.

[2] A. A. Gol'dberg and I. V. Ostrovskii, *Value distribution of meromorphic functions*, Moscow: Nauka (1970), 592, in Russian.

[3] Ju. M. Gal' and M. N. Sheremeta, *Belonding of analytic functions to a covergence class*, Dopovidi AN URSR, Ser. A **7** (1985), 11–14, in Ukrainian.

[4] G. R. MacLane, *Asymptotic values of holomorphic function*, Rice Univ. Studies **49** (1963), 83.

[5] M. N. Sheremeta, *On belonging of entire entire characteristic functions on probability laws to a convergence class*, Dopovidi AN URSR, Ser. A **8** (1975), 696–699, in Ukrainian.

[6] V. M. Sorokivskii, *On the growth of characteristic functions on probability laws*, Drogobych 1980, 20. Manuscript dep. in VINITI 17.12.80, N 5330-80 Dep., in Russian.

[7] M. N. Sheremeta and S. I. Fedynyak, *On the derivative of Dirichlet series*, Siberian Math. J. **39**, no. 1 (1998), 206–223.

[8] O. M. Mulyava and M. M. Sheremeta, *On a convergence class for Dirichlet series*, Bull. Soc. Lettres Łódź **50** Ser. Rech. Deform. **30** (2000), 23-30.

[9] P. V. Filevych and M. M. Sheremeta, *On a convergence class for entire functions*, Bull. Soc. Lettres Łódź **53** Ser. Rech. Deform. **40** (2003), 5–16.

[10] O. M. Mulyava, M. M. Sheremeta, and O. M. Sumyk, *Relation between the maximum modulus and the maximal term of Dirichlet series in terms of a convergence class*, Bull. Soc. Lettres Łódź, Ser. Rech. Deform. **62**, no. 2 (2012), 93–105.

Chair of Function Theory and Probability
Lviv National University
Universytetska 1
UA-79000 Lviv
Ukraine
e-mail: m_m_sheremeta@list.ru

Presented by Adam Paszkiewicz at the Session of the Mathematical-Physical Commission of the Łódź Society of Sciences and Arts on December 2, 2013

O PRZNALEŻNOŚCI FUNKCJI CHARAKTERYSTYCZNYCH PRAW PRAWDOPODOBIEŃSTWA DO KLASY ZBIEŻNOŚCI

S t r e s z c z e n i e

Badany jest warunek na prawo prawdopodobieństwa, przy którym jego funkcja charakterystyczna należy do pewnej klasy zbieżności.

PL ISSN 0459-6854

BULLETIN

DE LA SOCIÉTÉ DES SCIENCES ET DES LETTRES DE ŁÓDŹ

2013 Vol. LXIII

Recherches sur les déformations no. 2

pp. 23–34

Bogumiła Kowalczyk and Adam Lecko

RADIUS PROBLEM IN CLASSES OF POLYNOMIAL CLOSE-TO-CONVEX FUNCTIONS

II. PARTIAL SOLUTIONS

Summary

We continue the research of [4] by calculating some radii of reciprocal dependence of selected classes of polynomial close-to-convex functions.

Keywords and phrases: polynomial close-to-convex functions, radius problem

1. Partial solutions

In this section we calculate some radii $R(\Lambda_1, \Lambda_2)$ defined in [4].

For $n \in \mathbb{N}$ and $j = 0, 1, \ldots, n-1$, let

$$\varepsilon_j^n := e^{2j\pi/n}, \quad \epsilon_j^n := e^{(2j+1)\pi/n}.$$

Clearly, when $n \geq 2$, ε_j^n and ϵ_j^n for $j = 0, 1, \ldots, n-1$, are roots of a degree n of 1 and -1, respectively.

Theorem 1.1. *Fix $n \in \mathbb{N}$ and $\xi \in \overline{\mathbb{D}}^0$. Let $\alpha := |\xi|$.*

1. *If $\Lambda_1 = \{(0,0)\}$ and $\Lambda_2 = \left\{(1, \varepsilon_j^n \xi) : j = 0, 1, \ldots, n-1\right\}$, then $R(\Lambda_1, \Lambda_2)$ is the unique root in $(0,1)$ of the equation*

$$\alpha^n r^{n+2} + \alpha^n r^n + r^2 - 1 = 0, \tag{1}$$

i.e., if $f \in \mathcal{P}'$, then

$$\operatorname{Re}\{(1 - \xi^n z^n) f'(z)\} > 0, \quad z \in \mathbb{D}_{R(\Lambda_1, \Lambda_2)}.$$

Equivalently, if $p \in \mathcal{P}$, then

$$\operatorname{Re}\{(1 - \xi^n z^n) p(z)\} > 0, \quad z \in \mathbb{D}_{R(\Lambda_1, \Lambda_2)}.$$

2. *If*

$$\Lambda_1 = \left\{(1, \varepsilon_j^n \xi) : j = 0, 1, \ldots, n-1\right\}$$

and

$$\Lambda_2 = \left\{(1, \epsilon_j^n \xi) : j = 0, 1, \ldots, n-1\right\},$$

then $R(\Lambda_1, \Lambda_2)$ *is the unique root in* $(0,1)$ *of the equation*

$$\alpha^n r^{n+1} + \alpha^n r^n + r - 1 = 0. \tag{2}$$

Thus if $f \in \mathcal{C}(\Lambda_1)$, *i.e., if* $f \in \mathcal{A}$ *and*

$$\operatorname{Re}\left\{(1 - \xi^n z^n) f'(z)\right\} > 0, \quad z \in \mathbb{D},$$

then

$$\operatorname{Re}\left\{(1 + \xi^n z^n) f'(z)\right\} > 0, \quad z \in \mathbb{D}_{R(\Lambda_1, \Lambda_2)}.$$

Equivalently, if $p \in \mathcal{P}$, *then*

$$\operatorname{Re}\left\{\frac{1 + \xi^n z^n}{1 - \xi^n z^n} p(z)\right\} > 0, \quad z \in \mathbb{D}_{R(\Lambda_1, \Lambda_2)}.$$

3. *If* $\Lambda_1 = \{(0,0)\}$ *and* $\Lambda_2 = \{(n, \xi)\}$, *then* $R(\Lambda_1, \Lambda_2)$ *is the unique root in* $(0, r^+(n,\alpha))$ *of the equation*

$$(1 + r^2) A(r; n, \alpha) + r^2 - 1 = 0, \tag{3}$$

where

$$r^+(n,\alpha) := \min\left\{\frac{1}{\alpha} \sin\left(\frac{\pi}{2n}\right), 1\right\} \tag{4}$$

and

$$A(r; n, \alpha) := \sum_{k=1}^{N} (-1)^{k+1} \binom{n}{2k-1} (\alpha r)^{2k-1} \left(\sqrt{1 - \alpha^2 r^2}\right)^{n-2k+1}, \tag{5}$$

with

$$N = \begin{cases} (n+1)/2, & n = 2m-1,\ m \in \mathbb{N}, \\ n/2, & n = 2m,\ m \in \mathbb{N}, \end{cases} \tag{6}$$

i.e., if $f \in \mathcal{P}'$, *then*

$$\operatorname{Re}\left\{(1 - \xi z)^n f'(z)\right\} > 0, \quad z \in \mathbb{D}_{R(\Lambda_1, \Lambda_2)}.$$

Equivalently, if $p \in \mathcal{P}$, *then*

$$\operatorname{Re}\left\{(1 - \xi z)^n p(z)\right\} > 0, \quad z \in \mathbb{D}_{R(\Lambda_1, \Lambda_2)}.$$

4. *If* $\Lambda_1 = \{(n, \xi)\}$ *and* $\Lambda_2 = \{(n, -\xi)\}$, *then* $R(\Lambda_1, \Lambda_2)$ *is the unique root in* $(0, r^+(n,\alpha))$ *of the equation*

$$(1 + r^2) B(r; n, \alpha) + r^2 - 1 = 0, \tag{7}$$

where

$$r^+(n,\alpha) := \min\left\{\frac{1-\cos\left(\frac{\pi}{2n}\right)}{\alpha\sin\left(\frac{\pi}{2n}\right)}, 1\right\} \tag{8}$$

and

$$B(r;n,\alpha) := \sum_{k=1}^{N}(-1)^{k+1}\binom{n}{2k-1}\left(\frac{2\alpha r}{1-\alpha^2r^2}\right)^{2k-1}\left(\frac{1-\alpha^2r^2}{1+\alpha^2r^2}\right)^n, \tag{9}$$

with N given by (6). *Thus if $f \in \mathcal{C}(\Lambda_1)$, i.e. if $f \in \mathcal{A}$ and*

$$\operatorname{Re}\{(1-\xi z)^n f'(z)\} > 0, \quad z \in \mathbb{D},$$

then

$$\operatorname{Re}\{(1+\xi z)^n f'(z)\} > 0, \quad z \in \mathbb{D}_{R(\Lambda_1,\Lambda_2)}.$$

Equivalently, if $p \in \mathcal{P}$, then

$$\operatorname{Re}\left\{\left(\frac{1+\xi z}{1-\xi z}\right)^n p(z)\right\} > 0, \quad z \in \mathbb{D}_{R(\Lambda_1,\Lambda_2)}.$$

5. *For each $n \in \mathbb{N}$ the function*

$$(0,1] \ni \alpha \mapsto R_n(\alpha) := R(\Lambda_1,\Lambda_2) \tag{10}$$

is strictly decreasing in all four cases 1–4.

Proof. Fix $n \in \mathbb{N}$ and $\xi \in \overline{\mathbb{D}}^0$. Let $\alpha := |\xi|$. Then $\alpha \in (0,1]$.

1. Let $\Lambda_1 := \{(0,0)\}$ and $\Lambda_2 := \left\{(1,\varepsilon_j^n\xi) : j = 0,1,\ldots,n-1\right\}$. Then

$$P_{\Lambda_1} \equiv 1, \quad P_{\Lambda_2}(z) = 1-\xi^n z^n, \quad z \in \mathbb{D},$$

and

$$Q_{\Lambda_1,\Lambda_2}(z) = 1-\xi^n z^n, \quad z \in \mathbb{D}.$$

Hence we see that

$$r^+(\Lambda_1,\Lambda_2) = r^-(\Lambda_1,\Lambda_2) = 1$$

and further computations show that

$$\begin{aligned}\varphi(r;\Lambda_1,\Lambda_2) &= \max_{z\in\mathbb{T}_r}\operatorname{Arg} Q_{\Lambda_1,\Lambda_2}(z)\\ &= \max_{z\in\mathbb{T}_r}\operatorname{Arg}(1-\xi^n z^n) = \arcsin(\alpha^n r^n)\\ &= -\psi(r;\Lambda_1,\Lambda_2).\end{aligned}$$

From Theorem 3.4 of [4] it follows that $R_n(\alpha) := R(\Lambda_1,\Lambda_2)$ is the smallest root in $(0,1)$ of the equation (3.26) from [4], i.e., of the equation

$$\alpha^n r^n = \frac{1-r^2}{1+r^2}, \quad r \in (0,1), \tag{11}$$

and consequently of the equation (1). Since the function

$$[0,1] \ni r \mapsto \alpha^n r^n$$

is strictly increasing and the function

$$[0,1] \ni r \mapsto \frac{1-r^2}{1+r^2} \tag{12}$$

is strictly decreasing, we state from (11) that $R_n(\alpha)$ is the unique solution in $(0,1)$ of the equation (1).

Finally we show that the function (10) is strictly decreasing. To see this, write the equation (11) as

$$\alpha^n = g_n(r) := \frac{1-r^2}{r^n(1+r^2)}, \quad r \in (0,1).$$

Since the function g_n is strictly decreasing and

$$\alpha^n = g_n\left(R_n(\alpha)\right), \quad \alpha \in (0,1],$$

we conclude that

$$R_n(\alpha) = g_n^{-1}\left(\alpha^n\right), \quad \alpha \in (0,1].$$

As g_n^{-1} is strictly decreasing, so is the function (10).

2. Let

$$\Lambda_1 := \left\{(1, \varepsilon_j^n \xi) : j = 0, 1, \ldots, n-1\right\}$$

and

$$\Lambda_2 := \left\{(1, \epsilon_j^n \xi) : j = 0, 1, \ldots, n-1\right\}.$$

Then

$$P_{\Lambda_1}(z) = 1 - \xi^n z^n, \quad P_{\Lambda_2}(z) = 1 + \xi^n z^n, \quad z \in \mathbb{D},$$

and

$$Q_{\Lambda_1,\Lambda_2}(z) = \frac{1+\xi^n z^n}{1-\xi^n z^n}, \quad z \in \mathbb{D}.$$

Hence we see that

$$r^+(\Lambda_1, \Lambda_2) = r^-(\Lambda_1, \Lambda_2) = 1$$

and further computations show that

$$\begin{aligned}\varphi(r; \Lambda_1, \Lambda_2) &= \max_{z \in \mathbb{T}_r} \operatorname{Arg} Q_{\Lambda_1,\Lambda_2}(z) \\ &= \max_{z \in \mathbb{T}_r} \operatorname{Arg} \frac{1+\xi^n z^n}{1-\xi^n z^n} = \arcsin \frac{2\alpha^n r^n}{1+\alpha^{2n} r^{2n}} \\ &= -\psi\left(r; \Lambda_1, \Lambda_2\right).\end{aligned}$$

From Theorem 3.4 of [4] it follows that $R_n(\alpha) := R\left(\Lambda_1, \Lambda_2\right)$ is the smallest root in $(0,1)$ of the equation (3.26) from [4], i.e., of the equation

$$\frac{2\alpha^n r^n}{1+\alpha^{2n} r^{2n}} = \frac{1-r^2}{1+r^2}, \quad r \in (0,1). \tag{13}$$

Equivalently,

$$2\alpha^n r^n(1+r^2) - \left(1+\alpha^{2n}r^{2n}\right)(1-r^2) = 0,$$

i.e.,

$$r^2\left(1+\alpha^n r^n\right)^2 - \left(1-\alpha^n r^n\right)^2 = 0.$$

Hence

$$\left(\alpha^n r^{n+1} + \alpha^n r^n + r - 1\right)\left(\alpha^n r^{n+1} - \alpha^n r^n + r + 1\right) = 0,$$

i.e.,

$$\alpha^n r^{n+1} + \alpha^n r^n + r - 1 = 0 \tag{14}$$

or

$$\alpha^n r^{n+1} - \alpha^n r^n + r + 1 = 0.$$

The second equation is of the form

$$\alpha^n r^n = \frac{1+r}{1-r}$$

and since $(1+r)/(1-r) \geq 1$ for $r \in (0,1)$ it has no roots in $(0,1)$. Thus $R_n(\alpha)$ is the smallest root of the equation (14), i.e., of the equation (2). Equivalently, $R_n(\alpha)$ is the smallest root of the equation

$$\alpha^n r^n = \frac{1-r}{1+r}, \quad r \in (0,1). \tag{15}$$

Since the function

$$[0,1] \ni r \mapsto \alpha^n r^n$$

is strictly increasing and the function

$$[0,1] \ni r \mapsto \frac{1-r}{1+r} \tag{16}$$

is strictly decreasing, we state from (15) that $R_n(\alpha)$ is the unique solution in $(0,1)$ of the equation (2).

Writing (15) as

$$\alpha^n = g_n(r) := \frac{1-r}{r^n(1+r)}, \quad r \in (0,1),$$

and arguing as in Part 1 we conclude that the function (10) is strictly decreasing.

3. Let $\Lambda_1 := \{(0,0)\}$ and $\Lambda_2 := \{(n,\xi)\}$. Then

$$P_{\Lambda_1} \equiv 1, \quad P_{\Lambda_2}(z) = (1-\xi z)^n, \quad z \in \mathbb{D},$$

and

$$Q_{\Lambda_1,\Lambda_2}(z) = (1-\xi z)^n, \quad z \in \mathbb{D}.$$

An easy computation shows that

$$\max_{z\in\mathbb{T}_r} \operatorname{Arg}(1-\xi z) = \arcsin(\alpha r).$$

Hence we see that $r^+(n,\alpha) := r^+(\Lambda_1,\Lambda_2)$ is the solution in $(0,1)$ of the equation

$$n\arcsin(\alpha r) = \frac{\pi}{2},$$

i.e.,

$$r^+(n,\alpha)=\frac{1}{\alpha}\sin\left(\frac{\pi}{2n}\right)$$

if such the solution exists or let $r^+(n,\alpha):=1$ otherwise. Thus $r^+(n,\alpha)$ is given by (4). Clearly,

$$r^-(\Lambda_1,\Lambda_2)=r^+(n,\alpha).$$

Thus for $r\in(0,r^+(n,\alpha))$ we have

$$\begin{aligned}\varphi(r;\Lambda_1,\Lambda_2)&=\max_{z\in\mathbb{T}_r}\operatorname{Arg}Q_{\Lambda_1,\Lambda_2}(z)\\&=\max_{z\in\mathbb{T}_r}\operatorname{Arg}\{(1-\xi z)^n\}=n\arcsin(\alpha r)\\&=-\psi(r;\Lambda_1,\Lambda_2).\end{aligned}$$

Using the formula

$$\sin(nx)=\sum_{k=1}^{N}(-1)^{k+1}\binom{n}{2k-1}\cos^{n-2k+1}x\sin^{2k-1}x, \tag{17}$$

with $x=\arcsin(\alpha r)$, where N is given by (6), we see that

$$\varphi(r;\Lambda_1,\Lambda_2)=n\arcsin(\alpha r)=\arcsin A(r;n,\alpha), \tag{18}$$

where $A(r;n,\alpha)$ is given by (5). From Theorem 3.4 of [4] it follows that $R_n(\alpha):=R(\Lambda_1,\Lambda_2)$ is the smallest root in $(0,r^+(n,\alpha))$ of the equation (3.26), i.e., in view of (18), of the equation

$$A(r;n,\alpha)=\sin\varphi(r;\Lambda_1,\Lambda_2)=\frac{1-r^2}{1+r^2}. \tag{19}$$

This proves (3). Since the function

$$(0,r^+(n,\alpha))\ni r\mapsto A(r;n,\alpha)=\sin(n\arcsin(\alpha r))$$

is strictly increasing and the function (12) is strictly decreasing, we state that $R_n(\alpha)$ is the unique solution in $(0,r^+(n,\alpha))$ of the equation (3).

Moreover, by the fact that for each $r\in(0,r^+(n,\alpha))$ the function

$$[0,1]\ni\alpha\mapsto A(r;n,\alpha)=\sin(n\arcsin(\alpha r))$$

is strictly increasing and the function (12) is strictly decreasing, we deduce from (19) that the function (10) is strictly decreasing.

4. Let If $\Lambda_1:=\{(n,\xi)\}$ and $\Lambda_2:=\{(n,-\xi)\}$. Then

$$P_{\Lambda_1}(z)=(1+\xi z)^n,\quad P_{\Lambda_2}(z)=(1-\xi z)^n,\quad z\in\mathbb{D},$$

and

$$Q_{\Lambda_1,\Lambda_2}(z)=\left(\frac{1+\xi z}{1-\xi z}\right)^n,\quad z\in\mathbb{D}.$$

An easy computation shows that

$$\max_{z\in\mathbb{T}_r}\operatorname{Arg}\frac{1+\xi z}{1-\xi z}=\arcsin\frac{2\alpha r}{1+\alpha^2r^2}.$$

Hence we see that $r^+(n,\alpha) := r^+(\Lambda_1, \Lambda_2)$ is the solution in $(0,1)$ of the equation

$$n \arcsin \frac{2\alpha r}{1+\alpha^2 r^2} = \frac{\pi}{2},$$

i.e.

$$r^+(n,\alpha) = \frac{1-\cos\left(\frac{\pi}{2n}\right)}{\alpha \sin\left(\frac{\pi}{2n}\right)}$$

if such solution exists or let $r^+(n,\alpha) := 1$ otherwise. Thus $r^+(n,\alpha)$ is given by (8). Clearly,

$$r^-(\Lambda_1, \Lambda_2) = r^+(n,\alpha).$$

Thus for $r \in (0, r^+(n,\alpha))$ we have

$$\varphi(r; \Lambda_1, \Lambda_2) = \max_{z\in\mathbb{T}_r} \operatorname{Arg} Q_{\Lambda_1,\Lambda_2}(z)$$

$$= \max_{z\in\mathbb{T}_r} \operatorname{Arg} \left(\frac{1+\xi z}{1-\xi z}\right)^n = n \arcsin \frac{2\alpha r}{1+\alpha^2 r^2}$$

$$= -\psi(r; \Lambda_1, \Lambda_2).$$

Using the formula (17) with $x = \arcsin \frac{2\alpha r}{1+\alpha^2 r^2}$ we see that

$$\varphi(r; \Lambda_1, \Lambda_2) = n \arcsin \frac{2\alpha r}{1+\alpha^2 r^2} = \arcsin B(r; n, \alpha), \tag{20}$$

where $B(r;n,\alpha)$ is given by (9). From Theorem 3.4 of [4] it follows that $R_n(\alpha) := R(\Lambda_1, \Lambda_2)$ is the smallest root in $(0, r^+(n,\alpha))$ of the equation (3.26), i.e., in view of (20) of the equation

$$B(r;n,\alpha) = \sin \varphi(r; \Lambda_1, \Lambda_2) = \frac{1-r^2}{1+r^2}. \tag{21}$$

This proves (7). Since the function

$$(0, r^+(n,\alpha)) \ni r \mapsto B(r;n,\alpha) = \sin\left(n \arcsin \frac{2\alpha r}{1+\alpha^2 r^2}\right)$$

is strictly increasing and the function (12) is strictly decreasing, we state that $R_n(\alpha)$ is the unique solution in $(0, r^+(n,\alpha))$ of the equation (7).

Moreover, by the fact that for each $r \in (0, r^+(n,\alpha))$ the function

$$(0,1] \ni \alpha \mapsto B(r;n,\alpha) = \sin\left(n \arcsin \frac{2\alpha r}{1+\alpha^2 r^2}\right)$$

is strictly increasing and the function (12) is strictly decreasing, we deduce from (21) the function (10) is strictly decreasing.

□

2. Special cases

The last theorem yields a sequence of corollaries. The two ones below were proved in [6]. By using the method of proof different than the one used here, Parts 1-2 and 5 of the corollary below were shown in [5]. In cited papers the classes $\mathcal{C}(\Lambda)$ related to square trinomials P_Λ were considered.

Corollary 2.1. *Fix $\xi \in \overline{\mathbb{D}}^0$. Let $\alpha := |\xi|$.*

1. *If $\Lambda_1 = \{(0,0)\}$ and $\Lambda_2 = \{(1,\xi)\}$, then $R(\Lambda_1, \Lambda_2)$ is the unique root in $(0,1)$ of the equation*

$$\alpha r^3 + r^2 + \alpha r - 1 = 0,$$

i.e., if $f \in \mathcal{P}'$, then

$$\operatorname{Re}\{(1-\xi z)f'(z)\} > 0, \quad z \in \mathbb{D}_{R(\Lambda_1,\Lambda_2)}.$$

Equivalently, if $p \in \mathcal{P}$, then

$$\operatorname{Re}\{(1-\xi z)p(z)\} > 0, \quad z \in \mathbb{D}_{R(\Lambda_1,\Lambda_2)}.$$

2. *If $\Lambda_1 = \{(0,0)\}$ and $\Lambda_2 = \{(1,\xi),(1,-\xi)\}$, then*

$$R(\Lambda_1, \Lambda_2) = \sqrt{\frac{2}{1+\alpha^2+\sqrt{1+6\alpha^2+\alpha^4}}},$$

i.e., if $f \in \mathcal{P}'$, then

$$\operatorname{Re}\left\{(1-\xi^2 z^2)f'(z)\right\} > 0, \quad z \in \mathbb{D}_{R(\Lambda_1,\Lambda_2)}.$$

Equivalently, if $p \in \mathcal{P}$, then

$$\operatorname{Re}\left\{(1-\xi^2 z^2)p(z)\right\} > 0, \quad z \in \mathbb{D}_{R(\Lambda_1,\Lambda_2)}.$$

3. *If $\Lambda_1 = \{(1,\xi)\}$ and $\Lambda_2 = \{(1,-\xi)\}$, then*

$$R(\Lambda_1, \Lambda_1) = \frac{2}{1+\alpha+\sqrt{1+6\alpha+\alpha^2}}.$$

Thus if $f \in \mathcal{C}(\Lambda_1)$, i.e., if $f \in \mathcal{A}$ and

$$\operatorname{Re}\{(1-\xi z)f'(z)\} > 0, \quad z \in \mathbb{D},$$

then

$$\operatorname{Re}\{(1+\xi z)f'(z)\} > 0, \quad z \in \mathbb{D}_{R(\Lambda_1,\Lambda_2)}.$$

Equivalently, if $p \in \mathcal{P}$, then

$$\operatorname{Re}\left\{\frac{1+\xi z}{1-\xi z}p(z)\right\} > 0, \quad z \in \mathbb{D}_{R(\Lambda_1,\Lambda_2)}.$$

4. *If $\Lambda_1 = \{(1,\xi),(1,-\xi)\}$ and $\Lambda_2 = \{(1,i\xi),(1,-i\xi)\}$, then $R(\Lambda_1,\Lambda_2)$ is the unique root in $(0,1)$ of the equation*

$$\alpha^2 r^3 + \alpha^2 r^2 + r - 1 = 0.$$

Thus if $f \in \mathcal{C}(\Lambda_1)$, i.e., if $f \in \mathcal{A}$ and

$$\operatorname{Re}\left\{(1-\xi^2 z^2) f'(z)\right\} > 0, \quad z \in \mathbb{D},$$

then

$$\operatorname{Re}\left\{(1+\xi^2 z^2) f'(z)\right\} > 0, \quad z \in \mathbb{D}_{R(\Lambda_1,\Lambda_2)}.$$

Equivalently, if $p \in \mathcal{P}$, then

$$\operatorname{Re}\left\{\frac{1+\xi^2 z^2}{1-\xi^2 z^2} p(z)\right\} > 0, \quad z \in \mathbb{D}_{R(\delta;\Lambda_1,\Lambda_2)}.$$

5. *If $\Lambda_1 = \{(0,0)\}$ and $\Lambda_2 = \{(2,\xi)\}$, then $R(\Lambda_1,\Lambda_2)$ is the unique root in $(0, r^+(2,\alpha))$ of the equation*

$$2\alpha^2 r^4 + \left(2\alpha^2 - 1\right) r^2 + 2r - 1 = 0, \tag{22}$$

where

$$r^+(2,\alpha) = \min\left\{\frac{1}{\sqrt{2}\alpha}, 1\right\},$$

i.e. if $f \in \mathcal{P}'$, then

$$\operatorname{Re}\left\{f'(z)\right\} > 0, \quad z \in \mathbb{D},$$

then

$$\operatorname{Re}\left\{(1-\xi z)^2 f'(z)\right\} > 0, \quad z \in \mathbb{D}_{R(\Lambda_1,\Lambda_2)}.$$

Equivalently, if $p \in \mathcal{P}$, then

$$\operatorname{Re}\left\{(1-\xi z)^2 p(z)\right\} > 0, \quad z \in \mathbb{D}_{R(\Lambda_1,\Lambda_2)}.$$

6. *If $\Lambda_1 = \{(2,\xi)\}$ and $\Lambda_2 = \{(2,-\xi)\}$, then $R(\Lambda_1,\Lambda_2)$ is the unique root in $(0, r^+(2,\alpha))$ of the equation*

$$\alpha^4 r^6 - 4\alpha^3 r^5 + \alpha^2(2-\alpha^2) r^4 + 4\alpha(1-\alpha^2) r^3 + (1-2\alpha^2) r^2 + 4\alpha r - 1 = 0, \tag{23}$$

where

$$r^+(2,\alpha) = \min\left\{(\sqrt{2}-1)/\alpha, 1\right\}.$$

Thus if $f \in \mathcal{C}(\Lambda_1)$, i.e., if $f \in \mathcal{A}$ and

$$\operatorname{Re}\left\{(1-\xi z)^2 f'(z)\right\} > 0, \quad z \in \mathbb{D},$$

then

$$\operatorname{Re}\left\{(1+\xi z)^2 f'(z)\right\} > 0, \quad z \in \mathbb{D}_{R(\Lambda_1,\Lambda_2)}.$$

Equivalently, if $p \in \mathcal{P}$, then

$$\operatorname{Re}\left\{\left(\frac{1+\xi z}{1-\xi z}\right)^2 p(z)\right\} > 0, \quad z \in \mathbb{D}_{R(\Lambda_1,\Lambda_2)}.$$

Proof. Parts 1–4 follow directly from Parts 1–2 of Theorem 2.1.

We prove now Part 5. Let $\Lambda_1 := \{(0,0)\}$ and $\Lambda_2 := \{(2,\xi)\}$. Note first that by (4) we have

$$r^+(2,\alpha) = \min\left\{\frac{1}{\sqrt{2}\alpha}, 1\right\}.$$

Since in view of (5),

$$A(r;2,\alpha) = 2\alpha r\sqrt{1-\alpha^2 r^2},$$

we see by (3) that $R(\Lambda_1,\Lambda_2)$ is the unique root of the equation

$$2(1+r^2)\alpha r\sqrt{1-\alpha^2 r^2} + r^2 - 1 = 0 \tag{24}$$

lying in $(0, r^+(2,\alpha))$. From (24) we have

$$4\alpha^2 r^2 - 4\alpha^4 r^4 = \frac{(1-r^2)^2}{(1+r^2)^2}.$$

Equivalently,

$$(1-2\alpha^2 r^2)^2 = \frac{4r^2}{(1+r^2)^2}.$$

Since $r \in (0, r^+(2,\alpha))$, the above equation yields

$$1 - 2\alpha^2 r^2 = \frac{2r}{1+r^2},$$

i.e., the equation (22).

We prove now Part 6. Let $\Lambda_1 := \{(2,\xi)\}$ and $\Lambda_2 := \{(2,-\xi)\}$. Note first that by (8) we have

$$r^+(2,\alpha) = \min\left\{(\sqrt{2}-1)/\alpha, 1\right\}.$$

Since in view of (9),

$$B(r;2,\alpha) = \frac{4\alpha r(1-\alpha^2 r^2)}{(1+\alpha^2 r^2)^2},$$

we seer by (7) that $R(\Lambda_1,\Lambda_2)$ is the unique root of the equation

$$(1+r^2)\frac{4\alpha r(1-\alpha^2 r^2)}{(1+\alpha^2 r^2)^2} + r^2 - 1 = 0$$

lying in $(0, r^+(2,\alpha))$. Thus

$$(1+r^2)4\alpha r(1-\alpha^2 r^2) = (1-r^2)(1+\alpha^2 r^2)^2$$

which gives (23).

□

When $\xi \in \mathbb{T}$, then $|\alpha| = 1$ and the last corollary yields

Corollary 2.2. 1. *If* $\Lambda_1 = \{(0,0)\}$ *and* $\Lambda_2 = \{(1,1)\}$, *then* $R(\Lambda_1,\Lambda_2)$ *is the unique root in* $(0,1)$ *of the equation*

$$r^3 + r^2 + r - 1 = 0,$$

i.e.,

$$R(\Lambda_1,\Lambda_2)=\sqrt[3]{\frac{\sqrt{33}}{9}+\frac{17}{27}}-\sqrt[3]{\frac{\sqrt{33}}{9}-\frac{17}{27}}-\frac{1}{3}\approx 0.543689. \tag{25}$$

Thus if $f\in\mathcal{P}'$, *then*

$$\operatorname{Re}\{(1-z)f'(z)\}>0,\quad z\in\mathbb{D}_{R(\Lambda_1,\Lambda_2)}.$$

2. *If* $\Lambda_1=\{(0,0)\}$ *and* $\Lambda_2=\{(1,1),(1,-1)\}$, *then*

$$R(\Lambda_1,\Lambda_2)=\sqrt{\sqrt{2}-1}\approx 0.643594,$$

i.e., if $f\in\mathcal{P}'$, *then*

$$\operatorname{Re}\left\{\left(1-z^2\right)f'(z)\right\}>0,\quad z\in\mathbb{D}_{\sqrt{\sqrt{2}-1}}.$$

3. *If* $\Lambda_1=\{(1,1)\}$ *and* $\Lambda_2=\{(1,-1)\}$, *then*

$$R(\Lambda_1,\Lambda_2)=\sqrt{2}-1\approx 0.424213.$$

Thus if $f\in\mathcal{C}(\Lambda_1)$, *i.e., if* $f\in\mathcal{A}$ *and*

$$\operatorname{Re}\{(1-z)f'(z)\}>0,\quad z\in\mathbb{D},$$

then

$$\operatorname{Re}\{(1+z)f'(z)\}>0,\quad z\in\mathbb{D}_{\sqrt{2}-1}.$$

4. *If* $\Lambda_1=\{(1,1),(1,-1)\}$ *and* $\Lambda_2=\{(1,i),(1,-i)\}$, *then* $R(\Lambda_1,\Lambda_2)$ *is the unique root in* $(0,1)$ *of the equation*

$$r^3+r^2+r-1=0,$$

i.e., $R(\Lambda_1,\Lambda_2)$ *is given by* (25). *Thus if* $f\in\mathcal{C}(\Lambda_1)$, *i.e., if* $f\in\mathcal{A}$ *and*

$$\operatorname{Re}\left\{(1-z^2)f'(z)\right\}>0,\quad z\in\mathbb{D},$$

then

$$\operatorname{Re}\left\{(1+z^2)f'(z)\right\}>0,\quad z\in\mathbb{D}_{R(\Lambda_1,\Lambda_2)}.$$

5. *If* $\Lambda_1=\{(0,0)\}$ *and* $\Lambda_2=\{(2,1)\}$, *then* $R(\Lambda_1,\Lambda_2)$ *is the unique root in* $\left(0,1/\sqrt{2}\right)$ *of the equation*

$$2r^4+r^2+2r-1=0,$$

i.e., if $f\in\mathcal{P}'$, *then*

$$\operatorname{Re}\left\{(1-z)^2f'(z)\right\}>0,\quad z\in\mathbb{D}_{R(\Lambda_1,\Lambda_2)}.$$

6. *If* $\Lambda_1=\{(2,1)\}$ *and* $\Lambda_2=\{(2,-1)\}$, *then*

$$R(\Lambda_1,\Lambda_2)=2-\sqrt{3}\approx 0,267949.$$

Thus if $f\in\mathcal{C}(\Lambda_1)$, *i.e., if* $f\in\mathcal{A}$ *and*

$$\operatorname{Re}\left\{(1-z)^2f'(z)\right\}>0,\quad z\in\mathbb{D},$$

then

$$\operatorname{Re}\left\{(1+z)^2f'(z)\right\}>0,\quad z\in\mathbb{D}_{2-\sqrt{3}}.$$

References

[1] A. W. Goodman , *Univalent Functions*, Mariner, Tampa, Florida, 1983.

[2] W. Hengartner and G. Schober, *On schlicht mappings to domains convex in one direction*, Comm. Math. Helv. **45** (1970), 303–314.

[3] B. Kowalczyk and A. Lecko, *Polynomial close-to-convexity*, Submited.

[4] B. Kowalczyk and A. Lecko, *Radius problem in classes of polynomial close-to-convex functions, I*, Bull. Soc. Sci. Lettres Łódź, Sér. Rech. Déform. **63**, no. 1 (2013), 65–77.

[5] A. Lecko, *On reciprocal dependence of some classes of regular functions*, Folia Sci. Univ. Tech. Resov., Matematyka **15**, no. 127 (1994), 35–53.

[6] A. Lecko, *On a radius problem in some subclasses of univalent functions, I*, Folia Sci. Univ. Tech. Resov., Matematyka **19**, no, 147 (1996), 35–54.

[7] A. Lecko, *A generalization of analytic condition for convexity in one direction*, Demonstr. Math. **30**, no. 1 (1997), 155–170.

[8] K. Noshiro, *On the theory of schlicht functions*, J. Fac. Sci. Hokkaido Univ. Jap. **2**, (1934–35), 129–155.

[9] M. S. Robertson, *Analytic functions star-like in one direction*, Amer. J. Math. **58**, (1936), 465–472.

[10] W. C. Royster and M. Ziegler, *Univalent functions convex in one direction*, Publ. Math. Debrecen **23**, no. 3–4 (1976), 339–345.

[11] S. E. Warschawski , *On the higher derivatives at the boundary in conformal mapping*, Trans. Amer. Math. Soc. **38**, no. 2 (1935), 310–340.

Department of Applied Mathematics
University of Warmia and Mazury
Słoneczna 54, 10-710 Olsztyn
Poland

Department of Analysis and Differential Equations
University of Warmia and Mazury
Słoneczna 54, PL-10-710 Olsztyn
Poland
e-mail: alecko@matman.uwm.edu.pl

Presented by Zbigniew Jakubowski at the Session of the Mathematical-Physical Commission of the Łódź Society of Sciences and Arts on February 7, 2013

PROBLEM PROMIENI W KLASACH FUNKCJI WIELOMIANOWO PRAWIE WYPUKŁYCH

II. CZĘŚCIOWE ROZWIĄZANIA

S t r e s z c z e n i e

W pracy tej będącej kontynuacją pracy *Radius problem in classes of polynomial close-to-convex functions I* opublikowanej w *Bulletin de la Société des Sciences et des Lettres de Łódź. Série: Recherches sur les Déformations* wyznaczone są promienie wzajemnej zależności wybranych klas funkcji wielomianowo prawie wypukłych.

PL ISSN 0459-6854

B U L L E T I N

DE LA SOCIÉTÉ DES SCIENCES ET DES LETTRES DE ŁÓDŹ

2013 Vol. LXIII

Recherches sur les déformations no. 2

pp. 35–49

Stanisław Bednarek

BUOYANCY BUBBLE FOIL

Summary

The new type of bubble foil filled by gas with density smaller than air density, helium or hydrogen, is described. In result this foil shows a lifting force for proper dimensions of the bubble. The internal structure of foil having regularly located cubical bubbles is presented and the elementary cell is selected. An analysis of forces applied to this cell is given and the minimal length of bubble for positive value of the lifting force is calculated. These calculations are executed for different thicknesses of foils and different densities of gases. A formula for unitary lifting force is derived and charts of dependences of this force on cube length are driven. Experimental production of such a foil is also described. Migration of helium trough walls of bubbles and decreasing of lifting force are observed in the produced foil. As a conclusion of this observation the using of the metal-coated or graphene-coated foil for buoyancy foil production is proposed. The previous calculation and analysis are then repeated for these proposed foils. Advantages of graphene layer coating are discussed. Results of the executed investigation confirms that production and practical application of the proposed buoyancy foil are possible.

Keywords and phrases: bubble foil, metalized, graphene, lifting force

1. Introduction

The well-known air bubble film, which is commonly called bubble foil, comprises two layers of polyethylene sheeting. One of these layers is flat and the other one has pressed hollows in a shape similar to that of a cylinder, which are allocated regularly on the whole surface and filled with air under the atmospheric pressure. Both layers are welded with each other in the places between the hollows. Because of the fact that the air closed in those hollows is compressible, the air bubble film is able to absorb the impact energy. Thanks to that it is widely used for packing different goods and items, especially those made of fragile materials in order to secure them

against mechanical damage [1]. Bubble foil was invented in 1957 by A. Fielding and M. Chavannes, and it was to serve as a new kind of wallpaper.

The aim of this article is to present results of model research and first experiments with a new type of bubble foil, which consists of gases whose density is smaller than that of air. After fulfilling certain conditions, the average density of this foil is smaller than the density of air. As a result, the foil is able to float in the atmosphere, and that is why it is called a buoyancy foil. Bubble foils can be shaped in an easy way, e.g. through cutting, folding, bending and welding. Thanks to that, a new kind of foil is suitable for aircrafts construction, which would be lighter than air (so called dirigibles) and which would have different shapes. Such aircrafts may have various uses, among others, in transport, commerce, research or security against radiolocation devices. Despite the freedom of giving different shapes to such crafts, they are easy and cheap to build. What is very important, they are highly resistant to being deprived of a lifting force, for example in the case of shooting out or even tearing the sheathing, and therefore they are reliable and safe for use.

2. Structure and production of foil

Buoyancy bubble foil comprise two identical layers of polyethylene foil 1 and 2 of h thickness (Figs. 1, 2). Each layer consists of cuboidal hollows with a square base, placed on the whole surface. Internal length of a base side is a and internal height of the cuboid is $a/2$. These hollows are allocated in a regular manner and the distance between their external walls is b. As a result, the flat surface of the foil, between the hollows, has a shape of grid. Layers of the foil are placed symmetrically towards each other and their hollows are turned towards the internal area. Because of that the hollows create cubical bubbles, with an external line of a. Both layers of the foil are connected with each other on the whole flat surface 3 between the hollows, and each bubble is filled with gas 4 of ρ_2 density, smaller than ρ_1 density of atmospheric air 5, surrounding the foil. Density of polyethylene that creates the foil is ρ_3.

The described buoyancy foil can be produced on an industrial scale with a method similar to a typical method of air bubble film production. The typical method consists in producing firstly a thin foil, by pressing polyethylene through a slot nozzle and blowing with an air stream [2, 3]. The obtained foil is moved above a rolling drum, equipped with small, regularly allocated holes whose diameter is the same as that of the hollows. The hollows are pressed through a stream of hot air. Then, the hollows are covered with flat foil, and both foils are welded on a surface among the hollows, by a hot roll with a profiled surface [4, 5]. The process of welding of the foil takes place in the air under atmospheric pressure, thanks to which air is also closed within the bubbles created after the foil is welded.

In order to obtain the presented buoyancy foil, two identical layers of foil with hollows may be produced using the typical method. Then, those layers should go through a chamber filled with gas whose density is lower than the density of air.

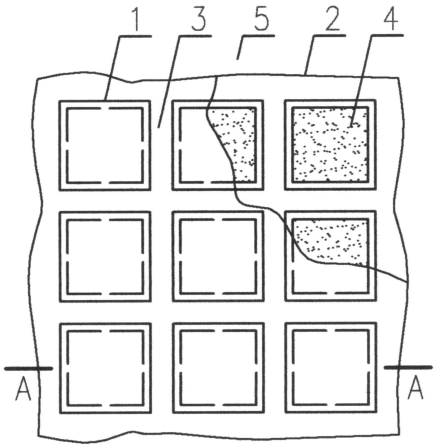

Fig. 1: Structure of the buoyancy bubble foil presented on top view: 1, 2 – layers of foil with concaves – down and upper respectively, 3 – surface of layers connection, 4 – bubble filling gas, 5 – air.

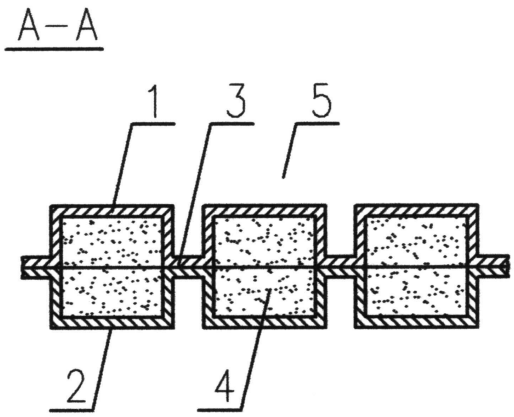

Fig. 2: Structure of the buoyancy bubble foil from Fig. 1 presented on cross-section by A-A plane: description of elements is the same as on Fig. 1.

The layers are put on each other and welded on a surface among the hollows. As a result, gas filling the chamber is closed within the bubbles. At the final stage of production, the foil is pulled out of the chamber and put in the area filled with atmospheric air.

3. Minimal size of a cell

Now we will take a closer look at the forces that influence one cubical bubble along with the fragments of flat surface connecting the bubbles that surround it (Fig. 3). The smallest, repeated fragment of foil will be called *elementary cell*. According to Archimedes' law and principles of statics, this cell, being in the field of gravity of Earth with intensity of $g = 9.81\,\mathrm{m/s^2}$, is influenced by the following forces: air uplift pressure W_p, weight of gas that fills the bubble W_g, and weight of the foil W_f [6]. The resultant of those forces F_N is a lifting force of an elementary cell and is expressed by the following formula:

$$F_N = W_p - W_g - W_f. \tag{1}$$

Taking into account the dimension markings for an elementary cell as it is shown in Fig. 3 and previously given markings for density, volumes of the following elements have been calculated: displaced air, gas comprised within a bubble, and foil creating a bubble. Multiplying these volumes by adequate densities and field of gravitation intensity g, the following formulae for forces W_p, W_g, and W_f have been obtained:

$$W_p = \left[a^3 + 2(a+b)^2 h - 2a^2 h\right] \rho_1 g, \tag{2}$$

$$W_g = (a-2h)^3 \rho_2 g, \tag{3}$$

$$W_f = \left[a^3 - 2(a-2h)^3 h + 2(a+b)^2 h - 2a^2 h\right] \rho_3 g. \tag{4}$$

Having substituted (2)–(4) into (1) a formula for a lifting force of a cell was derived in the following form:

$$\begin{aligned} F_N = \big\{ &\left[a^3 + 2(a+b)^2 h - 2a^2 h\right] \rho_1 - \left[(a-2h)^3 \rho_2\right] \\ &- \left[a^3 - (a-2h)^3 + 2(a+b)^2 h - 2a^2 h\right] \rho_3 \big\}\, g. \end{aligned} \tag{5}$$

Formula (5) presents a function of third degree of external size of a bubble a. An analysis of the variation of this function for values, which are present in reality, of air density and gases with density lower than that of air, and two types of polyethylene (LD – low density polyethylene, HD – high density polyethylene), leads to the conclusion that the function grows fast along with growth of the external size of a bubble a, and it can have either positive or negative values. What is more, the value of this function depends also on a relation between a and other dimensions b, h of a cell. Together with the small values of those relations, considering the relation $\rho_3 >> \rho_2, \rho_1$ (ρ_3 is $920\,\mathrm{kg/m^3}$ for polyethylene LD and $940\,\mathrm{kg/m^3}$ for polyethylene HD, whereas ρ_2, ρ_1 have values of $1\text{–}10^{-1}\,\mathrm{kg/m^3}$), the dominating value is that of foil weight and the lifting force is negative [7, 8]. An increase of the value causes the fact that this force becomes positive, and the foil is able to float in the air independently and to lift items attached to it.

For further deliberations a key meaning is ascribed to calculate minimal value of the size of a bubble a_m, above which a lifting force becomes positive. For this

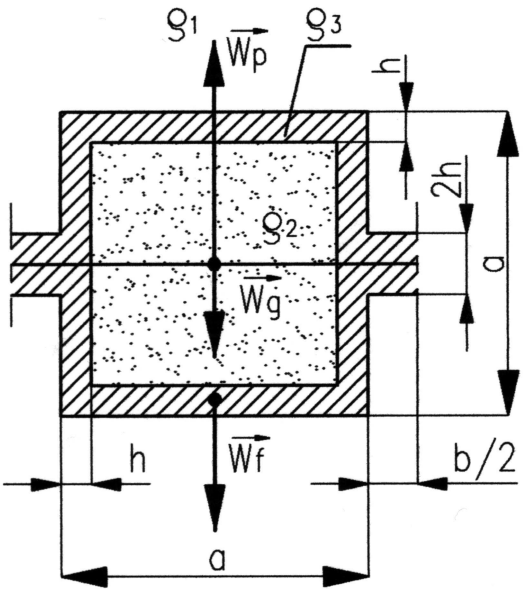

Fig. 3: Forces applied to an elementary cell of the buoyancy bubble foil: W_p – force of air buoyancy, W_g – weight of gas concave filling, W_f – foil weight, ρ_1, ρ_2, ρ_3 – densities of air, filling gas, and foil, respectively.

purpose, a left-hand side of the expression (5) is compared with 0, and a is replaced with a_m which results in:

$$\begin{aligned}(6)\qquad &\left[a_m^3 + 2(a_m^3 + b)^2 h - 2a_m^2 h\right]\rho_1 - \left[(a_m - 2h)^3 \rho_3\right] \\ &- \left[a_m^3 - (a_m - 2h)^3 + 2(a_m + b)^2 h - 2a_m^2 h\right]\rho_3 = 0.\end{aligned}$$

Expression (6) is an equation of the third degree for a_m, consisting of complex coefficients. Arranging coefficients with subsequent powers of the unknown and using the analytical method of Cardano would be labour-consuming, and would lead to highly complicated formulae. That is why, this equation was solved numerically with a method of dividing a range by two, whose ends change a_m [9] – the polynomial of a variable referring to that equation. The calculations are conducted for all gases whose density is lower than that of air, and with chosen thickness of the polyethylene foil within the scope of 0.01–0.1 mm, which was made from polyethylene LD and/or HD. The calculations comprise densities of gases and air that are listed in physical tables [10, 11]. The distance between external walls of the bubbles is assumed to amount at $b = 2$ mm. Results of those calculations are presented in Table 1. Obtained minimal

sizes of the bubbles a_m are comprised within a scope of 5.13 cm to more than 15 m. Obviously, from the practical perspective, sensible are bubbles of sizes not exceeding seven dozens of cm. The easiest way to obtain such sizes is to use hydrogen and helium as gases filling the bubbles. That is why, in further deliberations, only those two gases will be taken into account.

Tab. 1: Minimal size of the bubble a_m for different structures of buoyancy bubble foil.

Gas	Thickness of polyethylene foil h (mm)							
	0.01		0.02		0.05		0.1	
	Kind of polyethylene							
	LD	HD	LD	HD	LD	HD	LD	HD
	Minimal internal size of the bubble a_m (cm)							
Hydrogen (H)	5.12	5.33	10.2	10.4	25.6	26.1	50.7	53.1
Helium (He)	5.45	5.68	10.9	11.3	27.1	28.5	51.2	53.4
Methane (CH_4)	10.46	10.97	20.9	21.9	52.3	54.6	104.9	110.2
Ammonia (NH_4)	11.61	12.11	23.2	24.2	57.9	60.7	116.5	122.3
Neon (Ne)	15.23	16.05	30.8	32.1	77.1	89.3	154.4	161.6
Carbon oxide (CO)	138.3	145.1	278.3	291.5	696.3	807.4	1342.3	1473.1
Nitrogen (N)	145.1	151.3	281.6	299.7	716.6	829.8	1381.6	1513.6

For the purpose of calculations, the assumed density was in the temperature of 20 °C: air $\rho_1 = 1.185\,\mathrm{kg/m^3}$. Other gases: hydrogen $\rho_2 = 0.0823\,\mathrm{kg/m^3}$, helium $\rho_2 = 0.164\,\mathrm{kg/m^3}$, methane $\rho_2 = 0.657\,\mathrm{kg/m^3}$, ammonia $\rho_2 = 0.708\,\mathrm{kg/m^3}$, neon $\rho_2 = 0.824\,\mathrm{kg/m^3}$, carbon oxide $\rho_2 = 1.145\,\mathrm{kg/m^3}$, nitrogen $\rho_2 = 1.146\,\mathrm{kg/m^3}$, and polyethylene: $\rho_3 = 920\,\mathrm{kg/m^3}$ (LD) and $\rho_3 = 940\,\mathrm{kg/m^3}$ (HD). Distance between the internal walls of the neighboring bubbles $b = 2\,\mathrm{mm}$.

Because of a complicated form of equation (6), its analysis is difficult. However, in practice a, b, h dimensions meet the requirements $b << a$, $h << b$, and what is more, it was earlier found out that $\rho_3 >> \rho_2,\ \rho_1$. As a result, several elements in an expansion of the equation (6) comprising squares and cubes h and b can be omitted. It corresponds with omitting tiny volumes of foil in corners and sides of the cell. Moreover, differences of density $\rho_3 - \rho_2$ and $\rho_3 - \rho_1$ have value close to ρ_3. After taking these assumptions, equation (6) takes the form

$$(\rho_1 - \rho_2)a_m^2 + 6a_m h\rho_3 + 4bh\rho_3 \approx 0, \tag{7}$$

i.e. a quadratic equation which is possible to solve using Viéte's formulae. The discriminant of this equation for values $\rho_1, \rho_2, \rho_3, h, b$ present in reality is positive, that is why equation (7) has two real roots. Only one of those roots is positive and has a physical sense. This root is expressed as

$$a_m = \frac{6h\rho_3 + \sqrt{(6h\rho_3)^2 + 16bh\rho_3(\rho_1 - \rho_2)}}{2(\rho_1 - \rho_2} . \tag{8}$$

After expanding the sum that is under the root into the Taylor series and transformation, we can get an approximate formula which allows to estimate the minimal size of a bubble a_m quickly:

$$a_m \approx \frac{6h\rho_3}{\rho_1 - \rho_2} + \frac{4}{3}b. \tag{9}$$

In the latter formula it is easy to notice that a significant influence on lowering the size of a bubble is presented by: using a foil with lower thickness h, made of polyethylene LD (smaller ρ_3 value), filling the bubble with gas of smaller density ρ_2 and narrowing the space b between neighbouring bubbles. An analysis of the results of calculations made according to the precise formula (8) leads to the same conclusions, which are listed in Tab. 1. Undoubtedly, lowering the size of bubbles allows shaping the foil in an easier way, and widens its scope of use.

4. Unitary lifting force

A significant meaning for practical use of buoyancy bubble foil is ascribed to a lifting force that affects the unit of foil volume. The value of this force will be marked by F_1, and in further considerations it will be called *unitary lifting force*. According to Fig. 3, it is possible to place a cuboid with rectangular base into each elementary cell. The side of a base of this cuboid is $a+b$ long, and its height is a. If the layers of foil are placed on each other, the number of cells comprised within unit of volume is determined by the equation $1/[(a+b)^2 a]$. Each cell is influenced by the lifting force that can be expressed by the formula (5). That is why the formula for unitary lifting force reads:

$$F_1 = \frac{\left\{\left[a^3 + 2(a+b)^2 h - 2a^2 h\right]\rho_1 - \left[(a-2h)^3 \rho_3\right]\right\} g}{(a+b)^2 a} - \frac{\left[a^3 - (a-2h)^3 + 2(a+b)^2 h - 2a^2 h\right]\rho_3 g}{(a+b)^2 a}. \tag{10}$$

The value of force F_1 is positive with the values $a > a_m$ calculated for a particular kind of foil, and listed in Tab. 1. Dependence of force F_1 from the size of a bubble a was numerically probed for previously distinguished foils filled with helium or hydrogen, that can be used for practical purposes. For a foil with smaller sizes of bubbles, b – the length between neighbouring walls of the bubbles is 2 mm, and when it comes to bigger bubbles, the length is enhanced to 5 mm; results of these calculations are presented in Fig. 5, 6. Diagrams show an asymptotic growth of F_1 with growth of size of an elementary cell a. The growth stops at the boundary value $(\rho_1 - \rho_2)g$, which is the same as the difference of weights of air and the gasses filling the bubbles. The obtained results are explained by the fact that the value of buoyant force grows along with the third power of the bubble size, which is much faster than the weight of the foil growing along with square of this size. With bubble

sizes much bigger than the minimal, weight of the foil is negligible in comparison with buoyancy force. What is more, value of the unitary lifting force F_1 is lower and grows much slower along with an increase of the thickness of foil. Filling the bubbles with gas of small density (with hydrogen instead of helium) we observe triggers faster growth of F_1 and 10 % increase of its boundary value. Lowering the value of F_1 is insignificant after using polyethylene HD instead of LD. Considering, in equation (10), the relations listed previously: $b << a$, $h << b$ and $\rho_3 >> \rho_2,\ \rho_1$ after transformations, a simplified formula for F_1 is obtained:

$$F_1 \approx \left\{(\rho_1 - \rho_2) - 6\rho_3 \left[1 + \frac{2}{3}\left(\frac{b}{a}\right)\right]\left(\frac{h}{a}\right)\right\} g. \tag{11}$$

The latter formula allows to show easily that F_1 attempts to reach the boundary value $(\rho_1 - \rho_2)g$ when $b, h << a$, and that F_1 grows faster for, and reaches higher values for, with smaller densities ρ_1, ρ_2.

In addition, it has to be mentioned that the cubic bubbles provide the highest value of the unitary lifting force in comparison with bubbles of a different shape. It results from the known geometrical theorems about the closest packing [9]. For example, if the foil comprised the closest packed bubbles with a shape of identical spheres of the same diameter as the length of a side of a cube, a ratio of weight of walls of a spherical bubble to a lifting force would be the same as in the case of a cubic bubble. It is true that for producing such a bubble a smaller amount of foil would be needed, but a spherical bubble would close a smaller volume than a corresponding cube, and the lifting force would also be lower. The ratio of the weight of walls to a lifting force would be lowered by a bigger weight of a fragment of foil in a shape of a polygon with a cut-out circle, joining the bubbles. Moreover, with the closest packing of identical spheres, only 74 % of space is filled. Calculations conducted for that model show that as the result, a unitary lifting force with bubbles in a shape of the closest packed, identical spheres would only be 69 % of the value of that force for cubic cells.

There was an experiment conducted on a small scale, which consisted in creating a cellular buoyancy foil filled with helium. For that purpose, a ready polyethylene LD foil was used, with thickness of 0.02 mm, which is usually used for packages of food. Squares with a side of 15 cm were cut out of this foil and welded on the edges, which created cubical cells, partially opened at one edge. Thermal impulse heat sealing machine FS 300 was used for the purpose of joining the foil. The width of the weld cube, which was turned towards the inside was 2 mm. The obtained cubes were transferred to the upper part of the chamber, where an end of a hose, connected by a reducer with a bottle containing helium, was put through an opened fragment of the edge. Atmospheric air that was initially present in cubes was replaced by helium.

After that, a hose was removed and keeping a cube in the upper part of the chamber, an open fragment of the edge was closed by a welder. In that way, using simple means, cubes filled with helium under atmospheric pressure were obtained. Next, those cubes were joined together by welding the jutting out welds with the

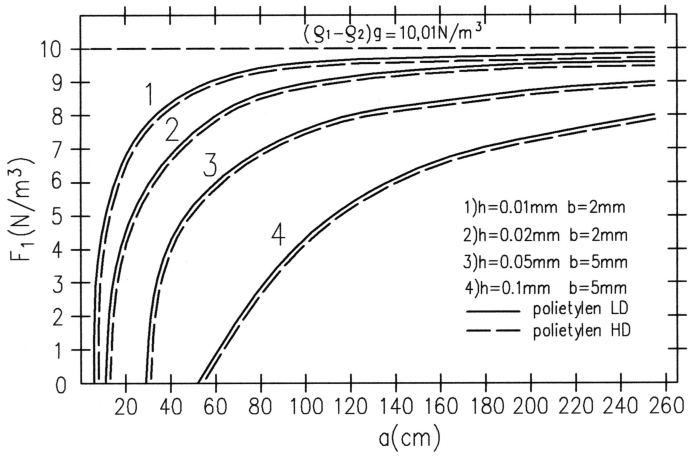

Fig. 4: Dependence of the unitary lifting force F_1 on length of bubble a for buoyancy bubble foil filled by helium.

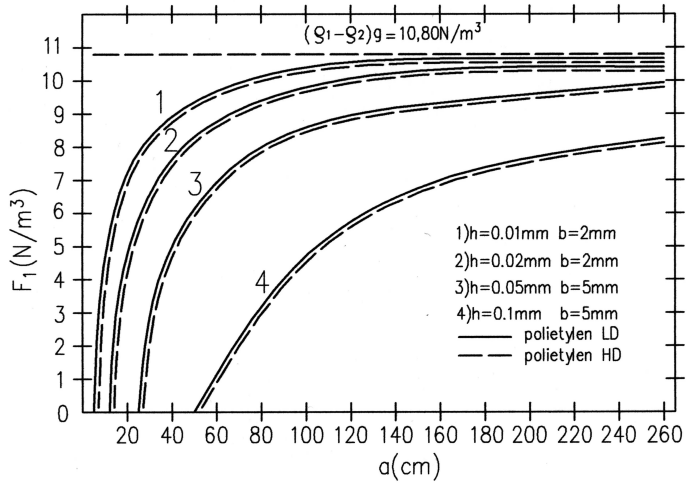

Fig. 5: Dependence of the unitary lifting force F_1 on length of bubble a for buoyancy bubble foil filled by hydrogen.

same welding machine. As a result, mats with thickness of one cube, comprising a hundred, regularly allocated cubes, were obtained.

The produced mats floated in the air, and were able to lift small items. Average lifting force of such a mat, determined experimentally, was $(2.76 \pm 0.08)\,\mathrm{N/m^3}$ and within the margin of error it complies with a theoretical value read from the Fig. 4.

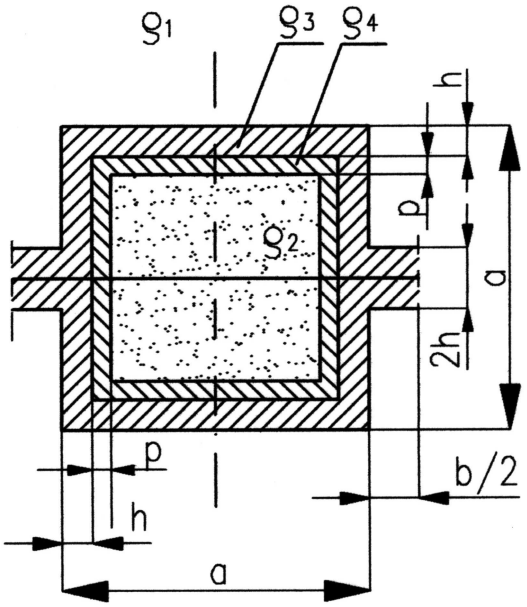

Fig. 6: Elementary cell of metal coated buoyancy bubble foil presented on the cross-section – comp. Figs. 2 and 3: ρ_4 – metal density.

Low durability turned out to be a defect of the produced mat. Volume of the bubbles was becoming smaller with the flow of time, and after 18–23 days, the lifting force did not allow the foil to stay in the air. This effect took place because molecules of helium in move in room temperature at an average square speed of 1300 m/s, and because of that helium is very penetrating [10]. Thin polymer foils, regarding their chain molecular structure, show some permeability for liquids and gases [12]. As a consequence, permeability of helium through the walls of bubbles to air took place. Also some amount of air transmitted to the bubbles. As a final result, the average density of a mix of gases in the bubble increased, and their volume decreased, which according to the formula (5) resulted in disappearance of a lifting force.

5. Metalized foil

It is generally known that thicker foils have lower permeability, but according to previous assumptions, it causes disadvantageous increase of the minimal size of the bubbles. A better way to decrease the permeability is to coat the foils with a thin layer of material with low permeability, e.g. metal. That is why, this part of the article presents the results of calculations for a buoyancy foil produced with the use of metalized foil. An elementary cell of such buoyancy foil is shown in Fig. 6. A way

of conduct described earlier was used for the purpose of these calculations with a difference that in equation (4) weight of the metalized layer was added. Denoting thickness of the layer by p and density of the metal by ρ_4, the weight of a cell is expressed by the following formula:

$$W_f = \left[a^3 - (a-2h)^3 + 2(a+b)^2 h - 2a^2 h\right] \rho_3 g + \left[(a-2h)^3 - (a-2h-2p)^3\right] \rho_4 g. \tag{12}$$

After adding (12) to equations (5), (10) and assuming that the foil metallized with a layer of aluminium with density of $\rho_4 = 2700\,\mathrm{kg/m^3}$ and thickness of $p = 0.005\,\mathrm{mm}$, it is possible to calculate numerically the sizes of bubbles a_m for foils filled with helium and hydrogen, and value of the unitary lifting force F_1. Results of those calculations are presented in Tab. 2. and in Figs. 7, 8. The obtained results show that metallization causes a significant growth of minimal sizes of the bubbles a_m, which is more clearly marked in the case of foil of smaller thickness, and decreasing a unitary lifting force F_1 and its slower pursuit to boundary values.

Tab. 2: Minimal size of the bubble a_m for different structures of buoyancy metal coated bubble foil. Metal layer of aluminium with density of $\rho_4 = 2700\,\mathrm{kg/m^3}$ has thickness of $p = 0.005\,\mathrm{mm}$.

Gas	Thickness of polyethylene foil h (mm)							
	0.01		0.02		0.05		0.1	
	Kind of polyethylene							
	LD	HD	LD	HD	LD	HD	LD	HD
	Minimal internal size of the bubble a_m (cm)							
Hydrogen (H)	12.3	13.5	24.82	25.2	61.3	62.8	122.7	123.1
Helium (He)	13.8	14.4	26.9	65.6	65.6	66.3	132.5	133.6

After using the previously ascertained relations $b << a$, $h << b$, $\rho_3 >> \rho_2, \rho_1$ and taking into account that for a metallized foil there is also $p << a$ and $\rho_4 >> \rho_2, \rho_1$, the following formulae approximated to the minimal size of a bubble a_m and unitary lifting force F_1 are formulated:

$$a_m \approx \frac{6(h\rho_3 + p\rho)}{\rho_1 - \rho_2} + \frac{4}{3}\,\frac{bh\rho_3}{3(h\rho_3 + p\rho_4)}, \tag{13}$$

$$F_1 \approx \left\{(\rho_1 - \rho_2) - 6\rho_3\left[1 + \frac{2}{3}\left(\frac{b}{a}\right)\right]\left(\frac{h}{a}\right) - 6\rho_4\left(\frac{p}{a}\right)\right\} g. \tag{14}$$

The obtained formulae, with lack of metallization ($p = 0$) simplify adequately to formulae (9) and (11), and what is more, it is easy to draw previously discussed regularities out of them, which are noticed in Tab. 2. and in the Figs. 7, 8. This proves the correctness of the derived approximated formulae (13), (14).

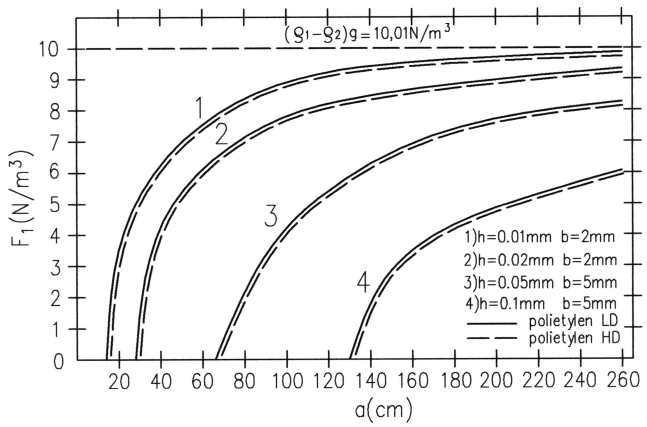

Fig. 7: Dependence of the unitary lifting force F_1 on length of bubble a for buoyancy metal coated bubble foil filled by hydrogen. Parameters of metal layer the same as in Tab. 2 description.

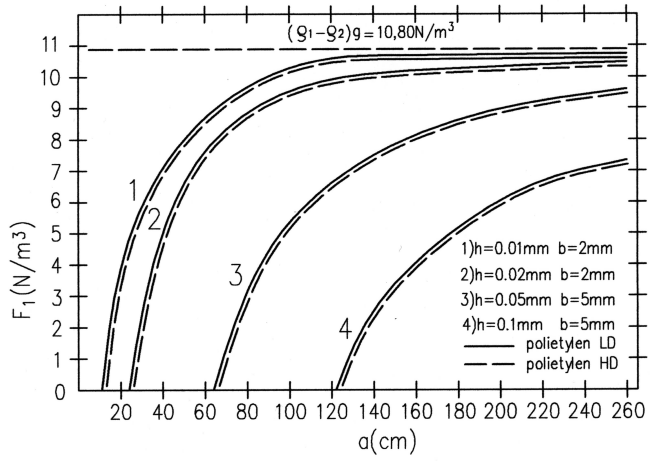

Fig. 8: Dependence of the unitary lifting force F_1 on length of bubble a for buoyancy metal coated bubble foil filled by helium. Parameters of metal layer the same as in Tab. 2 description.

6. Conclusions and perspectives

Calculations conducted for the accepted model of an elementary cell as well as the conducted experiments confirm that there is a real possibility to produce a buoyancy bubble foil from polyethylene filled with hydrogen or helium. In order that the lifting force of such a foil be positive, the edges of the cubical bubbles filled with hydrogen

whose walls are 0.01 mm thick, have to be longer than 5.2 cm. Because of a danger that hydrogen with oxygen may create an explosive mixture, the more advantageous gas is helium, for which the minimal lengths of the bubbles edges have to be higher by several percents. Taking into consideration the easiness of shaping different flying objects constructed from such a foil, bubbles of sizes not exceeding 20–30 cm are useful, whose walls are several hundred parts of mm thick.

While using the buoyancy bubble foil, permeability of gases through the walls made of thin foil takes place, which causes a decrease of the lifting force. Removing this problem by metallizing the foil or increasing its thickness causes a disadvantageous increase of minimal sizes of the bubbles. A promising solution to that problem may be presented by coating the internal surface of the bubbles with graphene. Discovered in 2004, graphene is a monoatomic layer of carbon atoms of hexagonal structure [13]. One of the unique properties of this material is impermeability of even the most volatile gases [14]. Thanks to the monoatomic thickness, surface density of this material is extraordinarily low: $3.5 \cdot 10^{-7}\,\mathrm{kg/m^2}$. An increase of the foil weight as a result of graphene coating is negligibly small and it will not increase the minimal sizes of the bubbles.

Moreover, graphene shows other properties. Its resistance towards tearing is 90 times higher than that of steel, and before it is tore, unit elongation achieves 30 %. Its electric conductivity is 5.9 times higher than the conductivity of copper [15]. An advantage of graphene coating would be a multiple growth of mechanical resistance of the bubbles, even when using very thin polyethylene foils whose thickness do not exceed several hundred parts of mm. Skin effect, known from the static electrodynamics, causes the fact that high electric conductivity of graphene prevents the permeability of micro and radio waves to the objects coated with this material, and it causes reflection of those waves [16]. Thanks to that, the buoyancy bubble foil with graphene coating allows to construct screens floating in the air, which can protect objects against being found by methods of radiolocation, or which can serve as mirrors reflecting electromagnetic radiation.

Right after graphene was discovered, it was very hard and expensive to coat a surface with it. However, currently there are cheaper methods of obtaining graphene panels with side of several dozens of cm, and attaching it to different surfaces [17–19]. This fact explains the probability of production of buoyancy bubble foil on a great scale, according to the analysed concept, which would be internally coated with a graphene layer and which has many different uses.

References

[1] K. S. Marsh and A. L. Brody, *Encyclopedia of Packing Technology*, John Wiley and Sons Inc., New York 1997, pp. 322–327.

[2] F. W. Bilmeyer Jr., *Textbook of Polymer Science*, John Wiley and Sons Inc., New York 1984, pp. 184–189.

[3] J. Sęk, *Plastics and its production methods (Tworzywa sztuczne i metody ich przetwórstwa)*, Publisher Technical University of Lódź, Łódź 2009, pp. 11–12 (in Polish).

[4] D. Żuchowska, *Construction polymers, Production and properties (Polimery konstrukcyjne. Przetwórstwo i właściwości)*, Publisher of Wrocław Technical University, Wrocław 1993, pp. 124–127 (in Polish).

[5] D. H. Morton-Jones, *Polymer Processing*, Chapman and Hall Ltd., London 1978, pp. 326–328.

[6] D. Halliday, R. Resnick, and J. Walker, *Fundamentals of Physics, Part 2*, John Wiley and Sons Inc., New York 2001, p. 71.

[7] *CRC Handbook of Chemistry and Physics*, CRC Press Boka-Roca, London 1995, p. 76.

[8] W. Mizerski, *Chemical Tables (Tablice chemiczne)*, Publisher Adamantan, Warszawa 1997, pp. 290–293 (in Polish).

[9] N. J. Bronsztejn, K. A. Siemiendiajew, G. Musiol, H. Mühling, *Taschnebuch der Mathematik*, Wissenschaftlicher Verlag Harii Deusth GmbH, Frankfurt an Main 2001, p. 171.

[10] W. Mizerski, *Physical-astronomical Tables (Tablice fizyczno-astronomiczne)*, Publisher Adamantan, Warszawa 2002, pp. 58–59 (in Polish).

[11] J. Arthur and L. Mary, *Macmillan's Chemical and Physical Data*, Macmillan's Press, London and Basingstoke 1992, pp. 283–292.

[12] K. H. Lautenschläger, W. Schörter, and A. Wanniuger, *Taschnebuch der Chemie*, Wissenschaftlicher Verlag, Harii Deusth GmbH, Frankfurt an Main 2005, pp. 771–772.

[13] A. K. Geim and K. S. Novoselov, *The rise graphene*, Nature Materials **6**, no. 3 (2007), 183–191.

[14] E. A. Kim and A. H. Castro-Neto, *Graphene; the soft and hard face of a material*, Europhysics News **40**, no. 2 (2009), 18–19.

[15] A. K. Geim, K. S. Novoselov, S. V. Morozov, D. Jiang, Y. Zhang, S. V. Dubons, I. V. Grigorieva, and A. A. Firsov, *Elecric field effect in atomically thin carbon*, Science **306** (2004), 5696–5661.

[16] D. J. Griffits, *Introduction to Electrodynamics*, Prentice-Hall Inc., New Jersey 1999, pp. 431–432.

[17] S. Ashley, *Smart production of grapheme (Urabianie grafenu)*, Scientific American (Świat Nauki) **4** (2010), 18–19 (in Polish).

[18] S. Park, D. A. Dikin, S. B. T. Nguyen, and R. S. Ruof, *Graphene oxides sheets chemically cross-linked by polyallyamine*, Journal of Chemical Physics **113**, no. 36 (2009), 15801–15804.

[19] S. Bae, *Roll-to-roll production of 30 inch graphene films for transparent electronics*, Nature Technology **5**, no. 8 (2010), 574–578.

Chair of Modelling the Teaching and Learning Processes
University of Łódź
Pomorska 149/153, PL-90-236 Łódź
Poland
e-mail: bedastan@uni.lodz.pl

Presented by Leszek Wojtczak at the Session of the Mathematical-Physical Commission of the Łódź Society of Sciences and Arts on July 5, 2012

WYPORNOŚCIOWA FOLIA PĘCHERZYKOWA

S t r e s z c z e n i e

Opisano nowy rodzaj folii pęcherzykowej wypełnionej gazem o gęstości mniejszej, niż gęstość powietrza, np. wodorem lub helem. W wyniku tego przy odpowiednich rozmiarach pęcherzyków folia ta wykazuje siłę nośną. Przedstawiono wewnętrzną strukturę takiej folii mającej regularnie rozmieszczone sześcienne pęcherzyki i wyodrębniono jej komórkę elementarną. Przeprowadzono analizę sił działających na tę komórkę. Obliczono dla różnych gazów i grubości folii minimalną długość boku pęcherzyka, dla której siła nośna ma wartość dodatnią. Następnie wyprowadzono wzór na wartość siły nośnej działającej na jednostkę objętości folii i narysowano wykresy zależności tej siły od długości boku pęcherzyków. Opisano też eksperyment, w którym podjęto próby wytwarzania takiej folii. W wytworzonej folii następowała migracja helu przez ścianki pęcherzyków i zmniejszenie jej siły nośnej. Dlatego zaproponowano użycie folii metalizowanej do wytwarzania folii wypornościowej lub folii pokrytej grafenem. Powtórzono poprzednio wykonane obliczenia i analizy dla folii metalizowanej oraz przedyskutowano zalety pokrycia grafenem. Przeprowadzone analizy uzasadniają możliwość produkcji i zastosowań zaproponowanej folii wypornościowej.

PL ISSN 0459-6854

B U L L E T I N

DE LA SOCIÉTÉ DES SCIENCES ET DES LETTRES DE ŁÓDŹ

2013 Vol. LXIII

Recherches sur les déformations no. 2

pp. 51–63

Ewelina Z. Frątczak, José E. Prieto, and Marek Moneta

CHARACTERIZATION OF EPITAXIALLY GROWN IRON-NITRIDE THIN FILMS

Summary

In the recent years phases of Fe-nitride compounds have been the subject of many studies because iron and nitrogen are among of the most abundant elements in nature, and these elements are very interesting from a fundamental and a technological point of view. Nevertheless there is still a debate on the most efficient, exact and controlled way of obtaining thin films of the desired iron nitrides phases. Thin films of iron nitrides were deposited by Molecular Beam Epitaxy in Ultra High Vacuum conditions. We grew films of the FeN alpha (α''-$Fe_{16}N_2$), epsilon (ϵ-Fe_xN, $2 \leq x \leq 3$) and gamma (FeN_y, $y > 0.5$) phases by evaporating Fe in the presence of flow of atomic nitrogen and by post-nitriding. By changing the parameters of growth conditions we tried to obtain the α''-phase in its possible purest form. We grew the ϵ-phase mainly in a nonmagnetic form. We worked also on iron mononitride FeN which is known to exist in different phases. On the basis of room temperature Conversion Electron Mössbauer Spectroscopy accompanied with Rutherford Backscattering Spectroscopy we show our results on the growth and transformations of the samples.

Keywords and phrases: iron nitrides, thin films, MBE, Mössbauer spectroscopy, RBS, phase identification

1. Introduction

The study of the iron nitrides phase diagram is a matter of interest in the field of basic research [1–4]. On the other hand, among the applications, iron nitrides have been found to have a significant interest as materials for magnetic devices [5]. Other nitrides are used as coating materials, or catalytic properties of iron nitrides are being improved by increasing the nitrogen content in the compounds [6]. There is a strong interest in the field of spintronics to grow on semiconductors transition-metal

nitride materials which are potentially ferromagnetic [7, 8]. A potential application of iron nitrides is the transformation of an interlayer between the semiconductor and a ferromagnetic material as α-Fe.

The most common compounds are the Fe_xN phases like α'-Fe_xN ($x > 8$), α''-$Fe_{16}N_2$ (bct), γ'-Fe_4N (fcc) and ϵ-Fe_xN ($x = 2$ to 3 (hcp)). All these phases contain less than 35 at. % N and have been well investigated. The α''-$Fe_{16}N_2$ phase with a composition up to about 11 at. % N, attracted considerable attention because of a possible very high saturation magnetization, reported to vary between 2.4 and 3.2 T [9]. The largest range of homogeneity in the Fe-N system (15-33 at. % N) is exhibited by the ϵ-phase with variable Fe-to-N ratio $Fe_{2-3}N$ [10]. At the N-rich side, three phases have been predicted theoretically: γ''-FeN (ZnS-type structure) and γ'''-FeN (NaCl type structure) for nitrogen content of 50 at. % N [11–15], as well as Fe_3N_4 for higher nitrogen concentrations [16]. In this work we present new methods of growing of α-$Fe_{16}N_2$, FeN_y ($y > 0.5$) and we focus on the identification of their phases, since the growth of the α''-$Fe_{16}N_2$ phase in its pure form was rather unsuccessfully attempted by many experimental groups.

2. Experimental set-up

Thin films and multilayers of metal-nitrides were grown in UHV (Ultra High Vacuum) system with a base pressure of value lower than 10^{-10} mbar. The system was built as a series of three interconnected chambers for the different stages of preparation and growth. For the growth of iron nitride thin films, the main chamber (growth chamber) was equipped with evaporators (Knudsen-cells) for ^{57}Fe and Cu [12]. The deposition rate for each evaporator was calibrated by measuring the thickness of deposited layers by Rutherford Backscattering Spectroscopy (RBS). A typical deposition rate of ^{57}Fe was ~ 0.027 Å/s. Most of the samples were grown on polished or cleaved (001) MgO single-crystals. Prior to deposition, the MgO substrates were cleaned *in situ* by annealing at 600°C in an oxygen atmosphere (10^{-6} mbar) for 2 h in a specially designed oxygen oven integrated with the UHV system. As a source of atomic nitrogen for the growth of nitrides, a home-made Radio Frequency (RF) atomic source was developed and mounted on the UHV system. The working pressure of the UHV system was about 10^{-6}–10^{-8} mbar during growth.

Samples were grown by N-assisted ^{57}Fe deposition or by postnitriding (with atomic N or a mixture of N + H) ^{57}Fe layers epitaxially grown on (001) MgO substrates. None of the Fe-N samples were mono-crystalline. After growth and cooling to RT all the films were capped *in situ* with 5 nm of copper in order to prevent oxidation.

The Conversion Electron Mössbauer Spectroscopy (CEMS) measurements were performed in a home-made set-up with a ^{57}Co radioactive source. The conversion electrons were detected by means of a C_3H_6O gas-flow proportional counter. A pure Fe foil was used for calibration of the CEMS system. The isomer shift values are

given with respect to α-Fe at room temperature. The CEMS spectra were fitted using a computer code MCTL [17]. In this program, the spectra were analyzed by a least-square fitting routine by superimposing lines with a Voight shape, optionally folded with a Gaussian, to derive the values of the hyperfine parameters and the relative area of each sub-spectrum.

Resonant RBS was used to determine precisely the N percentage in the layers, relative to the Fe content. These measurements were performed in a high vacuum chamber connected to the 5 MV tandem accelerator [18] at the Centro de Microanálisis at the Universidad Autónoma de Madrid (CMAM/UAM). A He^{2+} beam was used for measuring the excitation curve of nitrogen. The energy of the emitted protons happens to be very close to that of the scattered α particles at the resonance energy, so the proton and α particle signals cannot be separated in our measurements. This effect has been carefully corrected [12].

The scattered ions were detected by standard Si-barrier detector located at a scattering angle of 165°. Two spectra were sequentially measured at the same spot and under the same conditions in order to check that there is no nitrogen loss during the measurements.

3. Results and discussion

Several samples were grown following a procedure leading to production of the α''-$Fe_{16}N_2$ which has nitrogen content of about 11 at. %. Also some studies have been done of the ϵ-Fe_xN ($x = 2$ to 3 (hcp)) phase which has a nitrogen composition ranging from 25 at. % N to 33 at. % N. Even though this phase is grown quite easily and is interesting, there is not much information in the literature [1, 19]. Another studied phase was γ''-FeN, with a nitrogen content close to FeN with 1 : 1 Fe to N ratio.

After growth, structural and magnetic characterization were performed in order to determine the properties of the thin iron nitride films. The stoichiometry was determined by resonant RBS. For magnetic characterization and phase identification CEMS was used.

3.1. α''-$\mathbf{Fe_{16}N_2}$

We grown this phase in its best 24 % pure phase content and we still want to improve the result. Thin iron nitride films of 10–24 nm thickness were grown by MBE, the thickness was determined by RBS. In order to find the phase occurrence with high sensitivity, the samples were analyzed by CEMS. Some facts relevant for the growth of the α''-phase are the following: the α''-phase has distorted bcc lattice configuration of the Fe sub-lattice; the best quality α''-phase is formed at a temperature of 200°C; in the Lehrer diagram the α''-phase appears at low nitriding potential of a NH_3/H_2 mixture [2, 11, 19]. Basing on these points we follwed the mentioned route to grow the α''-phase: growing a bcc ^{57}Fe of 10–20 nm thick layer at 200–230°C and applying

a postnitriding procedure at $1 \cdot 10^{-2}$ mbar for 2–4 h, at 100–200°C. As a result we increased the highest fraction from 22 % [11,19], obtained before, to 24±2 %. However there are several publications reporting higher values obtained by various methods [20–24]. We arrived at this result after several trials and applying small variations in the procedure. Postnitriding a 20 nm of ^{57}Fe at $1 \cdot 10^{-2}$ mbar for 2 h at 100°C leads only to 13.4 % of α''-phase, in this conditions also ϵ phase and ^{57}Fe mixture is formed: ϵ-$Fe_{2.1}N$ nonmagnetic (17 % (Fe III)) and ϵ-$Fe_{2.4}N$ magnetic (13.4 % (Fe II, Fe III)), ^{57}Fe (56.2 %). As is mentioned above, in addition to the α''-$Fe_{16}N_2$ phase in the sample there were present components from the ϵ-phase, which is the most easily formed phase during the deposition of iron with nitrogen. We assume that this phase is formed at the top of the sample. Another additional component was pure iron, this could mean that the nitrogen was not diffusing deep enough. The α''-phase is probably formed between the two phases. The formation a mixture of $\alpha''+\epsilon$ (without the γ'-phase) at $T < 200$°C would be in accordance with the Lehrer diagram. Our highest α''-$Fe_{16}N_2$ phase content (24 %) achieved up to now was obtained for the sample grown by postnitriding a ^{57}Fe film with a thickness of 20 nm at 200°C with a working pressure in the chamber of $6.5 \cdot 10^{-7}$ mbar and a nitrogen pressure in the source of $1.1 \cdot 10^{-2}$ mbar. The nitrogen flow was directed slightly out of the sample. In this conditions also γ''-phase is formed (singlet: 10 %, doublet: 54 % (Fig. 1)). The spectrum (Fig. 1) was fitted with two components corresponding to the phases: α''-$Fe_{16}N_2$ and γ''-phase. The α''-$Fe_{16}N_2$ phase was fitted with three components. The origin of the components in the α''-$Fe_{16}N_2$ phase is the cubic crystal structure of the cell, which contains two non-equivalent crystallographic iron sites. The corner iron atoms (Fe I) have a local cubic symmetry and consequently a zero quadrupole splitting. On the other hand, the iron atoms at the face-centered position (Fe II) have an axial symmetry and are distinguished as Fe II-A and Fe II-B sites. For the unit cell the Electric Field Gradient (EFG) tensor for the hyperfine magnetic field is perpendicular to the two axes going through the Fe II-A sites and parallel to the axis going through the Fe II-B sites [11]. The three magnetic components (sextets) corresponding to the Fe I, Fe II-A and Fe II-B sites of the α''-$Fe_{16}N_2$ phase point to a pure phase with following parameters for Fe I: $\delta = 0.001$ mm/s, $H = 33$ T, $\epsilon = 0$ mm/s, R.A. = 9%, where: δ is the isomer shift given with respect to α-Fe at room temperature, H is the hyperfine magnetic field, ϵ is the quadrupole splitting and R.A. is the relative area. For Fe II-A, we have: $\delta = 0.09$ mm/s, $H = 39$ T, $\epsilon = 0.06$ mm/s, R.A. = 18 % and for Fe II-B: $\delta = 0.11$ mm/s, $H = 32$ T, $\epsilon = -0.11$ mm/s, R.A. = 9 %. The ratio of Fe I : Fe II-A : Fe II-B is 1 : 2 : 1. On the other hand, in the spectrum shown in Fig. 1, besides the contribution of 24 % α''-$Fe_{16}N_2$, an additional phase γ''-FeN is present with a major contribution of 76 %. The fit parameters for this phase are a singlet ($\delta = 0.06$ mm/s, R.A. = 10 %) and a doublet ($\delta = 0.26$ mm/s, $\epsilon = 0.46$ mm/s, R.A. = 54 %). The relative area is the fraction of area under the curve of the corresponding subspectrum and is related with the actual phase concentration though the iron content of the FeN compound.

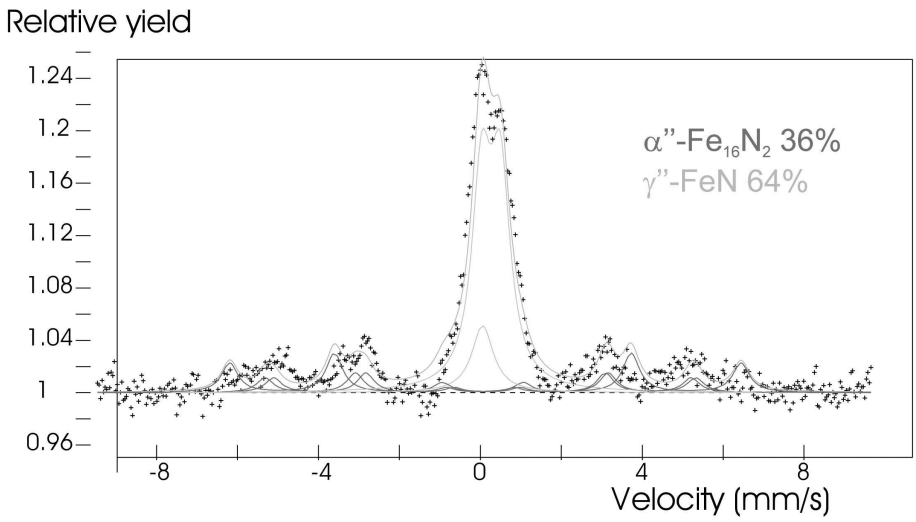

Fig. 1: Room temperature CEMS spectrum for the sample with the highest content in α''-$Fe_{16}N_2$ (24 %). The given numbers are the relative areas measured under the subspectra. The y-axis represent the number of counts and is normalized to the background of the signal.

We also applied a low temperature treatment in order to avoid or suppress bcc to fcc/hexagonal transitions and we added H_2 to the gas in the RF source to lower the chemical potential at the sample surface, in analogy with the NH_3/H_2 mixture in the Lehrer diagram. This resulted in the formation of different phases but no α''-phase was grown. Few samples were grown increasing a little bit the pressure of the nitrogen from $1{\cdot}10^{-2}$ mbar to $1.3{\cdot}10^{-3}$ mbar or lowering the temperature from 200°C to 150°C and 100°C. This procedure leads to γ''-phase formation accompanied with some paramagnetic ϵ-phase, as well as shortering the nitriding time from 2 h to 15 min. The same result comes out in case of keeping the sample after nitriding longer at the same temperature as it was during nitriding. For example, for $t = 10$ min of nitriding, the sample was kept at $T = 150$°C, for 3 h 50 min. Lowering the temperature to 100°C and to RT leads to formation of γ''-phase and iron. Nitriding the ^{57}Fe with a mixture of N_2 and H_2 at RT, maintaining the pressure at $1 \cdot 10^{-2}$ mbar does not influence the γ'' and ^{57}Fe formation. We also tried to change the goniometer position keeping the rest of the parameters as it was for α''-$Fe_{16}N_2$ growth (20 nm of ^{57}Fe nitrided for 2 h at $1 \cdot 10^{-2}$ mbar, $T = 200$°C) and we received 100 % of γ''-phase instead. Nitriding a sample with mixture of N_2 and H_2 at 150°C and $P_{N+H} = 1.3 \cdot 10^{-2}$ mbar, keeping the rest of parameters as it was for α''-$Fe_{16}N_2$ growth, gives contribution of γ''-phase formation accompanied with some magnetic and nonmagnetic ϵ-phase and Fe.

For all the samples mentioned here the working pressure in the chamber during N exposure was about $1.2 \cdot 10^{-6} - 3 \cdot 10^{-8}$ mbar.

We also studied the thermal stability of the α''-$Fe_{16}N_2$ phase. After growth, the sample was found to be a mixture of phases: α'', ϵ, and ^{57}Fe. After one year and a half the composition of the sample was checked out by Mössbauer spectroscopy, but no significant changes were found. Then the sample was heated up in three steps. At first to 150°C for 30 min, no changes were observed in a Mössbauer spectrum. In the second step the sample was heated up to 150°C for 1 h, no changes observed in the composition. In the third step the sample was heated again up to 150°C for 2 h, but again no changes were visible.

3.2. ϵ-Fe_xN

The ϵ-Fe_xN phase is the easiest one to obtain and we could grow films of 100 % purity of this phase by postnitriding of a ^{57}Fe sample in the presence of a flow of atomic nitrogen or a mixture of hydrogen and nitrogen. After evaporation of 20 nm of ^{57}Fe at 300°C, keeping the temperature we applied postnitriding for 2 h in N_2 atmosphere at pressure of $5 \cdot 10^{-2}$ mbar. As a result we received 15 % contribution of ϵ-Fe_xN from Mössbauer spectrum. In this conditions also γ''-phase was formed, what was found also by others [11], with fractions of singlet 42 % and of doublet 43 %. We obtained 100 % of ϵ-phase by postnitriding of ^{57}Fe sample in presence of hydrogen and nitrogen mixture from RF atomic source. Possibly, the hydrogen at the surface is changing the potential for recombination of nitrogen atoms into nitrogen molecules. This method was applied to grow a sample in the following way: postnitriding of 20 nm thick sample in N(29 %) + H(71 %) mixture for 4 h at 200°C with a pressure of gas mixture at the source of $P_{N+H} = 1.4$ mbar and working pressure at the growth chamber of $2 \cdot 10^{-7}$ mbar. CEMS spectra show that all Fe was converted into 100 % of ϵ-Fe_xN phase. The Mössbauer spectrum of this sample (Fig. 2) was fitted using the parameters for the ϵ-Fe_xN phases, both nonmagnetic and magnetic. The ϵ-Fe_xN phase has a hexagonal close-packed (hcp) structure. The major nonmagnetic phase corresponds to ϵ-$Fe_{2.1}N$. Nonmagnetic fraction implies that the concentration of N is above 30 at. % [1,19]. The spectrum attributed to this phase was fitted with a doublet for Fe III sites for the Fe atoms in the hcp unit cell. The fit parameters for Fe III were: $\delta = 0.37$ mm/s, R.A. = 88 %. The spectrum of the magnetic phase ϵ-$Fe_{2.4}N$ with a total R.A. = 12 % was fitted with two sextets for the Fe II and Fe III Fe sites with the following parameters for Fe II: $\delta = 0.28$ mm/s, $H = 30$ T, $\epsilon = 0$ mm/s, R.A. = 4 % and for Fe III: $\delta = 0.35$ mm/s, $H = 20$ T, $\epsilon = 0$ mm/s, R.A. = 8 %.

Another sample was grown by alternate nitriding and ^{57}Fe evaporating every 1 min, repeated 30 times, at 70°C and pressure in the chamber was $P = 1 \cdot 10^{-2}$ mbar and as a result mainly ϵ-Fe_xN magnetic phase was formed with nonmagnetic component 31.44 % and magnetic component 61.13 %. There is additional singlet fit: 7.43 %. Several samples were grown by simultaneous ^{57}Fe evaporation and nitriding. The sample grown at 300°C at $5 \cdot 10^{-2}$ mbar for 57 min had 24 nm and the composition was: 31.77 % of paramagnetic ϵ-Fe_xN and singlet: 29.77 % and doublet: 38.46 % of γ''-phase. Other sample grown at 300°C at $1 \cdot 10^{-1}$ mbar for 57 min had

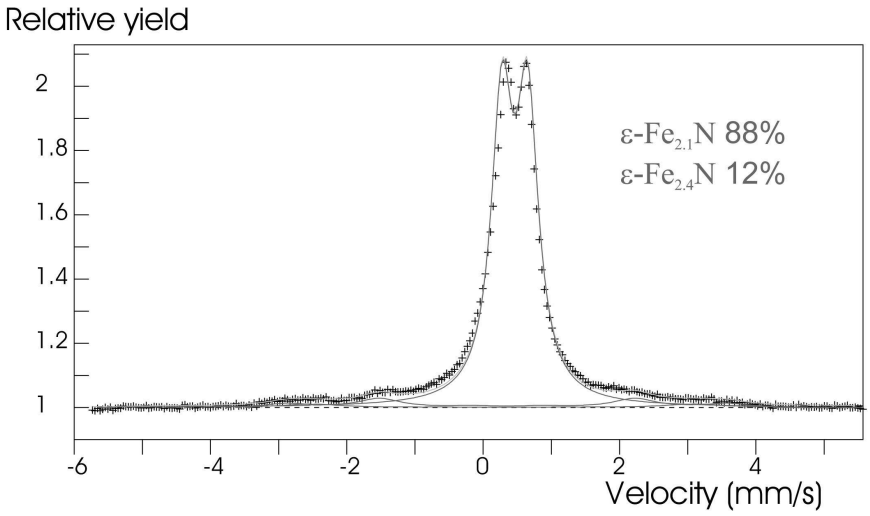

Fig. 2: Room temperature CEMS spectrum for the ϵ-Fe$_x$N sample. The given numbers are the relative areas measured under the subspectra. The y-axis represent the number of counts and is normalized to the background of the signal.

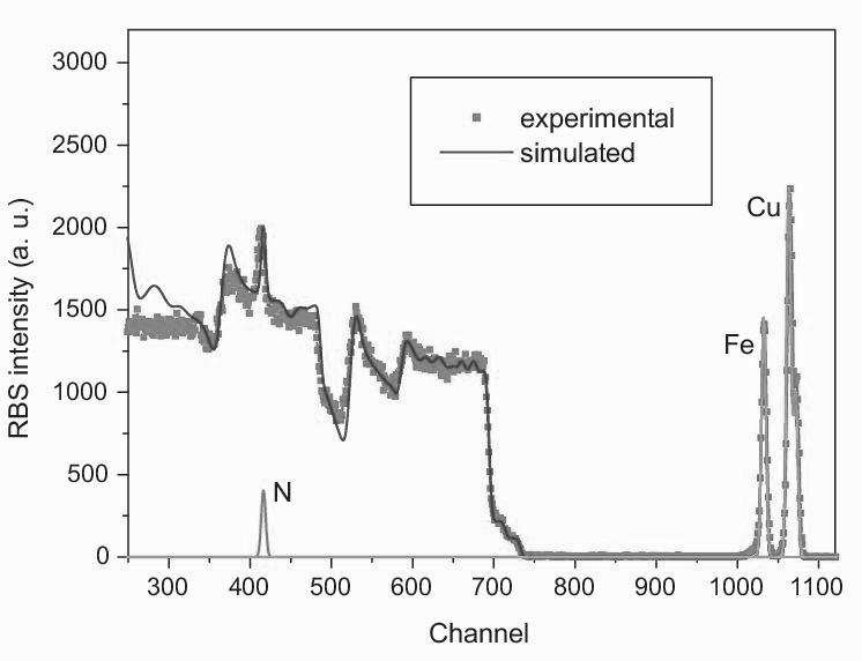

Fig. 3: RBS spectrum for the sample containing the ϵ-Fe$_x$N phase measured at 3.7 MeV.

24 nm with the composition: 22.17 % of paramagnetic ϵ-Fe_xN and singlet: 23.31 % and doublet: 54.52 % of γ''-phase.

Fig. 3 shows an illustrative RBS spectrum of ϵ-Fe_xN phase grown by simultaneous ^{57}Fe evaportion and nitriding at 408°C for 1 h and 36 min. The experimental data were simulated and fitted by SIMNRA program [25]. The sample thickness was 8 nm (here the evaporation rate was very low), the working pressure was $6.2 \cdot 10^{-6}$ mbar and the nitrogen pressure was $5 \cdot 10^{-2}$ mbar.

From few samples grown at the same conditions: simultaneous 40 nm ^{57}Fe evaporation and nitriding at 408°C at $1 \cdot 10^{-1}$ mbar for 1 h 36 min, we obtained different results. First sample: 100 % of ϵ-phase: 65.29 % of nonmagnetic and 34.71 % of magnetic component. Second sample: 100 % of ϵ-phase, 92.7 % nonmagnetic and 7.3 % of magnetic components. Third and fourth sample: 100 % of paramagnetic ϵ-Fe_xN. In the case of nitride films grown by postnitriding in the presence of high fluxes of nitrogen, and at temperature of 300°C the samples grown were found to be mixtures of the ϵ- and γ''-phases. Nitriding in a $NH_3 + H_2$ mixture gave 100 % of ϵ-phase. Simultaneous evaporation of ^{57}Fe and nitriding at 300°C gave mixture of ϵ- and γ''-phases and at 408°C gave 100 % of ϵ-phase.

For all the samples mentioned here, the working pressure in the chamber during N exposure was between $6.9 \cdot 10^{-6}$ and $3 \cdot 10^{-7}$ mbar.

3.3. γ''-FeN_y ($y > 0.5$)

These N-rich phases are theoretically predicted to coexist. According to the calculations, as stoichiometric phases, both should have a nitrogen content of 50 at. % N but with different configuration of the N atoms within the fcc Fe cage. The two structures correspond to the ZnS-type for γ''-FeN phase and a NaCl-type for the γ'''-FeN. The coexistence of these phases or the existence of only one phase still is a matter of controversy. Relying on already published results [2, 12–15, 19, 26] we assume that the samples grown in our work contain pure γ''-FeN phase with a high fraction of vacancies.

Fig. 4 shows an RBS spectrum of the 18 nm sample grown by simultaneous ^{57}Fe evaporation and nitriding at a temperature of 150°C and at nitrogen pressure $1 \cdot 10^{-1}$ mbar for 1 h. The working pressure was $6.8 \cdot 10^{-6}$ mbar. The Mössbauer result is shown in Fig. 5 and is 100 % of γ''-FeN_y ($y > 0.5$) phase. In our work this nonmagnetic phase was fitted with a singlet and a doublet. The singlet corresponds to a pure γ''-FeN phase and the doublet is associated to the different, inequivalent positions of iron atoms in the same phase: γ''-FeN with vacancies. The high doublet-to-singlet ratio means that the content of the phase with vacancies is significant, so the real N-to-Fe ratio deviates from the 1 : 1 assumption. This is also visible in the RBS spectrum of Fig. 4. Calculations confirmed that the Fe-to-N ratio is the same in the RBS and Mössbauer spectra of this sample. The Mössbauer fit parameters for the singlet are: $\delta = 0.006$ mm/s, R.A. = 24 % and for the doublet: $\delta = 0.26$ mm/s, ϵ=0.46 mm/s, R.A. = 76 %.

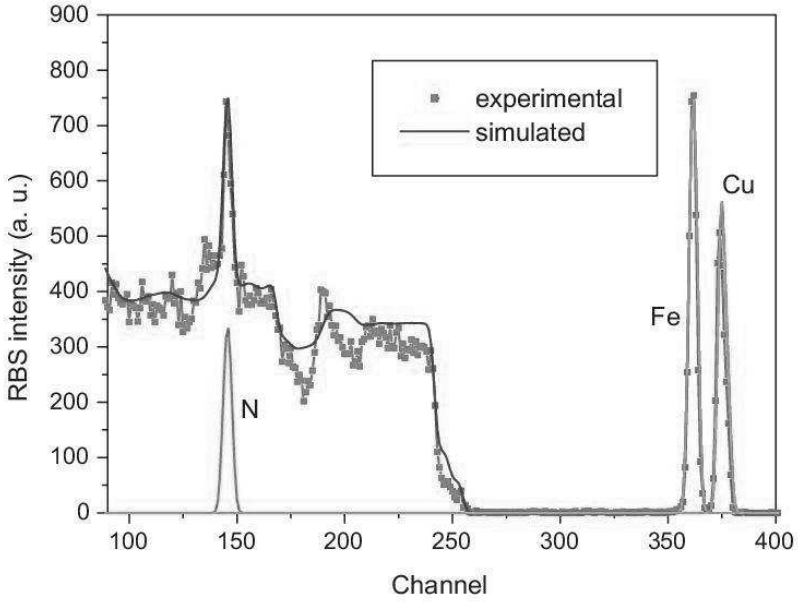

Fig. 4: RBS spectrum for the sample containing the γ''-FeN phase with vacancies. The nitrogen peak compared to the iron peak does not show a 1 : 1 FeN proportion of N and Fe because of the vacancies content. The sample was measured using a 3.7 MeV beam.

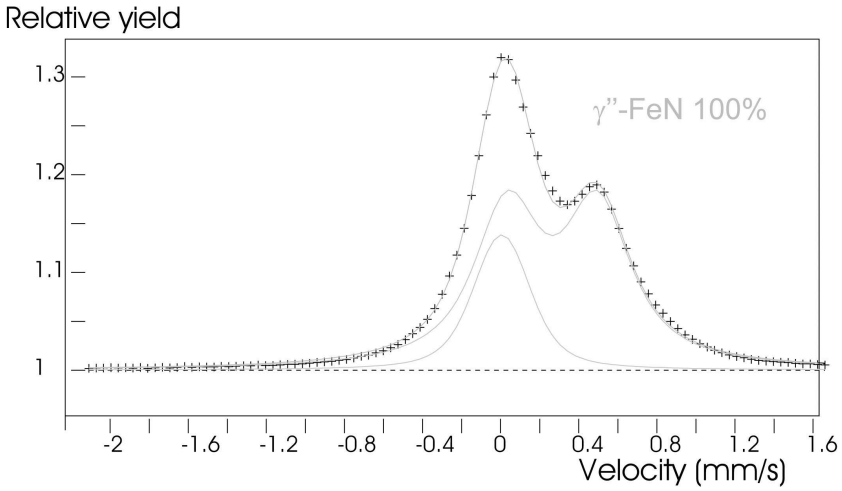

Fig. 5: Room temperature CEMS spectrum for the γ''-FeN sample. The given numbers are the relative areas measured under the subspectra. The y-axis represent the number of counts and is normalized to the background of the signal.

The influence of time exposure was also studied. A composition of the Mössbauer analysis made just after growth and made after two years proved that time exposure induced a transition of a part of the phase containing vacancies to an ϵ-phase. After two years the fraction of phase containing vacancies decreased by $13 \pm 3\,\%$ and according to the reaction which takes place during the phase transformation: Fe(N-vacancy) + FeN$\rightarrow$Fe$_2$N, the ϵ fraction increased by $1 \pm 0.25\,\%$, in a fraction 13 times smaller than the decrease of the fraction containing vacancies. If the vacancy is surrounded by 14 Fe atoms and this vacancy is capped by one N atom, then the 13 Fe atoms are left without vacancy, so the phase containing vacancies decreases 13 times. At the same time, the increase of the ϵ-phase is only by one Fe atom.

Actually the Mössbauer analysis proved the result predicted by the reaction above (see Figs. 5 and 6). After 2 years time exposure the spectrum acquired (Fig. 6) from the sample shows the γ''-FeN phase measured before (Fig. 5). Apart of the components of the γ''-FeN phase, another ϵ-Fe$_{2.1}$N paramagnetic phase appeared. The fit components for the γ''-FeN phase are a singlet: $\delta = -0.03\,\mathrm{mm/s}$, R.A. = 33 % and a doublet: $\delta = 0.3\,\mathrm{mm/s}$, $\epsilon = 0.4\,\mathrm{mm/s}$, R.A. = 66 %. For ϵ-Fe$_{2.1}$N doublet: $\delta = 0.3\,\mathrm{mm/s}$, $\epsilon = 0.2\,\mathrm{mm/s}$, R.A. = 1 %. Here the phase content is 99.5 % for the γ''-FeN phase and 0.5 % for the ϵ-Fe$_{2.1}$N phase.

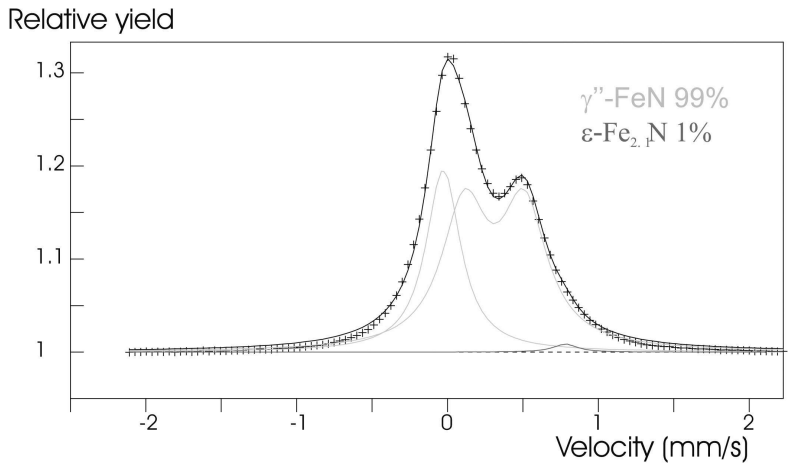

Fig. 6: Room temperature CEMS spectrum for the γ''-FeN sample after time exposure. The given numbers are the relative areas measured under the subspectra. The y-axis represent the number of counts and is normalized to the background of the signal. The bottom line corresponds to the ε-Fe$_{2.1}$N-face.

By the same method and the same growth parameters as before, but with the growth time 47 min and thickness 20 nm, we received this phase with singlet 16.84 % and doublet 83.16 %. By fixing the growth conditions we were able to reproduce the composition of the sample and grow other samples with different thicknesses. Another 36 nm sample grown at 50°C for 2 h at the same pressure as before gave the

result of singlet 12.41 % and doublet 84.51 %. Next two 44 nm samples were grown still at the same pressure but at 350°C for 1 h 46 min. The single phase content was 15.24 % and 19.19 %, and doublet 84.76 % and 80.81 % respectively. For all the samples mentioned here the working pressure in the chamber during N exposure was between $8.5 \cdot 10^{-6}$ and $4.5 \cdot 10^{-7}$ mbar.

In general, this phase was intended to grow in the range of temperatures from RT to 547°C. The purest phase was grown at 250°C. Above 350°C, ϵ-phase was grown.

Thermal stability was studied for several samples. A sample grown at RT (and fitted with two singlet lines) was heated up to 300°C for 1 h and maintained the first singlet with a lower isomer shift, but the second singlet with a higher isomer shift vanished. Heating again up to 400°C for 1 h resulted in the appearance of an oxide layer. After increasing the heating up to 450°C for 1 h, oxidized iron was formed. Another sample grown at 300°C (also fitted with two singlets) was heated up to 200°C for 1 h. It lost the singlet fraction, a doublet fraction appeared and the second singlet remained unchanged. Next, it was heated up to 300°C for 1 h: the second singlet started to increase and the doublet decreased. While the sample was heated up to 350°C for 1 h, oxidation occurred.

4. Conclusions

The synthesis of thin films of Fe nitrides: α''-, ϵ- and γ''-phases were described. Many attempts were done and different combinations of growth parameters were tried in order to obtain pure phases in a controlled way. N-assisted MBE and/or postnitriding can be applied successfully to produce most of the existing iron nitride phases. Depending on growth parameters such as deposition temperature, pressure of nitrogen and hydrogen in the RF atomic source, different phases were grown. The metastable character of all iron nitrides makes deposition temperature a key factor in determining which phase is formed. The highest, 24 % fraction of α''-$Fe_{16}N_2$ was obtained by postnitriding an epitaxial Fe layer at 200°C. By postnitriding of ^{57}Fe with a mixture of N and H at a temperature of 200°C we obtained 100 % of paramagnetic ϵ-$Fe_{2.1}N$ phase. At low deposition temperatures (below 150°C) and high pressures of nitrogen, N-assisted MBE growth was applied to the growth of nitride phases present at the high nitrogen-content side of the phase diagram. We claim that γ''-FeN_y ($y > 0.5$) is formed. Although the Mössbauer fits show the existence of two phases, singlet and doublet, we attribute the singlet to the pure γ''-FeN phase with ZnS structure and the doublet to the γ''-FeN phase containing vacancies. The additional phase could be also the γ'''-FeN phase, although we do not have strong evidence for this.

Acknowledgment

Financial support by the Spanish MiCInn through projects FIS2008-01431 and FIS2011-23230 is gratefully acknowledged.

References

[1] S. Grachev, D. M. Borsa, S. Vongtragool, and D. O. Boerma, Surf. Sci. **482–485** (2001), 802.

[2] M. Gupta, A. Gupta, P. Bhattacharya, P. Misra, and L. M. Kukreja, J. Alloy. Compd. **326** (2001), 265.

[3] N. I. Kardonina, A. S. Yurovskikh, and A. S. Kolpakov, Met. Sci. Heat Treat. **52** (2010), 454.

[4] D. Moszyński, I. Moszyńska, and W. Arabczyk, Mater. Lett. **78** (2012), 32.

[5] P. Schaaf, Prog. Mater. Sci. **47** (2002), 1.

[6] M. Zheng, X. Chen, R. Cheng, N. Li, J. Sun, X. Wang, and T. Zhang, Catal. Commun. **7** (2006), 187.

[7] B. A. Orlowski, I. A. Kowalik, B. J. Kowalski, N. Barrett, I. Grzegory, and S. Porowski, J. Alloy. Compd. **423** (2006), 136.

[8] W. Lin, J. Pak, D. C. Ingram, and A. R. Smith, J. Alloy. Compd. **463** (2008), 257.

[9] S. Atiq, H.-S. Ko, S. A. Siddigi, and S.-C. Shin, J. Alloy. Compd. **479** (2009), 755.

[10] T. Liapina, A. Leineweber, E. J. Mittemeijer, and W. Kockelmann, Acta Mater. **52** (2004), 173.

[11] D. M. Borsa, Doctoral Thesis, Acad. Building, Broestraat 5, 9712 GP, Groningen 2004.

[12] E. Andrzejewska, R. Gonzalez-Arrabal, D. Borsa, and D. O. Boerma, Nucl. Instrum. Meth. B **249** (2006), 838.

[13] C. Navío, J. Álvarez, M. J. Capitán, F. Yndurain, and R. Miranda, Phys. Rev. B **78** (2008), 155417.

[14] I. Jouanny, P. Weisbecker, V. Demange, M. Grafouté, O. Peña, and E. Bauer-Grosse, Thin Solid Films **518** (2010), 1883.

[15] M. Gupta, A. Tayal, A. Gupta, V. Raghavendra Reddy, M. Horisberger, and J. Stahn, J. Alloy. Compd. **509** (2011), 8283.

[16] W. Y. Ching, Y.-N. Xu, and P. Rulis, Appl. Phys. Lett. **80** (2002), 2904.

[17] http://pleiterborg.nl/nvsf/software/CIO/

[18] A. Rivera, R. Andrzejewski, A. Guirao, R. González Arrabal, E. Andrzejewska, N. Gordillo, J. E. Prieto, and D. O. Boerma, Nucl. Instrum. Meth. B **249** (2006), 935.

[19] D. M. Borsa and D. O. Boerma, Hyperfine Interact. **151–152** (2003), 31.

[20] K. Nakajima, T. Yamashita, M. Takata, and S. Okamoto, J. Appl. Phys. **70** (1991), 6033.

[21] M. Q. Huang, W. E. Wallace, S. Simizu, and S. G. Sankar, J. Magn. Magn. Mater. **135** (1994), 226.

[22] J. M. D. Coey, K. O'Donnell, Q. Qi, E. Touchais, and K. H. Jack, J. Phys.: Condens. Matter. **6** (1994), L23.

[23] P. Bezdicka, A. Klarikova, I. Paseka, and K. Zaveta, J. Alloy. Compd. **274** (1998), 10.

[24] J. M. D. Coey and P. A. I. Smith, J. Magn. Magn. Mater. **200** (1999), 405.

[25] http://www.rzg.mpg.de/ mam/

[26] R. Usui, Y. Yamada, and Y. Kobayashi, Hyperfine Interact. **205** (2012), 13.

Centro de Microanálisis de Materiales
Dpto. de Física de la Materia Condensada
and
Instituto "Nicolás Cabrera"
Universidad Autónoma de Madrid
E-28049 Madrid
Spain

Department of Solid State Physics
University of Łódź
Pomorska 149/153, PL-90-236 Łódź
Poland
e-mail: ewelinazofia@gmail.com

Presented by Marek Moneta at the Session of the Mathematical-Physical Commission of the Łódź Society of Sciences and Arts on June 18, 2013

CHARAKTERYZACJA WYTWORZONYCH EPITAKSJALNIE CIENKICH FILMÓW AZOTKÓW ŻELAZA

S t r e s z c z e n i e

W ciagu ostatnich lat fazy zwiazków azotków żelaza były przedmiotem wielu badań, gdyż azot i żelazo znajdują się wsród pierwiastków najczęściej występujacych w naturze, a także są interesujące ze wzgledu na badania fundamentalne oraz zastosowanie technologiczne. Niemniej jednak, ciągle prowadzona jest debata nad najbardziej wydajnym, dokładnym i kontrolowanym sposobem otrzymywania cienkich warstw odpowiednich faz azotków żelaza. Cienkie filmy azotków żelaza były nanoszone metodą Epitaksji z Wiązek Molekularnych w warunkach Ultra Wysokiej Próżni. Przygotowano warstwy FeN faz alfa (α''-$Fe_{16}N_2$), epsilon (ϵ-Fe_xN, $2 \leq x \leq 3$) i gamma (FeN_y, $y > 0.5$) poprzez osadzanie żelaza w obecności strumienia atomowego azotu i przez post-azotowanie. Zmieniając parametry warunków wzrostu próbowano uzyskać fazę α w możliwie najczystszej postaci. Wytworzono fazę ϵ głównie w formie niemagnetycznej. Pracowano również nad azotkiem żelaza FeN, o którym wiadomo, że posiada różne fazy. Na podstawie techniki Spektroskopii Mössbauerowskiej Elektronów Konwersyjnych w temperaturze pokojowej i Spektroskopii Rozpraszania Wstecznego Rutherforda przedstawiono rezultaty wzrostu i transformacji faz.

PL ISSN 0459-6854

B U L L E T I N

DE LA SOCIÉTÉ DES SCIENCES ET DES LETTRES DE ŁÓDŹ

2013 Vol. LXIII

Recherches sur les déformations no. 2

pp. 65–77

Savvas Mitridis, Dimitra Georgakaki, and Hariton M. Polatoglou

FINITE ELEMENT STUDY OF THE METROLOGICAL ASPECTS OF ATOMIC FORCE MICROSCOPE CANTILEVERS

Summary

In this paper we compare two different calibration methods for cantilevers used in contact mode Atomic Force Microscopy: the dimensional method and the finite element method (FEM). Each method is used for the accurate calculation of the normal cantilever stiffness k_z, a parameter crucial for the AFM images acquired with a constant-force load. The dimensional method was restricted to tipless rectangular and trapezoidal cantilevers whereas FEM allowed us to compare levers of different geometries: tipless rectangular, tipless trapezoidal 2D, tipless trapezoidal 3D and trapezoidal 3D with a pyramidal tip at the free end. The FE models were initially validated by the equations provided by beam theory and data from literature and then were used to produce our results.

Keywords and phrases: atomic force microscope, cantilever calibration, finite element method

1. Introduction

Calibration of atomic force microscope (AFM) cantilevers has been a crucial issue in modern nanometrology applications and especially in mechanical and dimensional measurements at the nanoscale [1, 2]. A lot of work has been done with the use of the nominal value of the cantilever stiffness, provided by the manufacturer's specifications, but it has been proven, that this could lead to erroneous results either for static or for dynamic cantilevers [3].

Today, the methodologies applied in cantilever calibration are divided into three main categories: The dimensional methods are based on the measurement of the geometrical properties of the cantilever as well as the sample elastic properties [4].

These methodologies are easy to implement for rectangular cantilevers but for complex geometries such as V-shaped, A-shaped or trapezoid cantilevers, a comparison and/or combination with Finite Element Models [5, 6] is often mandatory for obtaining more accurate results. The static experimental methods are based on the direct measurement of reference properties, such as cantilever of known stiffness [7, 8], particles of known mass attached to the cantilever end [9], reference artefacts [10] etc. The dynamic methods are based on the cantilever's resonant response f_0 and they require accurate measurement of the cantilever's plan view dimensions. The most widely used techniques are: Cleveland method [11], Sader method [12] and thermal noise method [13]. A thorough review by Cook et al [14] presents in detail and compares the experimental implementations of Sader and thermal noise methods.

In this work we use a combination of computational and theoretical methods in order to calibrate cantilevers used in contact mode atomic force microscopy. More specifically, we perform cantilever dimensional measurements based on beam theory and we calculate k_z assuming a perfect rectangular geometry as well as a trapezoidal one. Using the results from the above dimensional analysis we construct realistic FE models of various geometries. Initially we modeled a simple tipless rectangular lever as well as a trapezoidal tipless lever, compared directly to the results from beam theory. Additionally, we created levers with a 3D trapezoidal cross-section with/without tip and finally 3D trapezoidal levers with a tip and an etched free end. Useful conclusions arise from the intercomparisons between different FE models as we move from the simplest rectangular geometry to more complex approaches.

2. Mathematical tools and methods

A beam is an horizontal or vertical structural element that is capable of withstanding load primarily by resisting bending. The bending force induced into the material of the beam is a result of the external loads, own weight, span and external reactions to these loads. The beams are characterized by their length, their cross sectional shape and the material used. Supports of the beam limiting lateral or rotational movements, so as to meet the conditions of stability, as well as to limit deformation to a certain allowance. A beam with a laterally and rotationally fixed support at one end with no support at the other end is called a cantilever beam.

In this paper we will assume that the AFM cantilever behaves as a homogeneous and isotropic beam. This is based on the simplicity of the analytical method followed and also the fact that we are studying only the contact mode of the microscope. The most common theories that have developed are the Timoshenko and the Euler-Bernoulli theory. However there are other similar theories that take into account other parameters of the problem and lead to higher order differential equations. The boundary conditions vary depending on how the beam is supported. So we can consider the AFM cantilever as being clamped to the one end (to the holder) and

free to the other. At the fixed end of the beam there will be no deflection and there will not be any sloping present either. At the free end of the beam there will be no bending moment and there is also no shear force present at the utmost edge of the beam. Below we attempt a more extensive report on two of these theories (Timoshenko and Euler-Bernoulli) and, simultaneously, the justification of the use of the classical theory in this paper, by comparing the two theories.

2.1. Timoshenko beam theory and Euler-Bernoulli beam theory

The model takes into account shear deformation and rotational inertia effects, making it suitable for describing the behaviour of short beams, sandwich composite beams or beams subject to high-frequency excitation when the wavelength approaches the thickness of the beam. The resulting equation is of 4th order, but unlike ordinary beam theory – i.e. Bernoulli-Euler theory – there is also a second order spatial derivative present. Physically, taking into account that the added mechanism of deformation effectively lowers the stiffness of the beam, while the result is a larger deflection under a static load and lower the predicted eigenfrequencies for a given set of boundary conditions. The latter effect is more noticeable for higher frequencies as the wavelength becomes shorter, and thus the distance between opposing shear forces decreases.

If the shear modulus of the beam material approaches infinity – and thus the beam becomes rigid in shear – and if rotational inertia effects are neglected, Timoshenko beam theory converges towards ordinary beam theory. In static Timoshenko beam theory [15] without axial effects, the displacements of the beam are assumed to be given by:

$$u_x(x, y, z) = -z\psi(x), \tag{1}$$

$$u_y(x, y, z) = 0, \tag{2}$$

$$u_z(x, y, z) = w(x), \tag{3}$$

where x, y, z are are the coordinates of a point in the beam, and u_x, u_y and u_z are the components of the displacement vector in the three coordinate directions, ψ is the angle of rotation of the normal to the mid-surface of the beam and w is the displacement of the mid-surface in the z-direction.

The governing equations are the following uncoupled system of ordinary differential equations:

$$\frac{d^2}{dx^2}(EI\frac{d\psi}{dx}) = q(x), \tag{4}$$

$$\frac{dw}{dx} = \psi - \frac{1}{KAG}\frac{d}{dx}(EI\frac{d\psi}{dx}). \tag{5}$$

Combining the two equations gives, for a homogeneous beam of constant cross-section,

$$\frac{d^4w}{dx^4} = q(x) - \frac{EI}{KAG}\frac{d^2q}{dx^2}. \tag{6}$$

Euler Bernoulli's Beam Theory [15] also known as engineer's beam theory or classical beam theory (CBT) is a simplification of the linear theory of elasticity which provides a means of calculating the load carrying and deflection characteristics of beams. It covers the case for small deflections of a beam which is subjected to lateral loads only. It is thus a special case of Timoshenko beam theory which accounts for shear deformation and is applicable for thick beams. The two key assumptions in the Euler-Bernoulli beam theory are that the material is linear elastic according to Hooke's law and that plane sections remain plane and perpendicular to the neutral axis during bending. The latter is sometimes referred to as Navier's hypothesis. In contrast, and as mentioned above, Timoshenko beam theory relaxes the assumption that the sections remain perpendicular to the neutral axis, thus including shear deformation.

The Euler-Bernoulli equation describes the relationship between the beam's deflection and the applied load:

$$\frac{d^2}{dx^2}\left(EI\frac{d^2w(x)}{dx^2}\right) = q. \tag{7}$$

The curve $w(x)$ describes the deflection of the beam in the z direction at some position x (the beam is modeled as a one-dimensional object), q is a distributed load, in other words a force per unit length (analogous to pressure being a force per area). Note that E is the elastic modulus and that I is the second moment of area. I must be calculated with respect to the centroid axis perpendicular to the applied loading. For an Euler-Bernoulli beam, which is not under any axial loading, this axis is called the neutral axis.

Often, EI is a constant, so that gives:

$$EI\frac{d^4w(x)}{dx^4} = q. \tag{8}$$

This equation, describing the deflection of a uniform, static beam, is used widely in practice and this is our choice for modeling an AFM cantilever beam.

Successive derivatives of w have important meanings where w is the deflection in the z direction, so:

1. w is the deflection of the beam,
2. dw/dx is the slope of the beam,
3. $M = -EI\ (d^2w/dx^2)$ is the bending moment of the beam,

4. $Q = -d(EId^2w/dx^{2)}/dx$ is the shear force in the beam.

The stresses in a beam can be calculated from the above expressions after the deflection due to a given load has been determined. The beam equation contains a fourth-order derivative in x. To find a unique solution $w(x,t)$ we need four boundary conditions. The boundary conditions usually model supports but they can also model point loads and moments. The supports or displacement boundary conditions are used to fix values of displacement w and rotation dw/dx on the boundary (Dirichlet boundary conditions). In our problem the fixed end of the cantilever can not accept any displacement or rotation. This means that at the fixed end both deflection and slope are zero. Since no external bending moment is applied at the free end of the beam, the bending moment at that location is zero. In addition, if there is no external force applied to the beam, the shear force at the free end is also zero.

For a rectangular cantilever which is subject to free oscillation, if the system is assumed as continuous and if the mass of the beam is considered to be distributed linearly with the axis of the beam, then the normal stiffness k_z is given by:

$$k_z = \frac{3EI}{L^3} = \frac{Ewt^3}{4L^3}, \tag{9}$$

where E is the Young's modulus of the cantilever material, $I = wt^3/12$ is the moment of inertia for a rectangular cross section and L, w, t are the length, width and thickness lever respectively.

In most cases, the cantilever has a trapezoidal cross section that deviates from the ideal rectangular one [16], thus the normal stiffness is given by

$$k_z = \frac{3EI}{L^3} = \frac{E(a^2 + 4ab + b^2)t^3}{12(a+b)L^3}, \tag{10}$$

where E is the Young's modulus of the cantilever material,

$$I = (a^2 + 4ab + b^2)t^3/12(a+b)L^3$$

is the moment of inertia for a trapezoidal cross section, L and t are the length and thickness lever respectively, a and b are the widths of the trapezoidal cross section and $(a+b)/2$ is the effective mean width if the lever is assumed to be rectangular [17].

2.2. Finite element analysis

The finite element method [18, 19] (FEM) (its practical application often known as finite element analysis (FEA)) is a numerical technique for finding approximate solutions to (linear or linearized) partial differential equations (PDE) and their systems, as well as (less often) integral equations. In simple terms, FEM is a method for dividing up a very complicated problem into small elements that can be solved in relation to each other and is considered as a special case of the more general Galerkin method with polynomial approximation functions. The solution approach

is based on eliminating the spatial derivatives from the PDE. This approximates the PDE with a system of algebraic equations for steady state problems or a system of ordinary differential equations for transient problems. These equation systems are linear if the underlying PDE is linear, and vice versa. Algebraic equation systems are solved using numerical linear algebra methods.

The basic idea in the finite element method is to find the solution of a complicated problem by replacing it by a simpler one. Since the actual problem is replaced by a simpler one in finding the solution, we will be able to find only an approximate solution rather than the exact solution. Moreover, in the finite element method, it will often be possible to improve and refine the approximate solution by spending more computational effort.

In the finite element method, the actual continuum or body of matter, such as a solid, liquid, or gas, is represented as an assemblage of subdivisions called finite elements. These elements are considered to be interconnected at specified joints called nodes or nodal points. The nodes usually lie on the element boundaries where adjacent elements are considered to be connected. Since the actual variation of the field variable (e.g., displacement, stress, temperature, pressure, or velocity) inside the continuum is not known, we assume that the variation of the field variable inside a finite element can be approximated by a simple function. These approximating functions (also called interpolation models) are defined in terms of the values of the field variables at the nodes. When field equations (like equilibrium equations) for the whole continuum are written, the new unknowns will be the nodal values of the field variable. By solving the field equations, which are generally in the form of matrix equations, the nodal values of the field variable will be known. Once these are known, the approximating functions define the field variable throughout the assemblage of elements.

In all FEM variants there are always the same sequence of steps to be taken :

1. Discretization of the continuum : divide the solution into smaller regions that we call elements. The elements are contained inside a certain number of points (nodes). The elements can take several shapes. From segments of lines, triangles, squares, etc, to curved elements. The problem to be solved is what determines the shapes of the finite elements. For example, for a 1D problem, like a cylindrical rod with radial symmetry, the simplest is to take the elements as linear segments with two nodes per segment. For a 2D problem, the simplest can be using triangular elements.

2. Select the type of trial function to use and in turn the shape functions: We select what kind of functions we will take to describe the variation of the function ϕ inside each element (the trial function). This is equivalent to say, that we select the basis set of functions that will describe our solution. One of the usual choices is to take a polynomial like for instance $\varphi(x) = \phi_0 + \phi_1 x$ (known as linear element) or $\varphi(x) = a_0 + a_1 x + a_2 x^2$ (known as quadratic element). If we have n unknown coefficients $\alpha_0, \alpha_1, \alpha_2, \alpha_3, \ldots, \alpha_{n-1}$ we will need the element to have n nodes to be

able to determine them. It is easy to show that the value of our trial function φ for a given position x inside an element can be written as a function of the values of φ at the N nodes the of element ($[\varphi_1,\ \varphi_2,\ ...,\ \varphi_N]$) , i.e. $\varphi(x) = [\varphi] \cdot [N] = [\varphi_1, \varphi_2, \ldots, \varphi_N] \cdot [N_1(x), N_2(x), \ldots, N_N(x)]$ where the $N_i(x)$, $i = 1, ..., N$, are known as the shape functions.

3. The formulation: Given the PDE you want to solve, now you must find a system of algebraic equations for each element "e" such that by solving it you obtain the values of of φ at the position of nodes of the element "e" ($[\varphi 1, \varphi 2, \ldots, \varphi N]'[\varphi]e$), i.e., you must find for each element "e" the matrix $[K]_e$ and the vector $[f]_e$ such that, $[K]^e \cdot [\varphi]^e = [f]^e$. There are different ways of getting the matrix $[K]^e$, as we will see later.

4. Assembling the equations for different elements: one has to assemble the equations for all elements. So, if we have a total of M effective nodes in the system, then we must build up a global matrix [K] of size $M \times M$ and a global vector $[f]$ of size M such that the FEM problems "reduces" to solve the following matrix equation: $[K] \cdot [\varphi] = [f]$ where $[\varphi] = [\varphi_1, \varphi_2, \ldots, \varphi_M]$ is the value of the approximate solution φ at the position where the effective nodes are. Notice that once we know $[\varphi_1, \varphi_2, \ldots, \varphi_M]$ then we can calculate the value of φ at whatever point x of the system.

5. Solve the system of equations: In principle you can use whatever method you want, but the more the number of nodes we use, the better is the quality of the solution and in consequence the matrices that we will build up can be very large, i.e. M becomes very large.

6. Compute secondary quantities: Once you know the φ values, you can compute other magnitudes using the values of φ.

3. Results

For the calibration procedure we have modeled typical silicon cantilevers used in conventional contact mode Atomic Force Microscopy. Young's modulus, Poisson's ratio and density of the probes are $E = 130\,\mathrm{GPa}$, $\nu = 0.279$ and $\rho = 2330\,\mathrm{kg \cdot m^{-3}}$, respectively [20, 21]. We have build Finite Element Models using the commercial ANSYS® Workbench™, Academic Research, Release 12.1 software. We have analyzed various geometries including simple tipless rectangular cantilevers that can be directly compared to the results from equation (9) as well as trapezoidal tipless levers, compared to the results from equation (10). Additionally, we created levers with a 3D trapezoidal cross-section with and without a pyramidal tip at its free end.

The rectangle AFM probes were modelled by a minimum of 550 3D tetrahedral elements and 1300 nodes and the levers with the trapezoidal cross-section with a maximum number of 36415 3D tetrahedral elements and 64582 nodes. In the cantilever-tip contact, where a higher strain is expected, the density of the grid elements was increased, as shown in Fig. 1, where the mesh model of a tipped lever

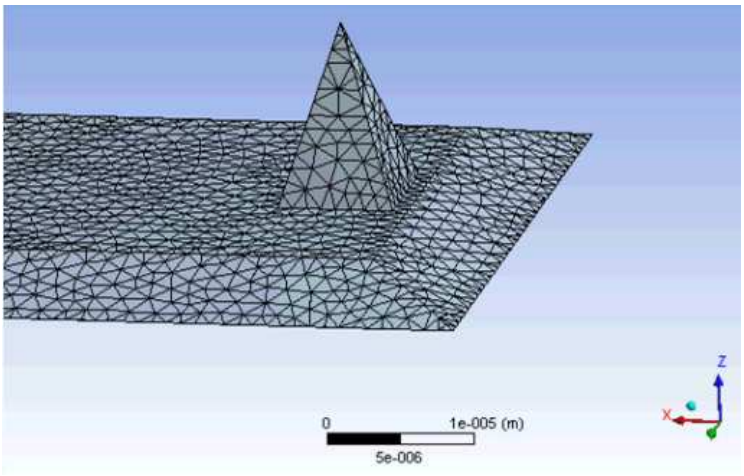

Fig. 1: The mesh model of a trapezoidal lever with a pyramidal tip at its free end.

is demonstrated. After creating proper mesh models, the stiffness was calculated by applying a vertical load at the free end of the beam and calculating the resulting deflection in the normal direction. We should note here that when we increased the number of 3D elements, the change in cantilever stiffness was negligible. The FEM results of cantilever deflection under loading are presented in the following Fig. 2.

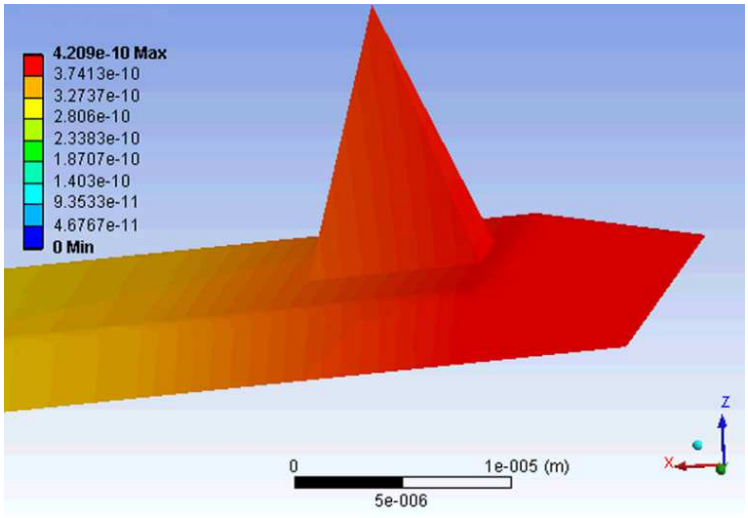

Fig. 2: The resulted deflection demonstrated in color code.

Tab. 1: Validation of our FE models.

cantilever number	Poggi et al Rect W1	FEM calc Rect W1	Ratio FEM per Poggi		Poggi et al Trap 2D	FEM calc Trap 2D	Ratio FEM per Poggi
1	3.660	3.741	1.022		2.820	2.866	1.016
2	3.240	3.292	1.016		2.420	2.450	1.012
3	2.380	2.432	1.022		2.010	2.052	1.021
4	4.450	4.531	1.018		3.380	3.428	1.014
5	2.580	2.629	1.019		2.020	2.051	1.015
6	2.280	2.325	1.020		1.790	1.817	1.015
7	6.370	6.499	1.020		4.830	4.901	1.015
8	2.770	2.835	1.023		2.290	2.334	1.019
9	5.480	5.590	1.020		2.170	4.233	1.015
10	4.790	4.879	1.019		3.580	3.629	1.014

Initially, we made an attempt to validate our rectangular and trapezoidal FE models with the results provided by Poggi *et al.* [16], for the rectangular and trapezoidal 2D geometry respectively. For this purpose, we have used the dimensional data of specific levers, measured by Poggi *et al.*, we constructed our models and then performed the virtual load-deflection experiments. For each case the cantilever elastic stiffness k_z is given by the ratio of applied force to resulting deflection. Our results are summarized in Table 1 where we observe an excellent agreement between our models and the experimental data. The ratio of computational to experimental value for each cantilever is practically 1. Fig. 3 shows the FE results for the calculated spring constant compared to literature.

After validating our models we proceed to compare the FE results with those provided by equations (9) and (10), for rectangular and trapezoidal cross sections respectively. Table 2 summarizes our results for all the geometries that we have used in this work. We observe that in the rectangular shaped case there exists an approximate 1.8–2.3% relative difference from theory whereas in the trapezoidal case this difference varies from 1.5–2%. When changing from the trapezoidal 2D to the more complex trapezoidal 3D geometry we observe a systematic overestimation of the cantilever stiffness that may be due to the model complexity. When examining the tipped cantilever in comparison to the tipless case the stiffness is slightly decreased. Fig. 4 demonstrates that when we assume a rectangular geometry with an average width there exists a significant overestimation of the cantilever stiffness whereas the trapezoidal cross section gives lower values for the spring constant. Additionally, in most cases there was no significant change in stiffness when moving to more complex FE models.

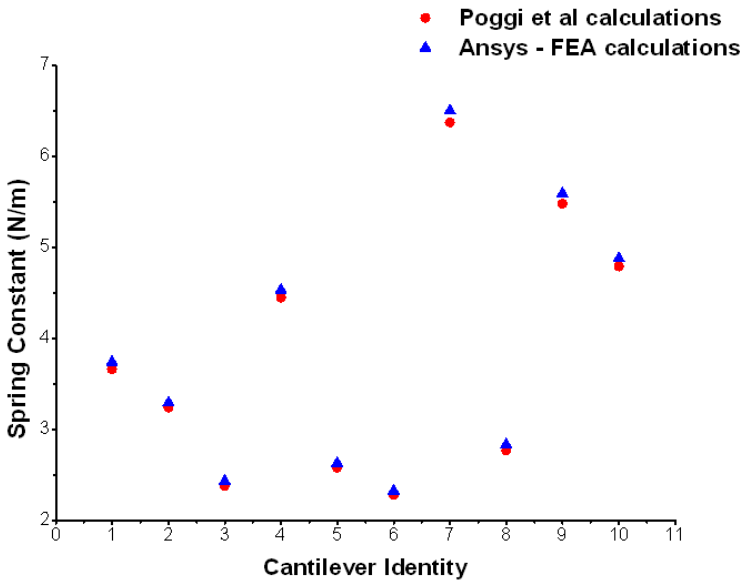

Fig. 3: The resulted deflection demonstrated in color code.

Tab. 2: FEM results and comparison with beam theory.

	K values (N/m)							
cantilever	rectangle			trapezoidal 2D			trapezoidal 3D	with tip
number	an/cal calcs	FEM calcs	relative dev.	an/cal calcs	FEM calcs	relative dev.	FEM calcs	FEM calcs
1	3.669	3.741	1.96%	2.822	2.866	1.55%	2.937	2.919
2	3.231	3.292	1.88%	2.415	2.450	1.45%	2.506	2.491
3	2.378	2.432	2.28%	2.012	2.052	2.01%	2.093	2.079
4	4.448	4.531	1.87%	3.378	3.428	1.46%	3.497	3.499
5	2.576	2.629	2.06%	2.017	2.051	1.68%	2.101	2.089
6	2.278	2.325	2.04%	1.789	1.817	1.56%	1.860	1.848
7	6.378	6.499	1.91%	4.828	4.901	1.52%	5.035	5.009
8	2.772	2.835	2.26%	2.289	2.334	1.97%	2.381	2.376
9	5.479	5.590	2.03%	4.166	4.233	1.60%	4.342	4.329
10	4.787	4.879	1.93%	3.575	3.629	1.53%	3.721	3.713

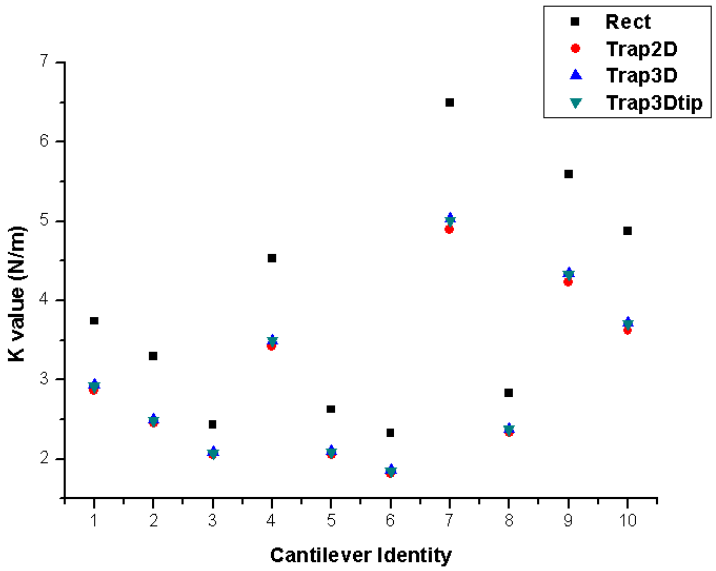

Fig. 4: Comparison of k_z values for several geometries.

4. Conclusions

The main purpose of this work is the presentation and comparative study of two very popular methods that we encounter in the calibration of contact Atomic Force cantilevers, the dimensional method from beam theory and Finite Element Modeling. Our rectangular and trapezoidal models were validated from experimental data and an excellent agreement was found, with the ratio of $k_{\mathrm{FEM}}/k_{\mathrm{exper}}$ approaching practically 1. The significance of the real trapezoidal geometry was also demonstrated as the plane rectangular approximation overestimates the cantilever spring constant in all studied levers. The trapezoidal 3D with/without tip geometries changed the calculated stiffness to a maximum of 3%, which is in the range of the estimated combined stiffness uncertainty provided by such a dimensional calibration method.

Acknowledgment

This research has been co-financed by the European Union (European Social Fund – ESF) and Greek national funds through the Operational Program "Education and Lifelong Learning" of the National Strategic Reference Framework (NSRF) – Research Funding Program: Heracleitus II. Investing in knowledge society through the European Social Fund.

We would also like to acknowledge the Lifelong Learning Programme (LLP)/Erasmus for mobility between Physics Department, Aristotle University of Thessaloniki, Thessaloniki Greece and Institute of Mathematics, Polish Academy of Sciences, Łódź Poland.

References

[1] V. L. Mironov, *Fundamentals of Scanning Probe Microscopy*, Nizhniy Novgorod 2004.

[2] A. Yacoot and L. Koenders, *Recent developments in dimensional nanometrology using AFMs*, Meas. Sci. Technol. **22** (2011), 1–12.

[3] N. A. Burnham et al., *Comparison of calibration methods for atomic-force microscopy cantilevers*, Nanotechnology **14** (2003), 1–6.

[4] C. A. Clifford and M. P. Seah, *The determination of atomic force microscope cantilever spring constants via dimensional methods for nanomechanical analysis*, Nanotechnology **16** (2005), 1666–1680.

[5] J. L. Choi and D. T. Gethin, *Simulation of atomic force microscopy operation via three-dimensional finite element modelling*, Nanotechnology **20** (2009), 1–14.

[6] D. A. Mendels et al., *Dynamic properties of AFM cantilevers and the calibration of their spring constants*, J. Micromech. Microeng. **16** (2006), 1720–1733.

[7] J. Ruan and B. Bhushan, *Atomic-scale friction measurements using friction force microscopy: Part I-General principles and new measurement techniques*, ASME J. Tribol. **116** (1994a), 378–388.

[8] A. Torii, M. Sasaki, K. Hane, and S. Okuma, *A method for determining the spring constant of cantilevers for atomic force microscopy*, Meas. Sci. Technol. **7** (1996), 179–184.

[9] M. L. Palacio and B. Bhushan, *Normal and lateral force calibration techniques for AFM cantilevers*, Critical Reviews in Solid State and Materials Sciences **35** (2010), 73–104.

[10] J. M. Neumeister and W. A. Ducker, *Lateral, normal, and longitudinal spring constants of atomic force microscopy cantilevers*, Rev. Sci. Instrum. **65**, (8) (1994), 2527–2531.

[11] J. P. Cleveland and S. Manne, *A nondestructive method for determining the spring constant of cantilevers for scanning force microscopy*, Rev. Sci. Instrum. **64** (1993), 403–405.

[12] J. E. Sader, *Calibration of rectangular atomic force microscope cantilevers*, Rev. Sci. Instrum. **70** (1999), 3967–3969.

[13] J. L. Hutter and J. Bechhoefer, *Calibration of atomic-force microscope tips*, Rev. Sci. Instrum. **64** (1993), 1868–1873.

[14] S. M. Cook et al., *Practical implementation of dynamic methods for measuring atomic force microscope cantilever spring constants*, Nanotechnology **17** (2006), 2135–2145.

[15] A. T. Beck and C. R. A. da Silva Jr, *Timoshenko versus Euler beam theory: Pitfalls of a deterministic approach*, Structural Safety **33** (2011), 19–25.

[16] M. A. Poggi, A. W. McFarland, J. S. Colton, and L. A. Bottomley, *A method for calculating the spring constant of atomic force microscopy cantilevers with a nonrectangular cross section*, Anal. Chem. **77** (2005), 1192–1195.

[17] E. J. Boyd and D. Uttamchandani, *Measurement of the anisotropy of Young's modulus in single-crystal silicon*, Journal of Micromechanical Systems **21** (2012), 1057–7157.

[18] J. N. Reddy, *An Introduction to The Finite Element Method* (Third Edition), McGraw-Hill, New York 2005.

[19] E. Madenci and I. Guven, *The Finite Element Method and Applications in Engineering Using ANSYS®*, Springer 2006.

[20] W. A. Brantley, *Calculated elastic constants for stress problems associated with semiconductor devices*, J. Appl. Phys. **44** (1973).

[21] Bo-Yi Chen, Meng-Kao Yeh, and Nyan-Hwa Tai, *Accuracy of the spring constant of atomic force microscopy cantilevers by finite element method*, Anal. Chem. **79** (2007), 1333–1338.

Physics Department
Solid State Physics Section
Aristotle University of Thessaloniki
Gr-54124 Thessaloniki
Greece
e-mail: hariton@physics.auth.gr; hariton@auth.gr

Presented by Ilona Zasada at the Session of the Mathematical-Physical Commission of the Łódź Society of Sciences and Arts on November 29, 2012

KALIBRACJA BELKI WSPORNIKOWEJ MIKROSKOPU SIŁ ATOMOWYCH Z WYKORZYSTANIEM METODY FEM

S t r e s z c z e n i e

W niniejszej pracy porównujemy dwie metody kalibracji belki wspornikowej mikroskopu sił atomowych, używanej w modzie kontaktowym; mianowicie metodą wymiarową i metodą elementu skończonego (FEM). Każda z metod została zastosowana do wyznaczenia/pokazania współczynnika sztywności belki wspornikowej k_z, będącego kluczowym parametrem rejestrowanych obrazów AFM ze stałą siłą. Metoda wymiarowa została ograniczona do przypadku prostokątnej i trapezoidalnej belki wspornikowej bez igły pomiarowej, podczas gdy metoda FEM pozwoliła na porównanie różnych geometrii belki wspornikowej, prostokątnej bez igły, dwu-wymiarowej trapezoidalnej bez igły, trój-wymiarowej trapezidalnej bez igły oraz trój-wymiarowej trapezoidalnej z igłą w kształcie piramidy. Modele użyte w metodzie FEM były zaprojektowane zgodnie z równaniem teorii belek oraz z danymi literaturowymi.

PL ISSN 0459-6854

B U L L E T I N

DE LA SOCIÉTÉ DES SCIENCES ET DES LETTRES DE ŁÓDŹ

2013 Vol. LXIII

Recherches sur les déformations no. 2

pp. 79–95

Julian Ławrynowicz, Kiyoharu Nôno, Daiki Nagayama, and Osamu Suzuki

A METHOD OF NONCOMMUTATIVE GALOIS THEORY FOR CONSTRUCTION OF QUARK MODELS (KOBAYASHI-MASUKAWA MODEL) II

EXCLUSION PRINCIPLES, QUARK MODELS, AND COLOURS

Summary

Concepts of binary and ternary Galois extension are introduced and the gauge theory with the symmetry group of the Galois groups is developed. Concepts of binary and ternary Clifford algebras are developed and the corresponding Dirac operators and Klein-Gordon operators are associated. In the present part of the paper, by use of the Galois extension structure of su(3), the quark models of Gell-Mann model are constructed. By use of the binary extension of su(3), the Kobayashi-Masukawa model is constructed.

Keywords and phrases: noncommutative Galois extension, ternary Clifford algebra, tenary Clifford analysis, quark model

Introduction

In the second part of the paper (Part I has been published in the preceding issue **63**, no. 1 of this journal, pp. 95–112), we observe the duality structure between binary and ternary quarks of su(3) (Theorem 3). By this we can give an understanding on the fact that mesons constitute with a quark an anti-quark and that baryons constitute only three quarks or anti-quarks (Theorem 4). Restricting the Galois invariant elements (Theorem 5), we can obtain the Gell-Mann model [4]. Next we proceed to the Kobayashi-Masukawa model. For this, we consider a binary Galois extension of su(3):

$$R\left[\sqrt[2]{-1},\ \sqrt[2]{-1},\ \sqrt[3]{1},\ \sqrt[2]{-1}\right]$$

and obtain 6 kinds of quarks. Then we can obtain the Kobayashi-Masukawa model. We can obtain three generations of 6 quarks (Theorem 6). We notice that a further ternary Galois extension can describe the kinds of colours of quarks. hence we can see that the method of noncommutative Galois theory has possibilities to describe the physics of quarks.

We recall the main results of the first part of the paper (Theorems 1 and 2) and state the results of the second part (Theorems 3 and 4):

(0) We formulate the physics of quark theory as the invariant spaces with respect to the Galois group.

(1) The binary and ternary Clifford algebras are introduced and the Dirac-type operators are associated. We can find a successive extension of binary and ternary extension on su(3) satisfying the required properties (Theorem 1).

(2) For a binary Clifford algebra there exists a sequence of noncommutative binary Galois extensions of the real field $\mathbb{R}$ which realize the given Clifford algebra (Theorem 2).

(3) For the case of a successive extension of binary and ternary extensions, we can find a duality structure between binary and ternary Galois extensions. By this we can show the structure of mesons and baryons (Theorem 3).

(4) By the following sequences of extensions, we can derive the so-called Gell-Mann model and Kobayashi-Masukawa model in a unified manner (Theorem 4)

$$\begin{aligned}\mathbb{R} &\Rightarrow R[\sqrt{1}] \Rightarrow R\left[\sqrt[2]{-1},\ \sqrt[2]{-1}\right] \Rightarrow R\left[\sqrt[2]{-1},\ \sqrt[2]{-1},\ \sqrt[3]{1}\right] \\ &\Rightarrow R\left[\sqrt[2]{-1},\ \sqrt[2]{-1},\ \sqrt[3]{1},\ \sqrt[2]{-1}\right] \Rightarrow R\left[\sqrt[2]{-1},\ \sqrt[2]{-1},\ \sqrt[3]{1},\ \sqrt[2]{-1},\ \sqrt[3]{1}\right].\end{aligned}$$

5. The binary and ternary Pauli exclusion principles

In this section, we introduce the concepts of binary and ternary Pauli exclusion principles for ternary elementary particles.

5.1. Binary and ternary Pauli exclusion principles

Prof. Kerner has generalized the well known Pauli condition to quarks which is called ternary Pauli exclusion principle [5]. We make the following definitions:

Definition 9. Let A be an algebra which is generated by θ^A $(A = 1, 2, \ldots, M)$ and $\bar{\theta}^A$ $(A = 1, 2, \ldots, M)$. Then we make the following concept [5, 6]:

1) $\theta^A\bar{\theta}^B$ $(A \neq B)$ is called to satisfy the *binary Pauli exclusion condition*, when

$$\theta^A\bar{\theta}^B = -\bar{\theta}^B\theta^A. \tag{55}$$

2) $\theta^A\theta^B\theta^C$ is called to satisfy the $\mathbf{j}$-*conjugate* (resp $\mathbf{j}^2$-*conjugate*) *Pauli exclusion condition*, when

$$\theta^A\theta^B\theta^C = \mathbf{j}\theta^B\theta^C\theta^A = \mathbf{j}^2\theta^C\theta^A\theta^B$$

(56)

$$\text{resp.} \quad (\theta^A\theta^B\theta^C = \mathbf{j}^2\theta^B\theta^C\theta^A = \mathbf{j}\theta^C\theta^A\theta^B).$$

Under the condition (2), we call the ternary Pauli condition with (resp. without) *colour condition*, when $\theta^A\theta^A\theta^A = 1$ (resp. $= 0$). We choose an algebra and can define binary particles and ternary particles making compositions of two generators and three generators. By this we can define the confined particles by the Pauli conditions. In fact, Kerner has proved that only one quark cannot exist, namely single quark is confined and that four quarks cannot exist [6]. Then we can prove the following theorem:

Theorem 3. 1) *Let A be an algebra which is generated by $\theta^A(A = 1, 2, \ldots, M)$ and $\bar{\theta}^A(A = 1, 2, \ldots, M)$ satisfying the binary Pauli exclusion principle. Then for the basic elements:*

$$\begin{cases} D_0'(\theta_1, \theta_2, \ldots, \theta_m) = e_1\theta_1 + \theta_2 e_2 + \ldots + \theta_m e_m, \\ \\ D_0''(\theta_1, \theta_2, \ldots, \theta_m) = \theta_1\bar{e}_1' + \theta_2\bar{e}_2' + \ldots + \theta_m\bar{e}_m', \end{cases} \tag{57}$$

we have an invariant element:

$$D_0'D_0''(\theta_1, \theta_2, \ldots, \theta_m) = \sum_{j=1}^{m} \theta_i\bar{\theta}_i \otimes 1. \tag{58}$$

2) *Let A be an algebra which is generated by $\bar{\theta}^A$ $(A = 1, 2, \ldots, M)$ and $\bar{\theta}^A$ $(A = 1, 2, \ldots, M)$ satisfying the ternary Pauli exclusion principle. Then for the basic element*

$$\begin{cases} D_0'(\theta_1, \theta_2, \theta_3) = e_1\theta_1 + \theta_2 e_2 + \theta_3 e_3, \\ \\ D_0''(\theta_1, \theta_2, \theta_3) = \theta_1 e_1' + j^2\theta_2 e_2' + j\theta_3 e_3', \\ \\ D_0''(\theta_1, \theta_2, \theta_3) = \theta_1 e_1' + j\theta_2 e_2' + j^2\theta_3 e_3', \end{cases} \tag{59}$$

we have an invariant element, when it satisfies the colour condition:

$$D_0'D_0''D_0'''(\theta_1, \theta_2, \theta_3) = (\theta_1^3 + \theta_2^3 + \theta_3^3 - 3\theta_1\theta_2\theta_3) \otimes 1. \tag{60}$$

3) *The binary and ternary Dirac operators and Klein-Gordon operators are the quantizations of gauge invariant elements. Here we introduce the quantization by*

$$\theta_i \to \partial/\partial\theta_i \quad (i = 1, 2, 3). \tag{61}$$

5.2. Duality structure between binary and ternary Galois extensions

We know that mesons and baryons constitute quarks. Moreover, we know the facts that each meson constitutes a quark and an anti-quark and that each baryon constitutes only three quarks or anti-quarks. Still now we have no understanding on this fact. We can give an understanding on this fact by use of the duality structure of binary and ternary Galois extensions. Here we propose a model of generations of particles in terms of Galois extensions. We assume that quarks and anti-quarks are generated by binary extensions. Hence we can see that the binary extensions generate mesons. After the generation of mesons, we have ternary Galois extension and baryons are created. From the duality structure between these extensions as we have seen in the case of su(3) (see Fig. 3 in Part. I), we can see that baryons constitute only particles or anti-particles.

Theorem 4. *Let A be an algebra which is generated by $\bar{\theta}^A$ $(A = 1, 2, \ldots, M)$ and $\bar{\theta}^A$ $(A = 1, 2, \ldots, M)$ satisfying the ternary Pauli exclusion principle. Moreover, it has a successive extension structure: $R[\sqrt[2]{-1}, \sqrt[3]{1}]$. Then for the basic elements of* (1) *and* (2) (in Part I) *we have the duality structure determined in* (4) *and shown in Fig.* 4.

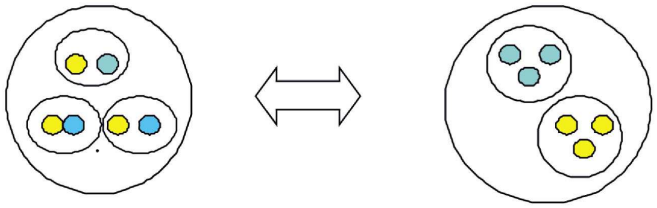

Fig. 4: The duality for the basic elements of (1) and (2).

6. The quark model of the Gell-Mann theory

In this section we discuss the quark model due to Gell-Mann by the structure of the Galois extension for su(3), see [4].

6.1. Binary Dirac operators

As we have seen, we can obtain the following commutation relations:

$$(62) \qquad \begin{cases} e_1^2 = e_2^2 = e_3^2 = -1, \\ \\ e_1 e_2 = -e_2 e_1 = e_3,\ e_2 e_3 = -e_3 e_2 = e_1,\ e_3 e_1 = -e_1 e_3 = e_2. \end{cases}$$

After the extension by e_0 $(= \mathrm{diag}\,[1, 1, 0])$, we have the Clifford algebra which is isomorphic to quaternion algebra. For e_i' and $e_i''(i = 1, 2, 3)$ we have the same asser-

tions. Making the quantization in Theorem 3, we can introduce the following binary Dirac operators for $\{e_0, e_1, e_2, e_3\}$:

$$\begin{cases} D = e_0\dfrac{\partial}{\partial x_0} + e_1\dfrac{\partial}{\partial x_1} + e_2\dfrac{\partial}{\partial x_1} + e_3\dfrac{\partial}{\partial x_3}, \\ \bar{D} = \bar{e}_0\dfrac{\partial}{\partial x_0} + \bar{e}_1\dfrac{\partial}{\partial x_1} + \bar{e}_2\dfrac{\partial}{\partial x_1} + \bar{e}_3\dfrac{\partial}{\partial x_3}. \end{cases} \tag{63}$$

We can obtain the Dirac operators for $\{e_0', e_1', e_2', e_3'\}$ and $\{e_0'', e_1'', e_2'', e_3''\}$ in a similar manner. Hence we can introduce three kinds of particles with spin $1/2$. Taking the fact that a quark can be regarded as a particle with spin $1/2$, we may introduce three kinds of quarks.

6.2. Ternary Dirac operators

From the results in Theorem 1, we have the ternary Galois extension structure for $\{e_1, e_1', e_1''\}$, $\{e_2, e_2', e_2''\}$, $\{e_3, e_3', e_3''\}$, see (51) in Part I. Hence we can also introduce ternary Dirac operators for:

$$\begin{cases} D = e_i\dfrac{\partial}{\partial\theta_1} + e_i'\dfrac{\partial}{\partial\theta_2} + e_i''\dfrac{\partial}{\partial\theta_3}, \\ D^* = e_i\dfrac{\partial}{\partial\theta_1} + \mathbf{j}^2 e_i'\dfrac{\partial}{\partial\theta_2} + \mathbf{j}e_i''\dfrac{\partial}{\partial\theta_3}, \quad (i = 1, 2, 3) \\ D^{**} = e_i\dfrac{\partial}{\partial\theta_1} + \mathbf{j}e_i'\dfrac{\partial}{\partial\theta_2} + \mathbf{j}^2 e_i''\dfrac{\partial}{\partial\theta_3}. \end{cases} \tag{64}$$

6.3. The duality structure between binary particles and ternary particles

From the noncommutative Galois structure on su(3), we have the duality structure on su(3). We can prove

Theorem 5. *We have the following "duality structure" between binary and ternary Galois extensions and the Dirac operators shown in Fig.* 5.

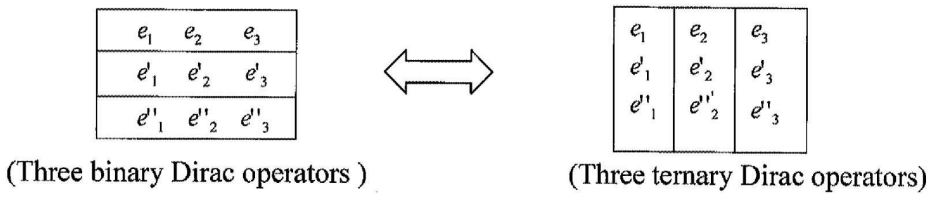

Fig. 5: Duality between the collections of binary and ternary Dirac-like operators.

Remark. We make a comment on the possibility of discussions on the quark confinement by the duality. We understand the duality as follows: The real world can be described by binary particles. The gauge theory of ternary extensions describes the fictitious space. It does not control the real world directly, but through the duality structure. The selection rule of particles can be described by the duality theorem. Then we can obtain real particles if and only if the quarks constitute with 3n quarks. Hence we can see that we have no single quark, or four quarks. This should be discussed carefully.

6.4. The construction of quark models

We proceed to the construction of quark models. We show that we can realize the Gell-Mann model making the gauge theory by the Galois extension structure on su(3). At first we notice that we can introduce three kinds of quarks by the binary Galois extension on su(3). We may identify the quarks as up-quark, down-quark, strange quark respectively; cf. [11]:

$$\{e_0, e_1, e_2, e_3\} \Rightarrow u, \quad \{e'_0, e'_1, e'_2, e'_3\} \Rightarrow d, \quad \{e''_0, e''_1, e''_2, e''_3\} \Rightarrow s. \tag{65}$$

(i) We begin with the construction of Gell-Mann model for mesons by use of binary Galois extensions. We consider the algebra A_0 which is generated by three elements u, d, s. We introduce the conjugate operation by $u, d, s \to \bar{u}, \bar{d}, \bar{s}$ making the conjugate elements of (65):

$$\{\bar{e}_0, \bar{e}_1, \bar{e}_2, \bar{e}_3\} \Rightarrow \bar{u}, \quad \{\bar{e}'_0, \bar{e}'_1, \bar{e}'_2, \bar{e}'_3\} \Rightarrow \bar{d}, \quad \{\bar{e}''_0, \bar{e}''_1, \bar{e}''_2, \bar{e}''_3\} \Rightarrow \bar{s}. \tag{66}$$

We can realize mesons by use of the binary Galois extension. Choosing an element $(\theta_1 u + \theta_2 d + \theta_3 s)$ and its conjugate operator $(\bar{\theta}_1 \bar{u} + \bar{\theta}_2 \bar{d} + \bar{\theta}_3 \bar{s})$, and making the invariant element, we have

$$\begin{aligned} &(\theta_1 u + \theta_2 d + \theta_3 s)(\theta_1 \bar{u} + \theta_2 \bar{d} + \theta_3 \bar{s}) \\ &= (\theta_1, \theta_2, \theta_3) \begin{pmatrix} u\bar{u} & u\bar{d} & u\bar{s} \\ d\bar{u} & d\bar{d} & d\bar{s} \\ s\bar{d} & s\bar{d} & s\bar{s} \end{pmatrix} \begin{pmatrix} \bar{\theta}_1 \\ \bar{\theta}_2 \\ \bar{\theta}_3 \end{pmatrix} \quad (= {}^t\theta\Theta\bar{\theta}). \end{aligned} \tag{67}$$

Then decomposing the matrix into the symmetric and skew symmetric matrix we can obtain a similar realization due to Gell-Mann model:

$$\begin{aligned} \Theta \;=\; &\begin{pmatrix} u\bar{u} & 0 & 0 \\ 0 & d\bar{d} & 0 \\ 0 & 0 & s\bar{s} \end{pmatrix} + \frac{1}{2} \begin{pmatrix} 0 & u\bar{d} + d\bar{u} & u\bar{s} + s\bar{u} \\ u\bar{d} + d\bar{u} & 0 & d\bar{s} + s\bar{d} \\ s\bar{u} + u\bar{s} & s\bar{d} + d\bar{s} & 0 \end{pmatrix} \\ &+ \frac{1}{2} \begin{pmatrix} 0 & u\bar{d} - d\bar{u} & u\bar{s} - s\bar{u} \\ d\bar{u} - u\bar{d} & 0 & d\bar{s} - s\bar{d} \\ s\bar{u} - u\bar{s} & s\bar{d} - d\bar{s} & 0 \end{pmatrix}. \end{aligned} \tag{68}$$

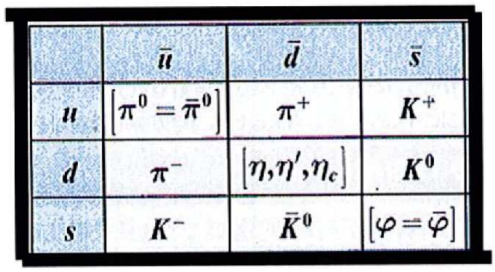

	$\bar{u}$	$\bar{d}$	$\bar{s}$
u	$\left[\pi^0 = \bar{\pi}^0\right]$	π^+	K^+
d	π^-	$\left[\eta, \eta', \eta_c\right]$	K^0
s	K^-	$\bar{K}^0$	$\left[\varphi = \bar{\varphi}\right]$

Fig. 6: The quark realization of mesons by use of the binary Galois extension on su(3).

(ii) Next we proceed to the realization of baryons. By use of the duality theorem, we can realize the ternary version of the quarks:

$$\{e_1, e_1', e_1''\} \Rightarrow u, \quad \{e_2, e_2', e_2''\} \Rightarrow d, \quad \{e_3, e_3', e_3''\} \Rightarrow s. \tag{69}$$

Then we take the ternary Galois extension structure by G (given by $(42)'$). By use of an algebra A_0, we make the following extension by G:

$$A_0[\sqrt[3]{1}] = \left\{\theta_1 1 + \theta_2 G + \theta_3 G^2 | \theta_1, \theta_2, \theta_3 \in A\right\}. \tag{70}$$

Then we can expect to realize the Gell-Mann model in this extension scheme. Choosing the following elements corresponding to the ternary Dirac operator, we may realize the baryons by the invariant elements (see Theorem 3, 2):

$$\begin{aligned}
&(\theta_1 u + \theta_2 d + \theta_3 s)\left(\theta_1 u + \theta_2 dG^2 + \theta_3 sG\right) j \left(\theta_1 u + \theta_2 dG + \theta_3 sG^2\right) \\
&= \left(uuu\theta_1^3 + ddd\theta_2^3 + sss\theta_3^3\right) \otimes 1 \\
&\quad + \left[(uud + udu + duu)\,\theta_1^2\theta_2 + (ddu + dud + udd)\,\theta_2\theta_1^2\right. \\
&\quad + (ssd + sds + dss)\theta_2\theta_3^2 + (dds + dsd + sdd)\theta_3^2\theta_2 \\
&\quad + (uus + usu + suu)\theta_1^2\theta_3 + (ssu + sus + uss)\,\theta_3\theta_1^2 \\
&\quad \left. + (usd + uds + dus + dsu + sud + uds)\,\theta_1\theta_2\theta_3\right] \otimes \hat{G},
\end{aligned} \tag{71}$$

where

$$\hat{G} = 1 + G + G^2 \quad (\neq 0).$$

Hence we can obtain 10 (resp 7) baryons from the symmetric elements when they satisfy the Pauli condition with (resp. without) colour condition (as for colours, see Sect. 8 below).

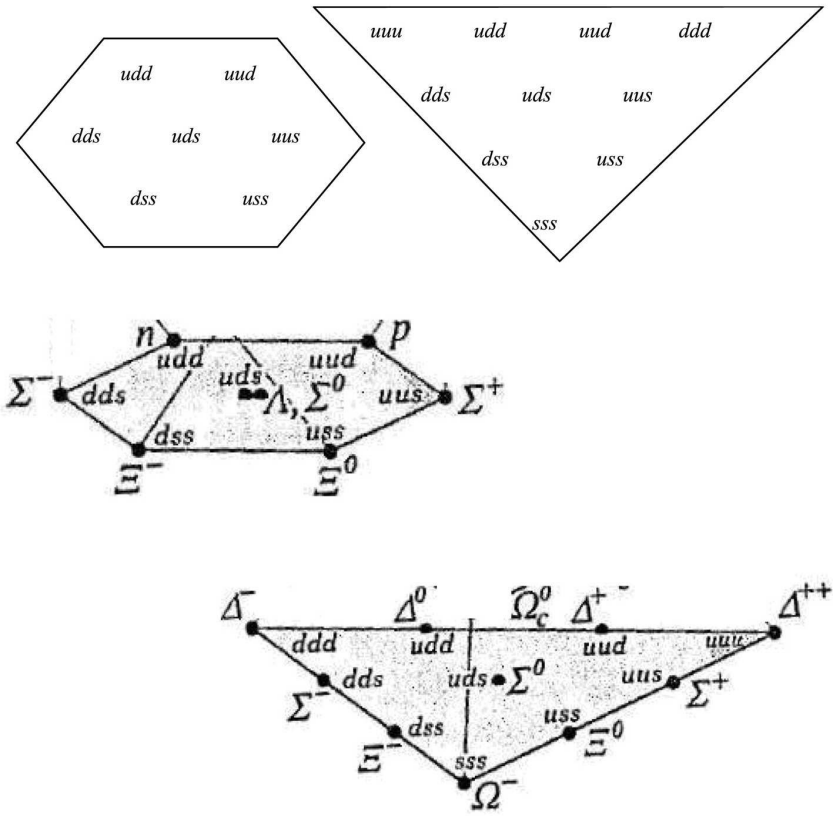

Fig. 7: The quark realization of baryons by use of the ternary Galois extension on su(3). The hexagon (resp. triangle) corresponds to the case of the Pauli condition without (resp. with) colour condition.

7. Quark model of the Kobayashi-Masukawa theory

We realize the Kobayashi-Masukawa model by use of the noncommutative Galois theory. We propose the Galois theory of Kobayashi-Masukawa model by making the binary extension of su(3) (see [8]):

$$\mathrm{su}(3)\left[\sqrt[3]{-1}\right].$$

By use of an algebra A_0 $(=\mathrm{su}(3))$, we make the following extension by G and H (given by (42′) and (40), respectively):

$$A_0\left[\sqrt[3]{1}\right]$$

(72)

$$=\left\{\theta_1 1+\theta_2 G+\theta_3 G^2+H(\theta_4 1+\theta_5 G+\theta_6 G^2)|\theta_i \quad (i=1,2,\ldots,6)\in A_0\right\}.$$

By this we determine possible mesons and baryons. We can prove the theorem:

Theorem 6. (1) *We can produce* 6 *kinds of quarks and we can find* 3 *generations of the quarks. Namely, we can obtain* 6 *kinds of quarks by use of the extension:*

$$\mathrm{su}(3)\left[\sqrt[2]{-1}\right].$$

(2) *Furthermore, if we make a ternary extension, we can introduce the concept of colours for the extension.*

7.1. The construction of quark models (mesons)

We can realize the Kobayashi-Masukawa model by use of the binary Galois extension structure on su(3). We prepare three kinds of quarks by the binary Galois extension on su(3) and their anti-quarks:

$$\{e_0, e_1, e_2, e_3\} \Rightarrow u, \quad \{e'_0, e'_1, e'_2, e'_3\} \Rightarrow c, \quad \{e''_0, e''_1, e''_2, e''_3\} \Rightarrow b, \tag{73}$$

$$\{\bar{e}_0, \bar{e}_1, \bar{e}_2, \bar{e}_3\} \Rightarrow \bar{u}, \quad \{\bar{e}'_0, \bar{e}'_1, \bar{e}'_2, \bar{e}'_3\} \Rightarrow \bar{c}, \quad \{\bar{e}''_0, \bar{e}''_1, \bar{e}''_2, \bar{e}''_3\} \Rightarrow \bar{b}. \tag{74}$$

Here we notice that the associations of quarks are different from those of the Gell-Mann model. Next we proceed to the construction of furthermore binary extensions. Then we can obtain three new quarks:

$$\{f_0, f_1, f_2, f_3\} \Rightarrow d, \quad \{f'_0, f'_1, f'_2, f'_3\} \Rightarrow s, \quad \{f''_0, f''_1, f''_2, f''_3\} \Rightarrow t, \tag{75}$$

$$\left\{\bar{f}_0, \bar{f}_1, \bar{f}_2, \bar{f}_3\right\} \Rightarrow \bar{d}, \quad \left\{\bar{f}'_0, \bar{f}'_1, \bar{f}'_2, \bar{f}'_3\right\} \Rightarrow \bar{b}, \quad \left\{\bar{f}''_0, \bar{f}''_1, \bar{f}''_2, \bar{f}''_3\right\} \Rightarrow \bar{t}. \tag{75}'$$

We can realize mesons by use of the binary Galois extension. Choosing an element

$$\Theta = \theta_1 u + \theta_2 d + \theta_3 s + \theta_4 c + \theta_5 b + \varepsilon\theta_6 t \tag{76}$$

and its conjugate operator

$$\overline{\Theta} = \bar{\theta}_1 \bar{u} + \bar{\theta}_2 \bar{d} + \bar{\theta}_3 \bar{s} + \bar{\theta}_4 \bar{c} + \bar{\theta}_5 \bar{b} + \bar{\varepsilon}\bar{\theta}_6 \bar{t} \tag{77}$$

and making the invariant element, we have ${}^t\Theta\Omega\overline{\Theta}$ with

$$\Omega = \begin{pmatrix} u\bar{u} & u\bar{d} & u\bar{s} & u\bar{c} & u\bar{b} & \varepsilon u\bar{t} \\ d\bar{u} & d\bar{d} & d\bar{s} & d\bar{c} & d\bar{b} & \varepsilon d\bar{t} \\ s\bar{u} & s\bar{d} & s\bar{s} & s\bar{c} & s\bar{b} & \varepsilon s\bar{t} \\ c\bar{u} & c\bar{d} & c\bar{s} & c\bar{c} & c\bar{b} & \varepsilon c\bar{t} \\ bu\bar{u} & b\bar{d} & b\bar{s} & b\bar{c} & b\bar{b} & \varepsilon d\bar{t} \\ \varepsilon t\bar{u} & \varepsilon t\bar{d} & \varepsilon t\bar{s} & \varepsilon t\bar{c} & \varepsilon t\bar{b} & \varepsilon^2 t\bar{t} \end{pmatrix}, \tag{78}$$

where ε implies that the survival time of the top quark is very small. In an analogous manner as in the Gell-Mann model, we can obtain mesons in a similar manner.

	$\bar{u}$	$\bar{d}$	$\bar{s}$	$\bar{c}$	$\bar{b}$	$\bar{t}$
u	$\pi^0=\bar{\pi}^0$	π^+	K^+	$\bar{D}^0$	B^+	
d	π^-	η,η',η_c	K^0	D^-	B^0	
s	K^-	$\bar{K}^0$	$\varphi=\bar{\varphi}$	D_S^-	B_S^0	
c	D^0	D^+	D_S^+	$J/\psi=\overline{J/\psi}$	B_C^+	
b	B^-	$\bar{B}^0$	$\bar{B}_S^0$	B_C^-	$\Upsilon=\bar{\Upsilon}$	
t						

Fig. 8: The quark realization of mesons by use of the binary Galois extension of su(3) within the Kobayashi-Masukawa model.

7.2. The construction of quark models (baryons)

Next we proceed to the realization of baryons. Then we can realize the baryons by the ternary Galois invariant elements (see [19]). We prepare the following proposition:

Proposition 10. For a system generated by $(\theta_1 u + \theta_2 d + \theta_3 s + \theta_4 c)$, we can generate four Clifford triples (see Definition 8):

$$[u,d,s], \quad [u,d,c], \quad [d,s,c], \quad [u,s,c]. \tag{79}$$

Hence we can generate baryons by the use of ternary Galois extensions.

Proof. We choose a triple $[u,d,s]$. Then we can make the ternary Galois extension and determine its invariant elements:

$$(\theta_1 u + \theta_2 d + \theta_3 s)(\theta_1 u + \theta_2 dG^2 + \theta_3 sG)(\theta_1 u + \theta_2 dG + \theta_3 sG^2). \tag{80}$$

In consequence we can obtain the generation of baryons in Figs. 9(a) and 10(a). Choosing other ternary Clifford triples, we can generate another system of baryons in a similar manner Fig. 9(b) and 10(b):

(a)

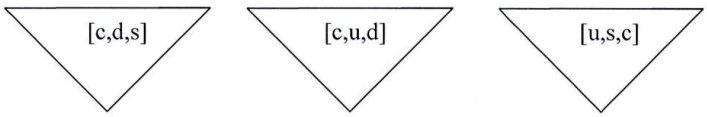

(b)

Fig. 9: The generations of baryons involved in their quark realization (a) without colour condition, (b) with colour condition.

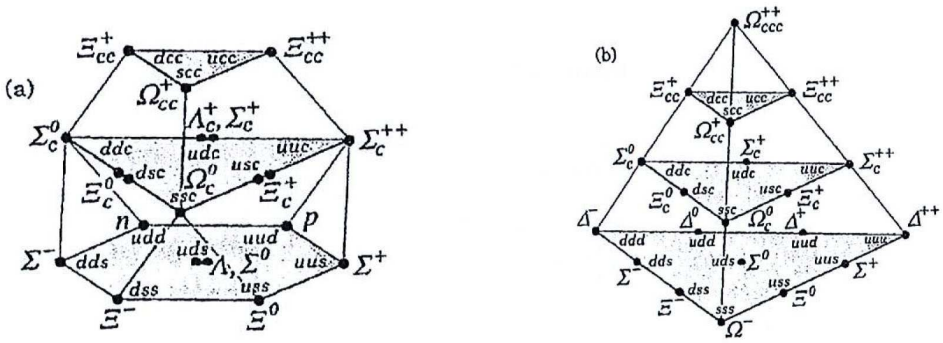

Fig. 10: The quark realization of baryons by use of the ternary Galois extension: (a) without colour condition, (b) with colour condition.

7.3. The 3-generations of quarks

Next we proceed to the "3-generation structure" in quarks. At first we notice the duality structures for the quarks.

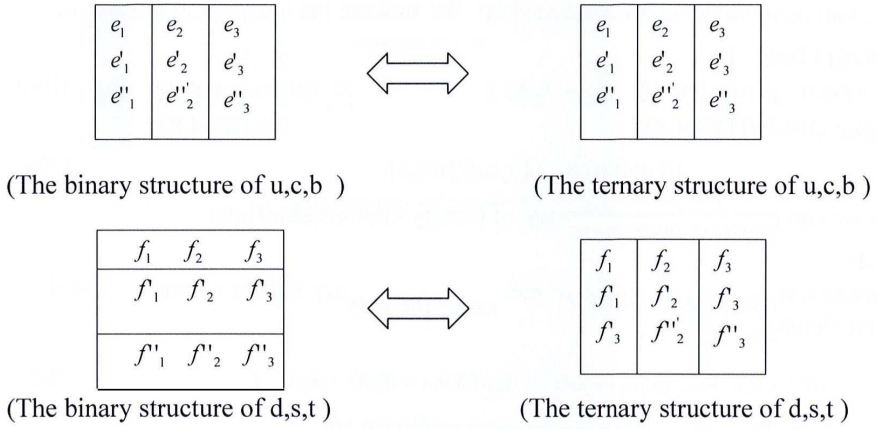

Fig. 11: Duality between the binary and ternary structures of the triple generations of baryons.

By use of the binary extension of these two structures, we see the duality structure between these duality structures can be obtained. By this fact we have the three generations (Fig. 12).

Hence we can obtain the generation structure:

$$\binom{u}{d}, \quad \binom{c}{s}, \quad \binom{t}{b}. \tag{81}$$

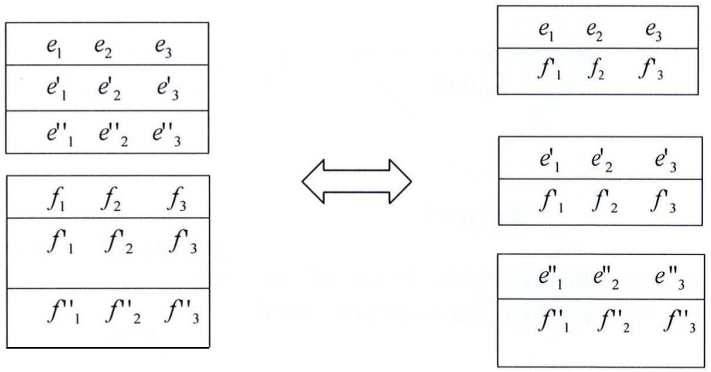

Fig. 12: Duality between the collection of two ternary structures of triple generations of baryons and the collection of three binary structures of triple generations of baryons.

which leads us to a cumulative scheme for elementary particles including quarks, leptons and bosons, and generations of Matter (Fig. 13) as well as corresponding 3-generations, more precisely: 3-objects, consisting of 2 collections of 2 particles, constructed from 2 *proper* generations, more precisely, from:

- 2 objects consisting of 3 collections of 2 particles (in each case),
- 2 objects consisting of 2 collections of 3 particles (in each case),
- 1 object consisting of 3 collections of 2 particles (in each case) and 1 object consisting of 2 collections of 3 particles (in each case).

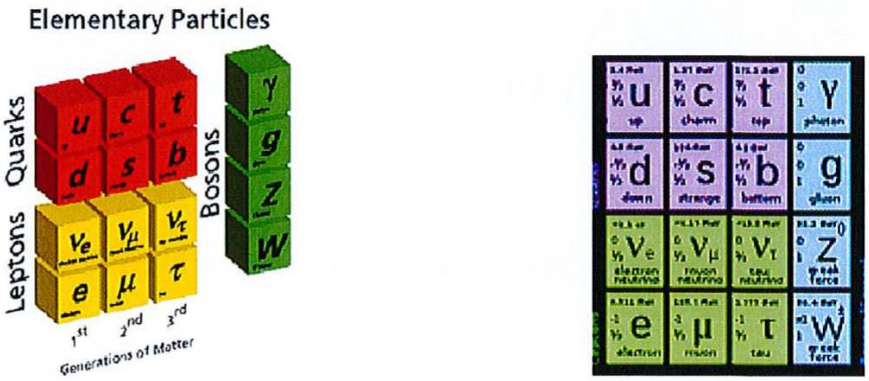

Fig. 13: A cumulative scheme for elementary particles including quarks, leptons and bosons, and generation of Matter.

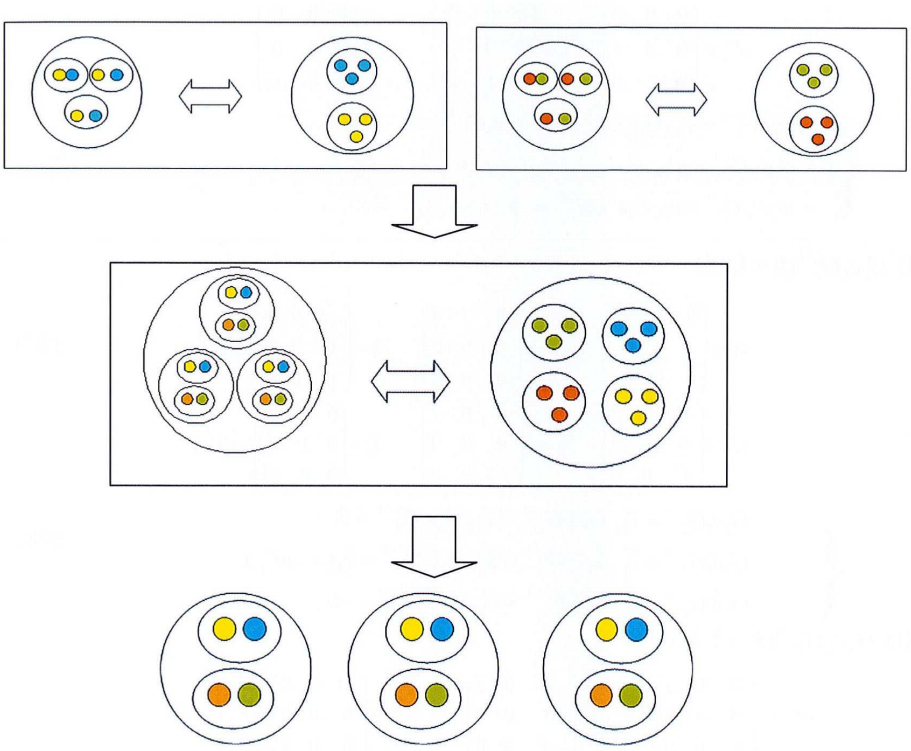

Fig. 14: An example of a corresponding 3-generation constructed from 2 proper generations (*proper* in the sense described above).

8. Introduction of colours

Here we describe a concept of colours in terms of noncommutative Galois extension. We propose a model of colours by use of the *nonion extension* of su(3):

$$G_i e_k G_i^{-1} = e_k'' \quad (i,k=1,2,3), \tag{82}$$

where

$$e_1 = \begin{pmatrix} 0 & i & 0 \\ i & 0 & 0 \\ 0 & 0 & 0 \end{pmatrix}, \quad e_2 = \begin{pmatrix} 0 & -1 & 0 \\ 1 & 0 & 0 \\ 0 & 0 & 0 \end{pmatrix}, \quad e_3 = \begin{pmatrix} i & 0 & 0 \\ 0 & -i & 0 \\ 0 & 0 & 0 \end{pmatrix},$$

(83)

$$G_1 = \begin{pmatrix} 0 & 1 & 0 \\ 0 & 0 & 1 \\ 1 & 0 & 0 \end{pmatrix}, \quad G_2 = \begin{pmatrix} 0 & j^2 1 & 0 \\ 0 & 0 & j \\ 1 & 0 & 0 \end{pmatrix}, \quad G_3 = \begin{pmatrix} 0 & j & 0 \\ 0 & 0 & j^2 \\ 1 & 0 & 0 \end{pmatrix}.$$

Hence we have the following basis:

I. $G_1 e_k G_1^{-1} \quad (k=1,2,3)$

$$e_1' = \begin{pmatrix} 0 & 0 & i \\ 0 & 0 & 0 \\ i & 0 & 0 \end{pmatrix}, \quad e_2' = \begin{pmatrix} 0 & 0 & 1 \\ 0 & 0 & 0 \\ -1 & 0 & 0 \end{pmatrix}, \quad e_3' = \begin{pmatrix} i & 0 & 0 \\ 0 & 0 & 0 \\ 0 & 0 & -i \end{pmatrix},$$

(84)

$$e_1'' = \begin{pmatrix} 0 & 0 & 0 \\ 0 & 0 & i \\ 0 & i & 0 \end{pmatrix}, \quad e_2'' = \begin{pmatrix} 0 & 0 & 0 \\ 0 & 0 & -1 \\ 0 & 1 & 0 \end{pmatrix}, \quad e_3'' = \begin{pmatrix} 0 & 0 & 0 \\ 0 & i & 0 \\ 0 & 0 & -i \end{pmatrix},$$

(85)
$$\begin{cases} G_1 e_1 G_1^{-1} = e_1', \quad G_1 e_2 G_1^{-1} = e_2', \quad G_1 e_3 G_1^{-1} = e_3', \\ G_1 e_1' G_1^{-1} = e_1'', \quad G_1 e_2' G_1^{-1} = e_2'', \quad G_1 e_3' G_1^{-1} = -e_3'', \\ G_1 e_1'' G_1^{-1} = e_1, \quad G_1 e_2'' G_1^{-1} = -e_2, \quad G_1 e_3'' G_1^{-1} = e_3''. \end{cases}$$

II. $G_2 e_k G_2^{-1} \quad (k=1,2,3)$

$$\tilde{e}_1 = \begin{pmatrix} 0 & i & 0 \\ i & 0 & 0 \\ 0 & 0 & 0 \end{pmatrix}, \quad \tilde{e}_2 = i \begin{pmatrix} 0 & j & 0 \\ j^2 & 0 & 0 \\ 0 & 0 & 0 \end{pmatrix}, \quad \tilde{e}_3 = \begin{pmatrix} -i & 0 & 0 \\ 0 & 0 & 0 \\ 0 & 0 & 1 \end{pmatrix} \quad (= e_3'),$$

(86)

$$\tilde{\tilde{e}}_1 = i \begin{pmatrix} 0 & 0 & j \\ 0 & 0 & 0 \\ j^2 & 0 & 0 \end{pmatrix}, \quad \tilde{\tilde{e}}_2 = i \begin{pmatrix} 0 & 0 & j \\ 0 & 0 & 0 \\ j^2 & 0 & 0 \end{pmatrix}, \quad \tilde{\tilde{e}}_3 = \begin{pmatrix} 0 & 0 & 0 \\ 0 & 1 & 0 \\ 0 & 0 & -1 \end{pmatrix} \quad (= ie_3''),$$

(87)
$$\begin{cases} G_2 e_1 G_2^{-1} = \tilde{e}_1, \quad G_2 e_2 G_2^{-1} = \tilde{e}_2, \quad G_2 e_3 G_2^{-1} = \tilde{e}_3, \\ G_2 \tilde{e}_1 G_2^{-1} = \tilde{\tilde{e}}_1, \quad G_2 \tilde{e}_2 G_2^{-1} = \tilde{\tilde{e}}_2, \quad G_2 \tilde{e}_3 G_2^{-1} = \tilde{\tilde{e}}_3 (= -ie_3''), \\ G_2 \tilde{\tilde{e}}_1 G_2^{-1} = e_1, \quad G_2 \tilde{\tilde{e}}_2 G_2^{-1} = e_2, \quad G_2 \tilde{\tilde{e}}_3 G_2^{-1} = ie. \end{cases}$$

III. $G_3 e_k G_3^{-1} (k=1,2,3)$

$$e_1^* = i \begin{pmatrix} 0 & 0 & j \\ 0 & 0 & 0 \\ j^2 & 0 & 0 \end{pmatrix}, \; e_2^* = i \begin{pmatrix} 0 & 0 & j \\ 0 & 0 & 0 \\ -j^2 & 0 & 0 \end{pmatrix}, \; e_3^* = \begin{pmatrix} -i & 0 & 0 \\ 0 & 0 & 0 \\ 0 & 0 & 1 \end{pmatrix} \quad (= e_3'),$$

(88)

$$e_1^{**} = i \begin{pmatrix} 0 & 0 & 0 \\ 0 & 0 & j \\ 0 & j^2 & 0 \end{pmatrix}, \; e_2^{**} = i \begin{pmatrix} 0 & 0 & 0 \\ 0 & 0 & -j \\ 0 & j^2 & 0 \end{pmatrix}, \; e_3^{**} = i \begin{pmatrix} 0 & 0 & 0 \\ 0 & 1 & 0 \\ 0 & 0 & -1 \end{pmatrix} \; (= ie_3),$$

$$(89)\qquad \begin{cases} G_3e_1G_3^{-1}=e_1^*, \quad G_3e_2G_3^{-1}=ee_2^*, \quad G_2e_3G_2^{-1}=e_3^*, \\ G_3e_1^*G_3^{-1}=e_1^{**}, \quad G_3e_2^*G_2^{-1}=e_2^{**}, \quad G_3e_3^*G_3^{-1}=e_3^{**}(=e_3), \\ G_3e_1^{**}G_3^{-1}=e_1, \quad G_3ee_2^{**}G_3^{-1}=e_2, \quad G_3e_3^{**}G_3^{-1}=e_2. \end{cases}$$

The rules (82) or (85), (87), (89) determining the transformations G_1, G_2, G_3 can be expressed in an elegant way as shown in Fig. 15.

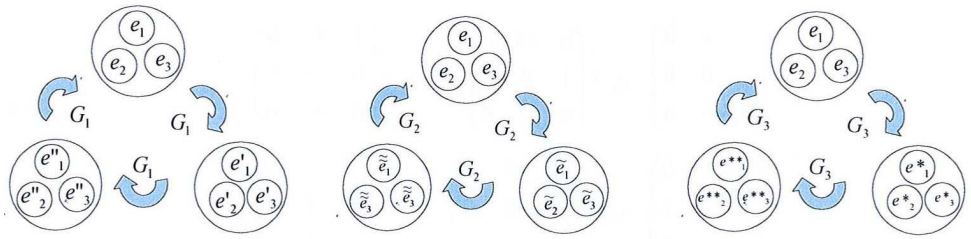

Fig. 15: Transformations G_1, G_2, G_3 governing the nonion extention of su(3).

We can obtain the Dirac operators for

$$\{e_0', e_1', e_2', e_3'\}, \quad \{e_0'', e_1'', e_2'', e_3''\}, \quad \{\tilde{e}_0, \tilde{e}_1, \tilde{e}_2, \tilde{e}_3\},$$
$$\{\tilde{\tilde{e}}_0, \tilde{\tilde{e}}_1, \tilde{\tilde{e}}_2, \tilde{\tilde{e}}_3\}, \quad \{e_0, e_1^*, e_2^*, e_3^*\}, \quad \{e_0, e_1^{**}, e_2^{**}, e_3^{**}\}$$

in a similar manner. By the nonion extension of su(3), we can introduce the colours. The idea of this is visualized in Fig. 16. We may also discuss more general quark models. This will be discussed in the next paper.

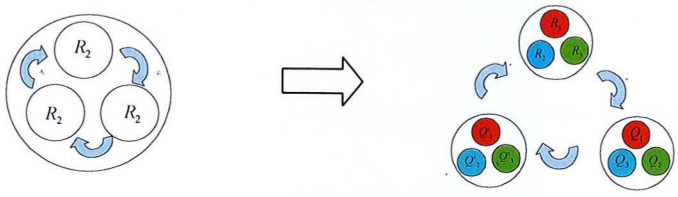

Fig. 16: The idea of introducing colours of elementary particles in connection with the transformations G_1, G_2, G_3 governing the nonion extension of su(3).

9. Conclusions and discussion

We have introduced a concept of noncommutative Galois extension for algebras and discussed its gauge theory. The physical observables are defined by gauge invariant objects. We have observed the Galois extension structure on su(3). The concept of ternary Clifford algebra is introduced and its characterization is given. With these preliminaries we consider the physics of quarks. By use of binary/ternary

Galois extension we have treated mesons/baryons, respectively. By use of the duality structure between binary and ternary Galois extensions, we can prove that baryons constitute with only quarks or anti-quarks and that mesons constitute with a quark and anti-quark.

Analyzing the Galois structure on su(3), we have shown the duality structure between mesons and baryons and realized the so called Gell-Mann model. Making the successive ternary extensions on su(3), we have constructed the Kobayashi-Masukawa model and derived 3-generations structure of the quark world. By use of the ternary Galois extension, we have introduced the concept of colours.

Hence we may conclude that in the future we can find a possibility of treatments on quarks by use of the noncommutative Galois theory.

References

[1] V. Abramov, R. Kerner, and B. Le Roy, *A $\mathbb{Z}$-graded generalization of supersymmetry*, J. Math. Phys. **38** (1997), 1650–1669.

[2] S. Eidelman et al., *Particle data group: Review of particle physics*, Phys. Lett. B **592**, nos. 1–4 (2004), 1–5.

[3] F. de Meyer and E. Ingram, *Separable Algebras over Commutative Rings*, (Springer Lecture Notes) in Math., Springer Verlag Berlin-Göttingen-Heidelberg 1971, 181 pp.

[4] M. Gell-Mann and Y. Néeman, *The Eight-fold Way*, W. A. Benjamin, New York-Amsterdam 1964.

[5] R. Kerner, *$\mathbb{Z}$-graded algebras and the cubic root of supersymmetry translations*, J. Math. Phys. **33** (1997), 403–411.

[6] R. Kerner, *The cubic chessboard*, Classical and Quantum Gravity **14** (1997), A203–A225.

[7] R. Kerner and O. Suzuki, *Internal symmetric groups of cubic algebra*, Internat. J. of Geom. Methods in Modern Phys. **8**, no. 7 (2011), 1487–1506.

[8] M. Kobayashi and T. Masukawa, *CP-violation in the renormalizable theory of weak interaction*, Prog. Th. Physics, **49**, no. 2 (1973), 652–657.

[9] J. Ławrynowicz, K. Nouno, D. Nagayama, and O. Suzuki, *Non-commutative Galois theory on Nonion algebra and* su(3) *and its application to constructions of quark models*, Soryuusironnkennkyuu, Yukawa Institute, Kyoto 2012, pp. 145–157.

[10] T. Nakayama and G. Azumaya, *Algebra (II)*, Iwanami Publisher, Tokyo 1954, (in Japanese).

[11] K. Huang, *Quarks, Leptons and Gauge Fields*, 2nd ed., World Scientific, Singapore 2013.

Department of Solid State Physics
University of Łódź
Pomorska 153/156, PL-90-236 Łódź
Institute of Mathematics
Polish Academy of Sciences
Śniadeckich 8, P.O. Box 21
PL-00-956 Warszawa, Poland
e-mail: jlawryno @uni.lodz.pl

Department of Mathematics
Fukuoka University of Education
Munakata-shi, Fukuoka
Japan
e-mail:nouno@fukuoka-edu.ac.jp

Department of Computer
and System Analysis
College of Humanities and Sciences
Nihon University, Sakurajosui 3-25-40
156-8550 Setagaya-ku, Tokyo
Japan
e-mail: osuzuki@chs.nihon-u.ac.jp

Presented by Julian Ławrynowicz at the Session of the Mathematical-Physical Commission of the Łódź Society of Sciences and Arts on November 29, 2012

METODA NIEPRZEMIENNEJ TEORII GALOIS DLA KONSTRUKCJI MODELI KWARKÓW (MODEL KOBAYASHIEGO-MASUKAWY) II

ZASADY WYKLUCZANIA, MODELE KWARKÓW I KOLORY

S t r e s z c z e n i e

Idea binarnego i ternarnego rozszerzenia Galois jest rozważana w kontekście teorii cechowania z grupą symetrii z grup Galois. Również pojęcia binarnej i ternarnej algebry Clifforda są rozważane i użyte do określenia stowarzyszonych operatorów Diraca i Kleina-Gordona. W obecnej części pracy, przez zastosowanie procedury rozszerzenia Galois algebry su(3), konstruujemy modele kwarkowe modelu Gell-Manna. Z kolei, przez zastosowanie rozszerzenia binarnego algebry su(3), konstruujemy model Kobayashiego-Masukawy.

PL ISSN 0459-6854

B U L L E T I N

DE LA SOCIÉTÉ DES SCIENCES ET DES LETTRES DE ŁÓDŹ

2013 Vol. LXIII

Recherches sur les déformations no. 2

pp. 97–106

Małgorzata Antoszewska-Moneta, Józef Balcerski, Romuald Brzozowski, Kazimierz Dolecki, Tomasz Gwizdałła, Bogdan Pawłowski, and Marek Moneta

PIXE INDUCED BY MEDIUM ENERGY HEAVY IONS IN APPLICATION TO ANALYSIS OF THIN FILMS AND SUBSURFACE REGIONS

Summary

X-rays emitted during the impact of heavy ions on the surface provide not only information on atomic excitation and further recombination processes but also on elemental composition and dynamics of restructuration of the surface.

In this work the characteristic radiation emitted during the interaction of medium energy (240 keV) light and heavy ions (Ar) with Au/Si thin (10 Å) film and Au foils in various diffraction geometries were measured in order to analyse transitions between states with high quantum numbers.

Also, the *X*-radiation generated in collisions of medium energy (220 keV) heavy ions (Ar, N) with Si surface and with Fe/Si and Fe/Cu/Si thin (10 A to 50 nm) films in grazing incident-exit angle geometry were measured in time sequence in order to determine dynamics of formation of implanted-sputtered subsurface region and in order to show that the dynamics of selective surface modification (structure and composition) during implantation can *in-situ* be monitored with PIXE.

Keywords and phrases: PIXE, heavy ions, surface sputtering

1. Introduction

The term PIXE is traditionally used to describe *particle induced X-ray* emission phenomena. For this analysis usually MeV energy light ions (H and He) are used, since their impact is considered non destructive and since characteristic *X*-ray emission cross sections peak appears at these energies [1–3]. The cross section ($\sim Z_p^2$) can be considerably enlarged by the use of heavy ions (HI's), which unfortunately

deposit locally large amount of energy, thus changing surface structure [4, 5]. The surface composition is also changed due to the implantation of beam ions and selective sputtering of the surface elements. HI's produce also continuous spectrum, which intensity $\sim Z_p^2$, and their own characteristic X-rays, especially in symmetric collisions ($Z_p \approx Z_a$), which overlap spectra of X-rays coming from target species [6]. An advantage of using slow heavy ions is related to shallow penetration depth which predestinates the ions for analysis of subsurface regions and even thin films. In the latter case it is proposed to improve detection limit by the use of double grazing incidence-detection geometry suppressing bremsstrahlung and radiation from the background.

Theoretical analysis of HI X-ray production becomes complicated due to large Coulomb interaction or molecular effects. Despite the fact that the first order Approximations, such as Plane Waves Binary A., Semi-Classical A. and Binary Encounter A. were further developed by including relativistic wave functions, binding-polarisation correction, Coulomb deflection and electron exchange processes, the discrepancies between calculated and experimental cross sections remained [7].

The k-shell X-ray emission cross-section σ_x (related to the excitation cross section σ_k and to the fluorescence yield ω_k as $\sigma_x = \sigma_k * \omega_k$) can be determined through independent measurement of the X-ray intensity N_x, the ion beam flux I_p on the target and the scattering geometry $\delta\Omega$ to get

$$N_x = I_p \cdot \sigma_x \cdot \rho \cdot R \cdot e \cdot \delta\Omega/4\pi, \tag{1}$$

where: ρ is the material density, $e \approx 1$ is the X-ray energy dependent registration efficiency of the detector, $\delta\Omega/4\pi$ is the detector fractional solid angle and R is the ion energy dependent projected range of the ion in material, [8].

Taking into account that impact of HI is a destructive event, the X-rays spectra emitted by Au/Si, Fe/Si and Fe/Cu/Si thin films during the irradiation with Ar ions of the energy 200–240 keV were measured in time sequence in order to determine dynamics on the spectra accumulation and stability of the films against HI sputtering, interface mixing, implantation and creation of recoils and cascades. Also, various modification of grazing incidence–exit geometry was used

Spectra of characteristic X-rays emitted by Ar during implantation of Ar ions into Si was measured, and compared with the spectra measured with He and N ions, in order to analyse the enhancement of the inner shell ionization and estimate the Ar detection limit in dependence on energy and dose of the implanted ions. This enhancement is caused by building the molecular orbitals, when colliding particles have the similar electronic structure. Such collisions are called symmetric and were used to improve the detection limits for Fe in Si [6].

2. Experimental set-up

The Ar, N and He ions beams were accelerated by 300 kV Cockroft-Walton multiplier of the Department of Solid State Physics to an energy of 230 keV. After leaving

the acceleration tube, the beam was magnetically analysed. The ion beam current density on the sample, measured by the Faraday cup, was about 0.5 μA/cm^2. The vacuum in the reaction chamber was better than 10^{-6} hPa [9].

The 10 Å thick Cu and Fe thin films were evaporated from Knudsen cell on Si surface which was cleaned in HF at high temperature. The targets were mounted on a two axis goniometer in double alignment geometry: the incident grazing angle was fixed at $\phi_{in} \leq 5^\circ$ and the exit grazing angle was fixed at $\phi_{out} \leq 0.5^\circ$ after preliminary measurements minimizing the signal from the Si background. The PIXE X-rays spectra emitted at 90° off the ion beam direction were measured by the SDD spectrometer [10] (fwhm 120 eV@6.4 keV) placed behind a 25 μm kapton window and deconvoluted with XRF-FP and GuPIX [10,11]. Ions RBS-scattered from the surface were registered at 90° off the ion beam direction by a Si(Li) detector cooled down to ca –70°C. The data acquisition was based on CAMAC system and on SWAN-4k amplitude-analysers and analysed with SIMNRA [12] and SRIM-2008 [13].

Because in PIXE characteristic X-rays are accompanied and superimposed by continuous radiation coming from accelerated electrons and by other recombination and emission processes, the grazing incidence-exit geometry was used in order to suppress bremsstrahlung and response from deeper regions. Simulations performed with SRIM showed for instance that in the grazing incidence geometry $\phi_{in} = 5^\circ$, a 240 keV Ar ion can sputter about 30 Fe atoms (and the same amount of Au atoms). About 55% of incident Ar ions are scattered back above the Fe surface. If an incident fluence of 10^{15} Ar/cm^2 at $\phi_{in} = 5^\circ$ is assumed, a 3 nm thick layer will be sputtered from the Fe surface. This should be compared with penetration depth of 40 nm and projected range of 100 nm of the Ar ions in Fe. This means that in this geometry measured is radiation which is emitted mainly from the excited target atoms leaving the surface and from the incident ions backscattered in excited state. The remaining part of incident ions, travelling in surface layer and initializing cascades, excite atoms in the topmost thin films. Radiation from deep layers and substrate should be substantially suppressed.

3. Results and discussion

3.1. Excitation of Au M-shells induced by H, N, Ar

It is expected to get a better insight into excitation and relaxation of the most intense M X-ray transitions in Au by comparing PIXE spectra induced by MEHI with these produced by light particles of MeV energy where the relative contributions of even weaker transitions in the diagram of levels and transitions in the M-shell shown in Fig. 1 are approximately known [7].

PIXE spectra induced in collisions of 200–240 keV H, He, N and Ar ions with bulk Au and with thin film Au(10 Å)/Si(110) in various geometry were measured with SDD X-ray spectrometer. We used time sequence, in order to monitor stability of the Au surface and Au thin film against HI sputtering by measuring the X-ray signal

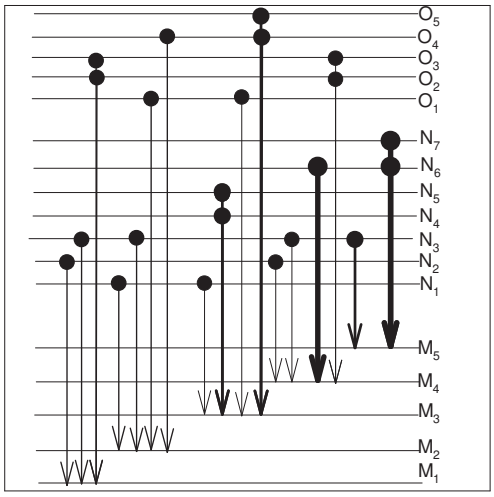

Fig. 1: Diagram of levels and most intense Au-M-X-ray transitions: $M_{45}N_{67}$,M_3N_{45}, M_3O_{45} and other shown in Fig. 2.

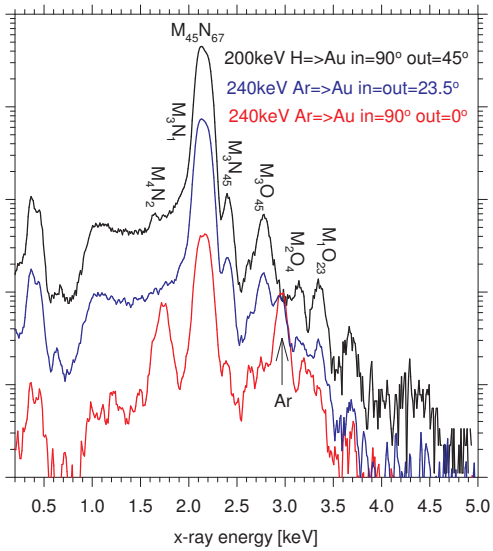

Fig. 2: Comparison of the raw PIXE spectra of Au M-lines excited by 200 keV H at normal incidence on 10 Å thin Au film and by 240 keV Ar at various incidence-exit geometry. The identification of electronic transitions is shown in Fig. 1. The SDD spectrometer with resolution 120 eV/6.4 keV was used.

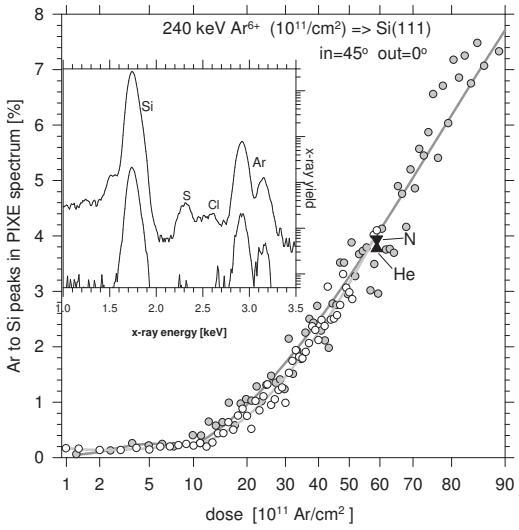

Fig. 3: Ar K-X-rays intensity in the PIXE spectrum induced during irradiation of Si wafer with 240 keV Ar^{6+}. The detection limit is about 10^{12}Ar/cm^2 $\sim$ 1.2 ppm of Ar in Si. The ratio of Ar/Si measured with 240 keV He and N ions shown with arrows. The angles are measured in respect to Si surface.

coming from the film and relating it to the signal coming from Si substrate. The time sequence was correlated with irradiation fluence and with the implanted dose. Resultant sum of spectra, which corresponded to implanted dose of 10^{13}Ar/cm^2 per each measurement, was analysed numerically. The comparison of Au M X-ray yield measured at normal H incidence and at grazing Ar exit is shown in Fig. 2. The most pronouncing feature is the maximum at 2.123 keV related to the $M_{45}N_{67}$ transition in the diagram of levels and transitions presented in Fig. 1. In the case of Au(10 Å)/Si we can see 1.74/1.83 keV $K_{\alpha/\beta}$ X-ray lines coming from Si base and 2.96/3.19 keV $K_{\alpha/\beta}$ X-lines coming from Ar ions and implanted atoms.

The PIXE spectra induced in Au with low energy Ar, reveal more subtle structure of M-shell then the similar spectra induced by 2 MeV protons [7], without requirement to apply elaborated numerical procedure for peaks deconvolution. Also, as it is shown in Fig. 2, thin films appear to enhance resolution and signal to background ratio in the spectra, as compared to spectra taken from bulk material.

3.2. Detection limit of Ar in Si with PIXE induced by Ar, N and He

We measured the characteristic X-rays emitted during the implantation of 240 keV Ar ions into Si crystal. The spectra were registered in time sequence by directing 10^{11}Ar/cm^2 ions per 300 s measurement and thus sampling the previously implanted dose. The incident ions were directed at the 45° to the surface and the emitted radiation was measured at grazing exit angle. In this geometry the penetration depth

is $L \approx 170\,\text{nm}$, the sputtering yield is $Y \approx 2.6$ Si/Ar [13] so destruction of the surface is negligible, but the RBS yield is $\approx 1\%$ [13] which means that nearly all the incident ions are implanted, thus changing subsurface composition. The spectra in the insert in Fig. 3 reveal clearly shaped Ar peaks and suppressed bremsstrahlung background. Intensity of the signal from Ar, proportional to area under Ar peak in the PIXE spectrum, related to the intensity of signal from Si were drawn in Fig. 3 as function of implanted Ar doze. There are two regions in the figure: in the first the signal from Ar fluctuates around the noise level, as if the X-rays were emitted mainly by incident ions. In the second region, above 10^{12}Ar/cm^2, the signal coming from accumulating Ar could be clearly resolved and the intensity is proportional to the implanted dose.

When colliding particles have the similar electronic structure an improvement of the detection limit, caused by building the molecular orbitals is expected. In order to check the enhancement of inner shell ionization, the spectra from the Si wafer implanted with $6 \times 10^{12}\text{Ar/cm}^2$, induced by Ar ions were compared with the spectra induced by He and N ions, as is shown with arrows and N/He symbols in Fig. 3, but no significant difference was found. This is in a contradiction to previously reported enhancement of Fe signal measured with Ni ions as compared to measurements with H and Ge ions [6].

3.3. Stability of thin film of Fe/Cu/Si and Fe/Si with PIXE induced by Ar

The HI X-ray production is accompanied by the destruction of the surface by sputtering, implantation of the beam elements and interface mixing. Thin films are particularly sensitive to HI irradiation.

In order to get some insight into the ion scattering process, the present experimental arrangement with 200 keV Ar ion beam impact on Fe/Cu/Si trilayer and on Fe/Si bilayer at 5° angles of incidence (and other appropriate initial parameters) were simulated with SRIM [13]. In the case of Fe/Cu/Si trilayer at this energy it can be, for instance, expected that about 50 % of incident Ar fluence is scattered back from this surface, whereas the remaining part is implanted as a doze. Before backscattering or stopping the ions suffer multiple collisions losing energy to electrons and creating vacancies and cascades. The sputtering yield amounts to 30 atoms Fe per incident Ar ion, which causes erosion of the topmost surface layer at a moderate speed of 3 Å layer of Fe per fluence of 10^{14}Ar/cm^2. The Cu film and Si substrate are expected to be sputtered at a negligible yield of 0.45 Cu/Ar and 0.35 Si/Ar, respectively, thus completely screened by Fe film. Although mixing of the Fe/Cu and Cu/Si interfaces within thickness of 2 Å can be observed, the extensive homogeneition of the trilayer is not expected.

The example of PIXE spectrum with Si, Fe and Cu K-shell X-rays emitted by a Fe(10 Å)/Cu(10Å)/Si(110) trilayer during irradiation with Ar ions of the energy 200 keV at $3 \times 10^{12}\text{Ar/cm}^2$, is shown in Fig. 4. The spectrum also contains K-shell

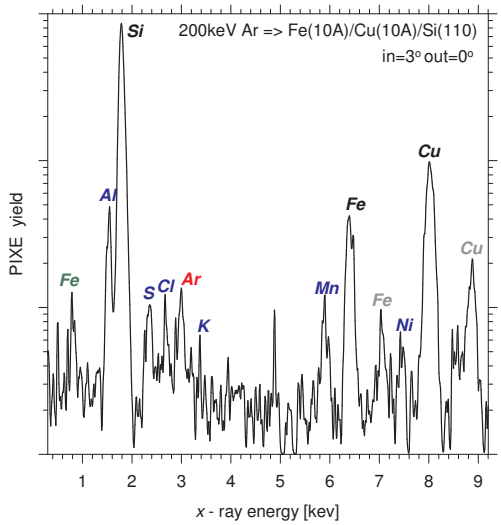

Fig. 4: PIXE spectrum induced during irradiation of Fe(10 Å) / Cu(10 Å) / Si(110) wafer with 200 keV Ar^{6+}. Implanted dose 3×10^{12}Ar/cm^2 corresponds to about 3.5 ppm of Ar. Thin films were evaporated from Knudsen cell. Thickness measured with quartz resonator. The angles $\phi_{\rm in} = 3^\circ$, $\phi_{\rm out} = 0^\circ$ are related to the surface. The SDD X-ray spectrometer with the resolution of 120 eV/6.4 keV.

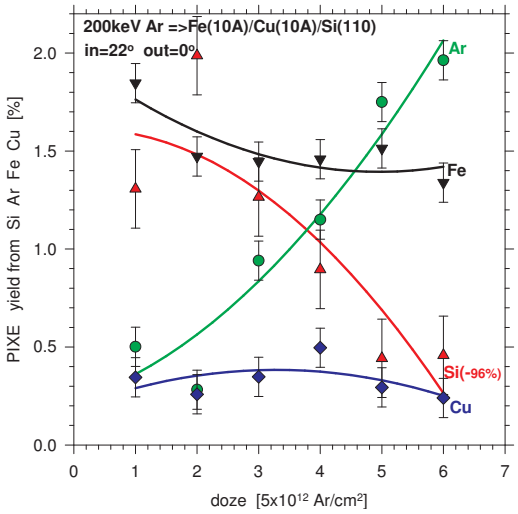

Fig. 5: Stability of Fe(10 Å)/Cu(10 Å)/Si(110) thin film against irradiation with 200 keV Ar beam at grazing-exit geometry measured by signals from Si, Ar, Fe and Cu in the PIXE spectra shown in Fig. 4. The angles are related to the surface.

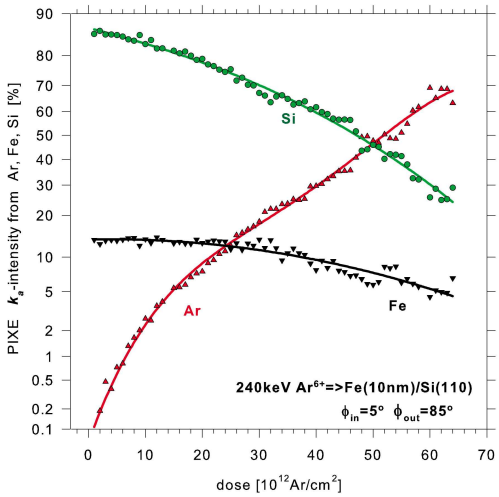

Fig. 6: Time sequence dependence of the intensity of radiation from Fe, Si and Ar in the PIXE spectra during impact of 240 keV Ar ions on Fe(10 nm)/Si(110) film. The 300 s correspond to an implanted doze of 10^{12}Ar/cm^2. The sputtering yield Y = 30 Fe/Ar, the Ar RBS = 0.53 [13]. The angles are related to the surface normal.

signal from Ar which is accumulated during irradiation and signals from trace impurities S, Cl and elements contained in environment Mn, Ni. The ions were directed at the incidence angle $\phi_{in} = 3°$ to the surface in order to have low penetration depth. Radiation was measured at the grazing exit angle in order to suppress bemsstrahlung.

In order to determine the stability of the films against HI sputtering and recoil implantation, we again used time sequence in measuring the X-ray signals coming from the films or implanted elements and related them to signal from the Si marker. The result of PIXE analysis for 200 keV Ar impact on Fe(10Å)/Cu(10 Å)/Si(110) is shown in Fig. 5. It can be seen that not only the signal from Fe and Cu decrease by a few per cent, but also the signal from Si loses intensity, whereas radiation from Ar increases nearly proportionally to the implanted dose and becomes detectable at the concentration of a few ppm, as shown also in Fig. 3. This means that use of HI at this geometry enables X-ray characterisation of the film, despite of the destructive consequences of HI impact.

Another detailed analysis of PIXE induced by Ar impact onto Fe(10 nm)/Si(110) film is shown in Fig. 6. The X-ray intensity from Ar increases monotonically and shortly becomes comparable with the decreasing signal from Si. The Ar atoms, which, in this geometry, are mainly RBS-scattered (53%), tend to be uniformly distributed in the film with a slight density increase (up to 0.06 %) in the region of mixed Fe/Si interface [13], thus intensifying radiation through molecular effect in

symmetric collisions. The vanishing radiation from Si substrate can be accepted as an effect of absorption of the radiation by additional Ar component introduced to the film. The decrease of the signal from Fe can be explained by intensive surface sputtering at this geometry $Y = 30\mathrm{Fe/Ar}$, thus thinning the film at the speed of 1 Å of Fe per $10^{12}\mathrm{Ar/cm^2}$ dose, as it is illustrated in Fig. 6.

4. Conclusions

The PIXE with MeV protons is a well-established method of nondestructive elemental analysis of films and surfaces, supported by plenty of codes which enable the analysis without standards at a moderate accuracy. The PIXE with low energy heavy ions benefits from shallow penetration depth, larger X-ray production yield and better signal to background ratio. For quantitative analysis HI PIXE requires callibration with standards and taking into account sputtering of surface during measurements, implanation of the beam ions, intensive interface mixing and the energy deposition followed by structural transformations in the surface.

References

[1] S. A. E. Johansson and J. L. Campbell, and K. G. Malmqvist, *Particle Induced X-ray Emission spectrometry (PIXE)*, WILEY 1995.

[2] S. A. E. Johansson and T. B. Johansson, Nuclear Instr. Meth. **137** (1976), 437.

[3] K. H. Ecker, H.-P. Weise, and K. L. Merkle, Microchim. Acta **133** (2000), 313.

[4] M. Toulemonde, C. Dufour, and E. Paumier, Phys. Rev. B **46** (1992), 14362.

[5] A. S. El-Said, R. Heller, W. Meissl, R. Ritter, S. Facsko, C. Lemell, B. Solleder, I. C. Gebeshuber, G. Betz, M. Toulemonde, W. Moller, J. Burgdorfer, and F. Aumayr, Phys. Rev. Lett. **100** (2008), 237601.

[6] Y. Mokuno, Y. Horino, A. Kinomura, A. Chayahara, N. Tsubouchi, and K. Fujii, Nucl. Instr. Meth. Phys. Res. B **109** (1996), 573.

[7] M. Pajek, M. Jaskóła, T. Czyżewski, L. Głowacka, D. Banaś, J. Braziewicz, W. Kretschmer, G. Lapicki, and D. Trautmann, Nucl. Instr. Meth. Phys. Res. B **150** (1999), 33.

[8] B. Pawłowski and M. Moneta, Nucl. Instr. Meth. Phys. Res. B **297** (2012), 194.

[9] M. Moneta and B. Pawłowski, Vacuum **78**, no. 2 (2005), 467.

[10] http://www.amptek.com/

[11] http://pixe.physics.uoguelph.ca/gupix/main/

[12] http://www.rzg.mpg.de/ mam/

[13] J. F. Ziegler, J. P. Biersack, and M. D. Ziegler, *The Stopping and Range of Ions in Solids*, (2008); http://www.SRIM.org

[14] G. Herzer, IEEE Trans. Magn. **26** (1990), 1397.

[15] R. Brzozowski, M. Wasiak, H. Piekarski, P. Sovak, P. Uznański, and M. Moneta, J. Alloys Comp. **470** (2009), 5.

[16] M. Moneta, R. Brzozowski, M. Wasiak, and P. Uznański, Nucl. Instr. Meth. Phys. Res. B **267** (2009), 411–414.

[17] R. Brzozowski and M. Moneta, Nucl. Instr. Meth. Phys. Res. B **297** (2012), 208.
[18] A. Puszkarz, M. Wasiak, A. Różański, P. Sovak, and M. Moneta, J. Alloys and Compounds **491** (2010), 495.

Chair of Modelling the Teaching
and Learning Processes
University of Łódź
Pomorska 149/153, PL-90-236 Łódź
Poland
e-mail: m_ateno@interia.pl

Department of Solid State Physics
University of Łódź
Pomorska 149/153, PL-90-236 Łódź
Poland

Department of Nuclear Physics
and Radiation Safety
University of Łódź
Pomorska 149/153, PL-90-236 Łódź
Poland

Presented by Marek Moneta at the Session of the Mathematical-Physical Commission of the Łódź Society of Sciences and Arts on June 18, 2013

PIXE INDUKOWANE CIĘŻKIMI JONAMI O ŚREDNIEJ ENERGII W ZASTOSOWANIU DO CIENKICH WARSTW I OBSZARÓW PODPOWIERZCHNIOWYCH

S t r e s z c z e n i e

Promieniowanie X emitowane z powierzchni bombardowanej ciężkimi jonami niesie informacje nie tylko o atomowych wzbudzeniach i następujących rekombinacjach, ale też o elementarnym składzie oraz dynamice restrukturyzacji powierzchni.

W tej pracy badano metodą PIXE cienkie warstwy Au/Si i folie Au przy pomocy jonów Ar średniej energii (240 keV) w różnej geometrii zderzeń w celu analizy przejść między stanami o wysokich liczbach kwantowych.

Badano również promieniowanie charakterystyczne generowane jonami Ar i N o energii 220 keV w interakcjach pod niewielkimi kątami $in - out$ mierzonymi do powierzchni badanego materiału, kryształu Si, warstw Fe/Si, Fe/Cu/Si, 10 Å do 50 nm, w krótkich odcinkach czasu w celu obserwacji w czasie rzeczywistym dynamiki zjawisk implantacji i rozpylania powierzchni i obszarów podpowierzchniowych oraz selektywnej modyfikacji struktury i kompozycji warstw i powierzchni.

PL ISSN 0459-6854

B U L L E T I N

DE LA SOCIÉTÉ DES SCIENCES ET DES LETTRES DE ŁÓDŹ

2013 Vol. LXIII

Recherches sur les déformations no. 2

pp. 107–128

In memory of
Professor Promarz M. Tamrazov

Krzysztof Pomorski and Przemysław Prokopow

NUMERICAL SOLUTIONS OF NEARLY TIME-INDEPENDENT GINZBURG-LANDAU EQUATION FOR VARIOUS SUPERCONDUCTING STRUCTURES

II. METHODOLOGY OF DETERMINATION VARIOUS TRANSPORT PROPERTIES OF SUPERCONDUCTING STRUCTURES FROM SOLUTIONS OF NEARLY TIME INDEPENDENT GINZBURG-LANDAU EQUATIONS

Summary

We present the new transport mechanism of vortices and quasiparticles in the structures of unconventional Josephson junction made by putting nonsuperconducting strip on the top of superconductor. The solutions of nearly time independent Ginzburg-Landau equations are used. Concept of temperature induced unconventional Josephson junctions is presented with some numerical examples.

Keywords and phrases: unconventional Josephson junction and device, TDGL relaxation algorithm, temperature induced Josephson junction, vortex and quasiparticle transport

1. Preliminaries on the existence of superconducting vortex and its basic properties

The superconducting or superfluid state is the case of macroscopic quantum phenomena and can be described by the superconducting order parameter that is complex valued scalar field $\psi(x)$. This scalar field or set of complex scalar fields (describing the distributions of order parameters) can be used in determination of electric or thermal transport properties of the system. The defects in the superconducting order parameter can occur due to the occurrence of electric and magnetic fields,

temperature gradients, non-uniform crystal lattice structure, certain geometry of the sample etc. In case of superconductors of the second kind the magnetic field of sufficient intensity can penetrate and punch the superconducting sample in certain places so the normal non-superconducting state is induced and surrounded by the superconducting state. Then non-dissipative current flows in the superconducting region around the quasinormal islands and supports the integer n number of fluxons so the total magnetic flux is $n(\hbar/2e)$, where n is positive integer number or zero. This is depicted in Fig. 1 and Fig. 2 and described for the first time by A. Abrikosov [1] by means of Ginzburg-Landau theory. More exact description of vortex is given by Bogoliubov-de Gennes theory, which points the quantization of the energetic levels inside vortex core depicted in Fig. 2. Superconducting vortex is the defect in the superconducting order parameter induced by the external magnetic field. Depending on the amount of impurities in the superconductor we can point 3 types of vortex cores as depicted in Fig. 3. The main criteria of difference between vortices is the average lifetime of coherent wavefunction of quasiparticle(s) inside core. Vortex existence and properties (as quantization of magnetic field flux) can be explained within the London, Ginzburg-Landau, Bogoliubov-de Gennes, Eilenberger, Usadel or Gorkov theory. Vortices create the static lattice if there is no external electric current flowing *via* the sample. There are various evidences of its existence. For example its existence can be explained by the heat capacity or current-voltage characteristics of the superconducting sample.

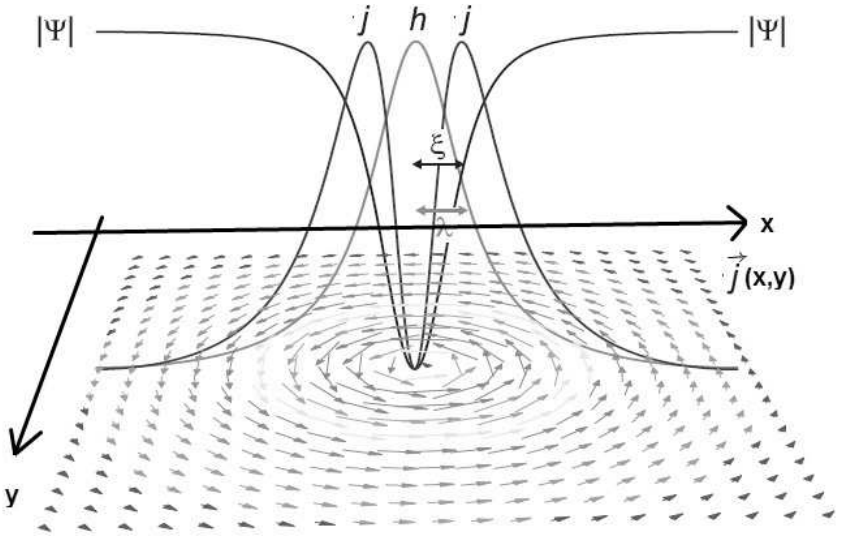

Fig. 1: Structure of the single superconducting vortex in s wave superconductor. Profiles of magnetic field $h(r)$, superconducting order parameter distribution $\psi(r)$, and superconducting current distribution $j(r)$ are given from Ginzburg-Landau theory.

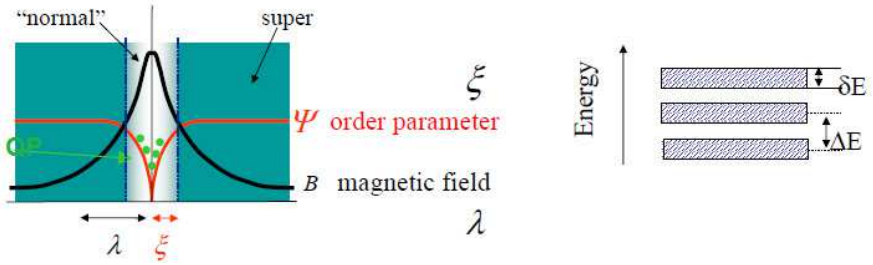

Fig. 2: Definition of superconducting vortex core and the occurrence of quantized energetic levels of quasiparticles.

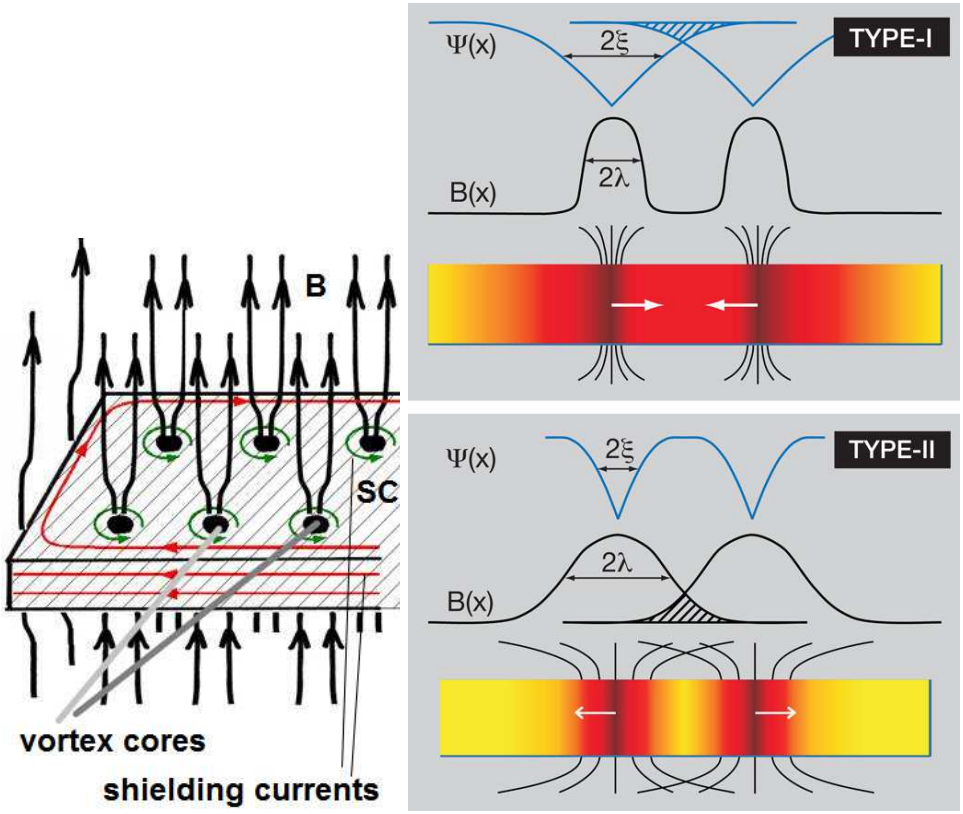

Fig. 3: Existence of vortices and interaction in superconducting vortex lattice given by [5].

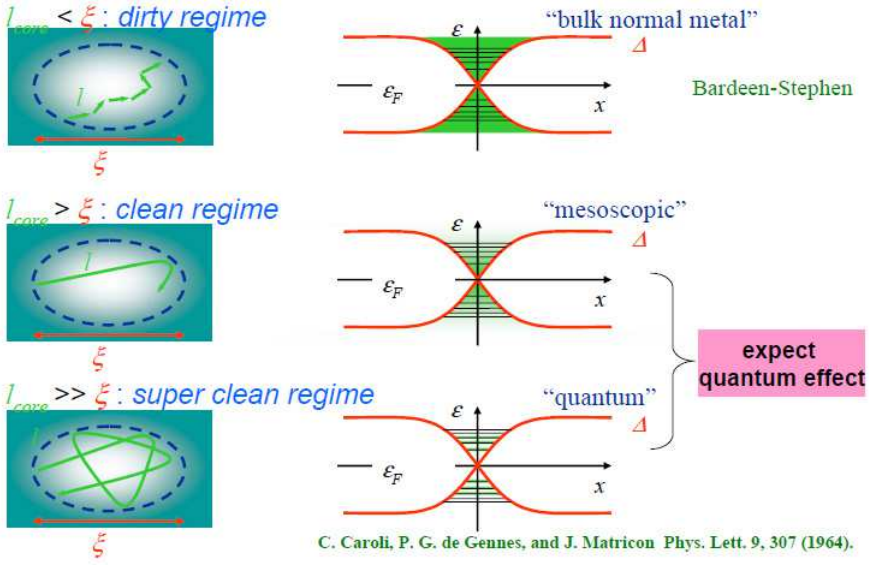

Fig. 4: Classification on superconducting vortex cores in dependence on the occurence of quantum coherence of quasiparticles.

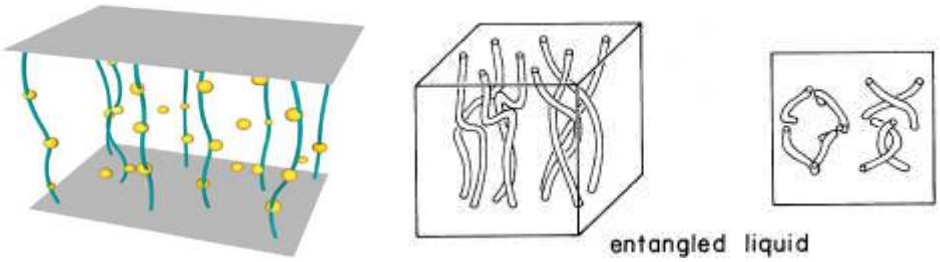

Fig. 5: View of superconductor vortex core pinned by pinning centers (left) and the case of entangled vortices (right given by G. Blatter [7]).

If we apply the external electric current vortices will start to move since there is the Lorentz force acting on the quasi-particles in its core. If we apply the external electric field to the sample vortex cores will start to move in the direction of electric field as it is the case of free electrons subjected to electric field as described by the Drude model. It should be noticed that in type II superconductors two vortices of the same helicity are repelling while in the superconductors of the I kind they are attracted. The second fact means that vortices in I kind of superconductors condense and creates the normal region, which is separated from the superconducting region on the contrary to the situation in II kind superconductors.

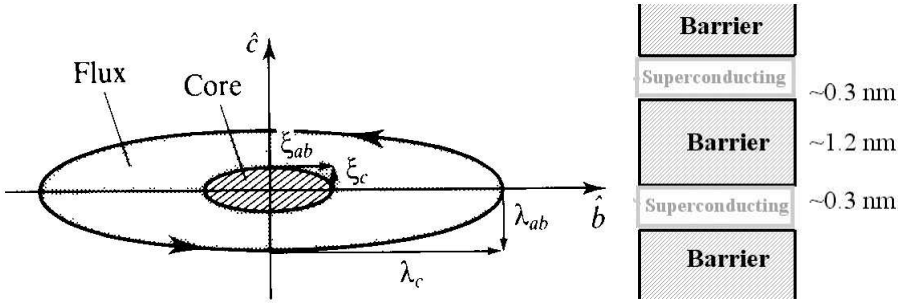

Fig. 6: Structure of Josephson vortex in d-wave superconductor and structure of d-wave superconductor as the stack of Josephson junctions.The core of vortex always tend to be localized in the nonsuperconducting or less superconducting region.

If thin superconductor sheet is placed in the strong external magnetic field perpendicular to its surface then the Ginzburg-Landau equation can be linearized. If we place the external voltage difference to the sample the superconducting vortices will start to move since electric field would act on the quasiparticle in the vortex core. By movement of quasiparticles and their interaction with with crystal lattice they will dissipate its energy. Therefore effectively the speed of vortex movement will be finite. First analytical solution describing the movement of vortex lattice was done by Schmidt in 1966. It was done for s-wave superconductor and is given below:

$$\tau(\frac{d\psi}{dt} + 2ie\psi\phi) = \xi^2(\nabla - \frac{2ie}{c}A)^2\psi + \psi \tag{1}$$

with the choice of the following vector potential $A = (0, Hx, 0)$ and $\phi = -E_x x$. TDGL equation has the solution within the first-order terms in E:

$$\psi = \sum_n C_n exp(iqn(y + \frac{cE_x t}{H}))exp(-\frac{1}{\xi^2}(x - \frac{qnc}{2eH})^2 + ie\tau E_x(x - \frac{qnc}{2eH})) \tag{2}$$

where τ is the relaxation constant, C_n-constants , H-value of magnetic field, q-value of electric charge and E_x is value of electric field in direction x. The solution corresponds to a vortex lattice moving with the velocity

$$v_y = -cE_x/H.$$

Let us consider the d-wave superconductor placed in the external magnetic field in direction parallel to the c-axis and voltage gradient present in ab plane. If the magnetic field is strong enough this linearizes the GL d-wave equation. The equation is of the form

$$-\Gamma(\frac{d}{dt}\psi + 2ie\phi\psi) = \alpha\psi + \beta|\psi|^2\psi - \gamma_{ab}(\Delta - \frac{2ie}{c}A)^2\psi - \gamma_c(\frac{d}{dz} - \frac{2ie}{c}A)^2\psi. \tag{3}$$

We assume $\phi = -E_{x'}x' - E_{y'}y'$, and $A_{y'} = Hx'$,$A_{x'} = 0$ and constant Γ. The superconducting order parameter within the first-order terms in E is of the form:

$$\psi = \sum_n C_n exp(i(qn + 2eE_{y'}t)(y' + \frac{eE_x}{H}))exp(-\frac{1}{\xi_{ab}}(x - \frac{eE_{x'}}{H}t - \frac{cqn}{2eH})^2) \times$$

$$\times exp(\Gamma\frac{\xi_{ab}}{\gamma_{ab}}(ieE_{x'}\xi_{ab} - eE_{y'}\xi(\Theta)(x - \frac{cqn}{2eH}))). \tag{4}$$

2. Vortices as particles

Superconducting vortex is the extended object which is the topological defect in the superconducting order parameter. In some sense the superconducting vortex is the excitation of the superconducting order parameter.

The superconducting vortex core from far distance can be viewed as point particle, which is subjected to various forces and whose dynamics can be modeled by the following Langevin overdamped forces:

$$\eta(x,y)\frac{d}{dt}x_i = -\frac{d}{dx_i}(U(x_i) + \sum_n W(x_i - x_j)) + F_{d,i} + \sqrt{2k_bT}\xi_i(t) + F_{M,i} \tag{5}$$

where: x_i is postion of vorticies, $\eta(x,y,t) = \eta(x,y) = c|\psi(x,y)|^2$ is viscosity of vortices, $U(x)$-substrate pinning potential, $W(x_i - x_j)$-intervortex interaction, F_d-driving force, ξ-thermal random force as described by S. Savel'ev and F. Nori and F_m-magnetic force as suggested in this work. The mass of vortex is neglected and hence the differential equations of the second order are reduced to the differential equations of the first order.

The example of vortex-vortex force F_{vv} is

$$F_{vv}(r) = \frac{\phi_0^2 s}{2\pi\mu_0\lambda^3}(\frac{\lambda}{r} - qexp(-\frac{r}{\xi})) \tag{6}$$

where r is distance between vortices, and force between vortex and pinning center F_{vp} is given as

$$F_{vp}(r_i - r_{pk}) = -f_{pv}(r_{ik}/r_p)exp(-(r_{ik}/r_p)2)r_{ik} \tag{7}$$

with

$$f_{pv} = B_2c_2(1 - \frac{B}{B_{c2}})\xi_2/\kappa_2 \tag{8}$$

where $\kappa_2 = \frac{\lambda_2}{\xi_2}$ is the ratio between the characteristic length of magnetic field decay λ and length of superconducting order parameter ξ. Numerical methodology to determine forces acting on vortices in the superconducting system is given in work [36].

Lorentz force acting on moving vortex is depicted in Fig. 16. From phenomenological point of view superconducting vortices of the same helicity are attracting from far distance and repel from the short distance. Such view is based on the fact that average magnetic flux density per certain area is constant. From microscopic point of view, the two-fluid picture is not a good approximation as stated by Eschrig, Rainer

and Sauls. The analogies between friction in the system with superconducting vortices and classical friction typical for macroscopic bodies were pointed for the first time by A. Maeda and are summarized in Table 1. In such view the superconducting vortex is treated as the particle with omission of the internal degrees of freedom that are incorporated into the description by mean field. In such case the physics of vortices can be reduced to the physics of the classically interacting particles as it is known from the theoretical mechanics. It should be noticed that the pancake vortex, which is the combination of Abrikosov and Josephson vortex as described in Fig. 13 cannot be approximated by one particle view. However the configuration of moving Josephson vortices as given by Fig. 14 and Fig. 15 can be approximated by the particle picture of vortex.

Tab. 1: Comparison and analogies between description of classical friction, vortices in superconductor in condensed systems according to A. Maeda and others.

System	Mechanical friction#1	Vortices in SC #2
Driving force F_d	Mechanical force F_d	Lorentz force *prop* to j
Static friction F_s due to	Surface roughness	Defects, impurities, disorder
Critical parameter	Maximal static friction F_s	Critical current j_c
Dynamical events	Stick-slip motion	Flux bundle motion
Static resistance	Static friction F_s	Pinning Fpinn
Thermal fluctuations	Not important	Important
History dependence	Yes	Yes
Inertia term	Important	Not important

3. Preliminaries on Josephson junction system

Josephson junction is the system of two superconductors coupling in the perturbative or nonperturbative way. One of the way to model the properties of superconducting structures is by use of Giznburg-Landau formalism. Other ways of description relies on usage of BCS theory. Quite straightforward is the description of the tunneling Josephson junction as given by A. Barone [18]. We have given the density of states on the left and right side according to formula

$$N_L(E) = N(0)/\sqrt{E^2 - \Delta^2}, N_R(E+V) = N(0)/\sqrt{(E+V)^2 - \Delta^2} \tag{9}$$

where $N(O), E, V$ and Δ are the density of states in the normal state, the energy, voltage across junction, the value of superconducting gap, respectively.

The current of quasiparticles moving from the left to the right is given as

$$I_{L\to R}(V) = A\int_{-\infty}^{+\infty} N_L(E)N_R(E+eV)(f_L(E))(1-f_R(E+eV))dE$$

and from the right to the left as

$$I_{R\to L}(V) = A\int_{-\infty}^{+\infty} N_R(E+eV)N_L(E)(1-f_L(E))(f_R(E+eV))dE.$$

The total electric current flowing from left to right is given as

$$(10)\quad I(V) = I_{L\to R} - I_{R\to L} = A\int_{-\infty}^{+\infty} N_L(E)N_R(E+eV).(f_L(E) - f_R(E+eV))dE$$

The system under the consideration is described on the left side of Fig. 7. The results of consideration can be summarized by the current-voltage characteristics given by Fig. 8.

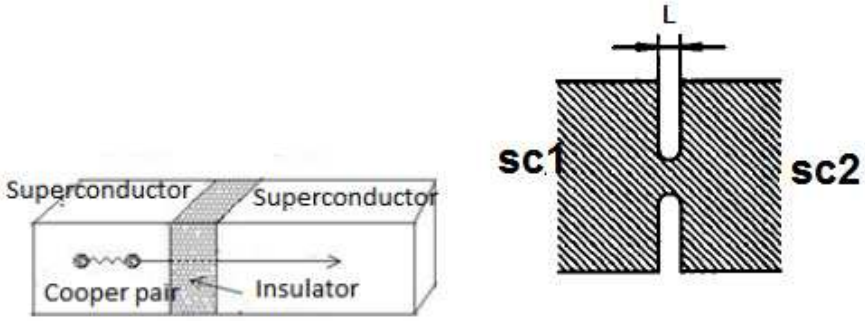

Fig. 7: General scheme of tunneling and weak link Josephson junction.

$$I_{SS} = \text{constant} \times \int_{-\infty}^{+\infty} \frac{|E|}{|E^2 - \Delta_L^2|^{1/2}} \frac{|E+eV|}{|(E+eV)^2 - \Delta_R^2|^{1/2}} [f(E) - f(E+eV)]\, dE$$

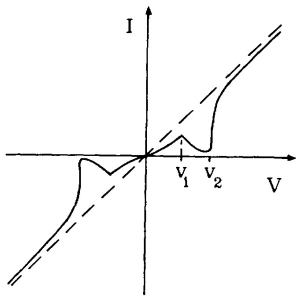

Fig. 8: Current voltage characteristic of tunneling Josephson junction as given by A. Barone [21].

4. Generalization of unconventional Josephson junction system and presence of vortices

It is possible to generalize the concept of unconventional Josephson junction or field induced Josephson junction made by putting the non-superconducting or ferromagnetic strip on the top of superconducting strip. If the superconductor has the granular structure, which is amorphous or ordered in certain regular way than we have given the array of 2 dimensional Josephsons junctions, whose superconducting order parameter is decreased by the nonsuperconducting strip. The structures under consideration are depicted in Figs. 9 and 10. There are two levels of occurrence of Josephson effect in such structures. Each superconducting granula is touching and interacting in Josephson ways with its nearest neighbours. RCSJ model describes well such interaction. Presence of nonsuperconducting bar on the top of superconducting bar generates second type of Josephson effect. One reservoir of superconducting which is the lattice of RCSJ circuits (lattice of superconducting granula) is separated into two superconducting reservoirs, which can interact in Josephson way as pointed in [2]. The presence of ferromagnetic strip can generate the Josephson vortices pinned by magnetic field as given in Figs. 11 and 12. If we have given the superconducting order parameter distribution for the case of absence of superconducting electric current flow then the small electric current flow can be treated as the perturbation of the previous solution (state). Let us assume that we have given the vortices present in the superconductor. If we sent the small external electric current and apply the weak electric field the vortices starts to move. In such case transport properties of the system can be established basing on the information on physical system with absence of transport.

With certain approximation superconducting vortices can be treated as independent particles especially in the case of not so high magnetic field.

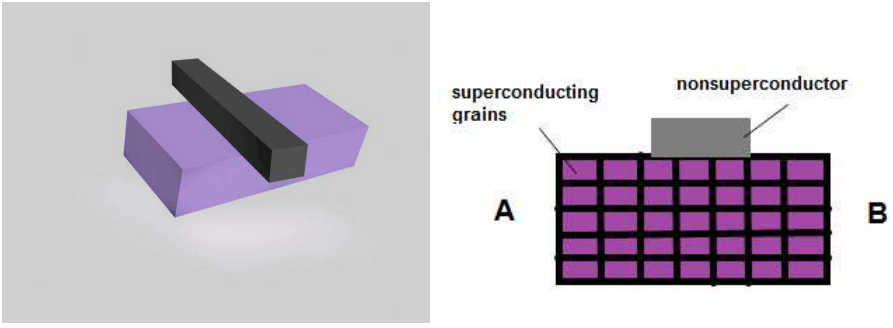

Fig. 9: Unconventional Josephson junction as the structure made by putting the nonsuperconducting material on the top of clean superconductor (Left) and granular superconductor -dirty unconventional Josephson junction (Right).

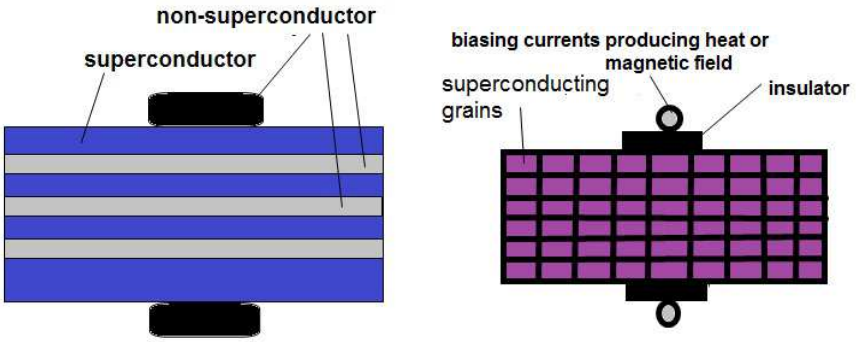

Fig. 10: Various modifications of unconventional Josephson junction concept.

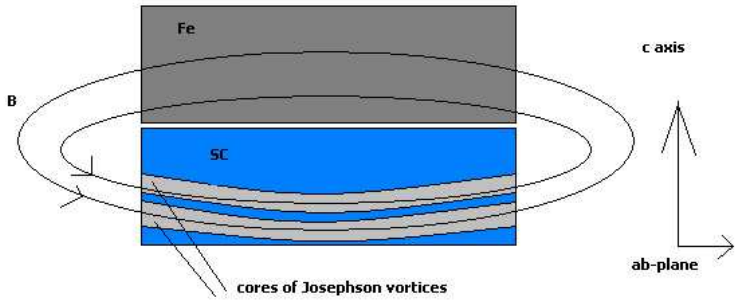

Fig. 11: Configuration of pinned vortex.

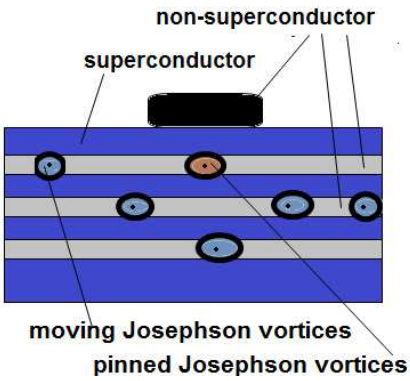

Fig. 12: Distribution of Josephson vortices movement in flow in the d-wave FIJJ with the same helicity given by [6].

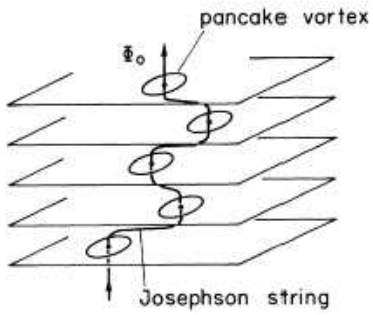

Fig. 13: Structure of pancake vortices is the combination of Abrikosov and Josephson vortices. It cannot be described by the single particle approximation.

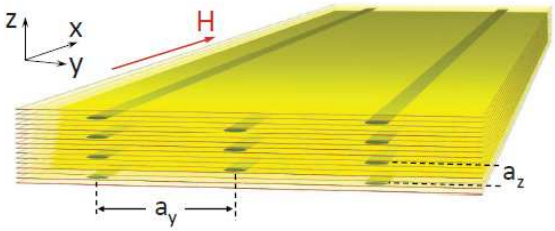

Fig. 14: The configuration of vortices. Two characteristic lengths can be identified.

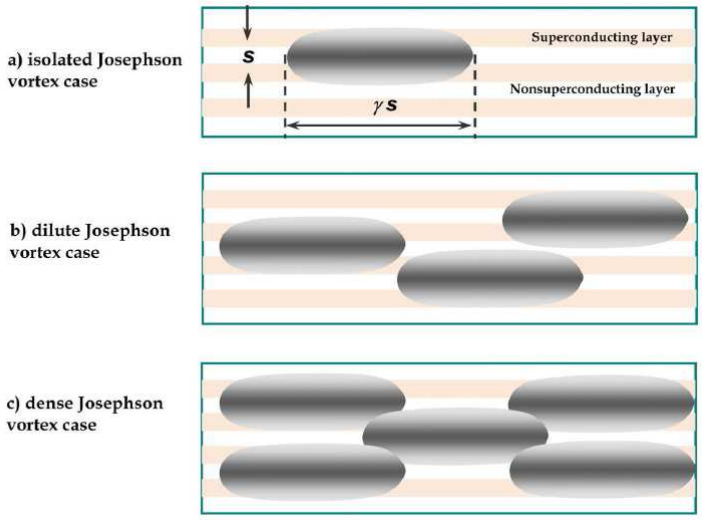

Fig. 15: Schematic drawing of distribution of Josephson vortices in *d*-wave superconductor in ac plane with a) isolated, b) dilute, and c) dense case.

5. Various aspects of vortex physics in superconducting structures

Following the thesis of Golibjon Berdiyorov [29] all vortex pinning mechanisms can be divided in two main groups: core pinning and electrodynamic pinning.

Electromagnetic pinning is due to the perturbation of the supercurrents around vortices and of their local magnetic fields by the defects, which are always present in real superconductors or can be manufactured artificially. The usual rotational symmetry of the screening currents is broken by the defects. The kinetic energy of the supercurrents can be lowered when vortices are situated on the pinning sites, resulting in an attraction between vortices and pinning centers. The important length scale here is the magnetic field penetration depth λ in the superconductor. Point defects in the lattice are the origin of the attractive interaction between superconductor vortices and defects. A local variation of T_c or κ at the defect results in a minimization of the free energy when the vortex core is located at the position of the defect. Other examples of core pinning sites are dislocations and grain boundaries. More effective core pinning is achieved when the size of the pinning site is of order ξ or λ.

Interaction of superconducting vortex with superconductor surface takes place and prevents flow of vortices out of superconductor. If we apply the magnetic field to the sample of superconductor of the second type below certain critical value the Meissner currents flowing around the sample close to its edge shield the sample from the impact of external magnetic field. If magnetic field reach certain value then there is appearance of superconducting vortices. Meissner current created by the external applied magnetic field repels a vortex from the surface as it is depicted in Fig. 17.

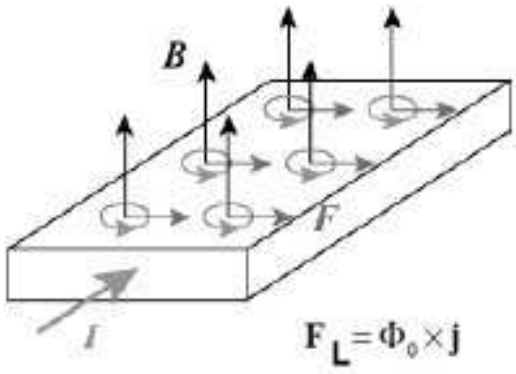

Fig. 16: Pictorial description of Lorentz force acting on superconducting vortex.

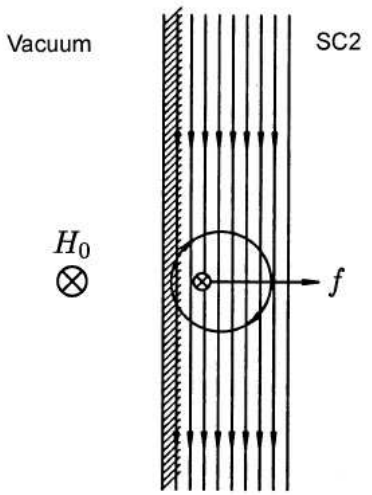

Fig. 17: Meissner current created by the external applied magnetic field repels a vortex from the surface.

5.1. Analogies and differences between theory of liquids and vortex flow in mesoscopic structures

There is certain analogy between the liquid of hard spheres and superconducting vortices in certain regime of its concenctration. Superconducting vortices of the same helicity repel each other at certain distances. If their cores happen to be in the same geometrical place two vortices can convert into one vortex with the sum of magnetic field fluxes of previous vortices, which is the integer number. Such situation does not occur in classical fluids. Vortices cannot be entangled as depicted in the Fig. 1.

5.2. Modes of vortex movement

There are 3 modes of vortex transport *via* uJJ structure: crystal, smectic and liquid phase. The criteria for the type of vortex movement are pointed by diagrams depicted in Fig. 18 and Fig. 19. Vortices can creep and can flow in dependence on the presence of pinning centers, external electric field and external electric current. Vortices can be pinned by the local pinning centers. The presence of external driving force and thermal force allows them to escape the local energetic minima.This is described by the Fig. 20 and quantified by the Arrenius law, which was pointed by Anderson-Kim theory in 1964. In accordance to this theory the average vortex velocity is given by

$$v = A\exp(-(U_0 - Fx)/kT) \tag{11}$$

where U_0 is average pinning potential and F is the external force of constant magnitude and x is the distance this force acts and A, U_0 are constants.

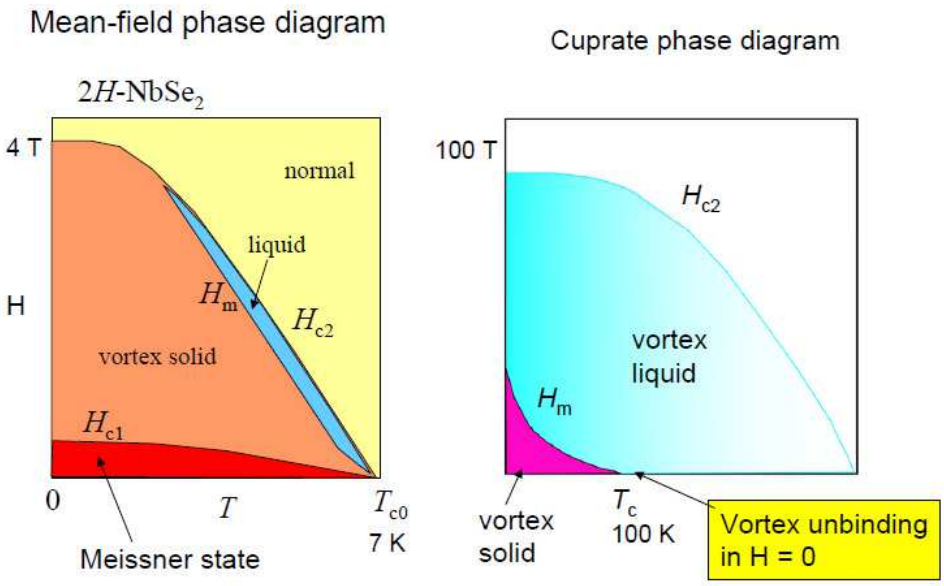

Fig. 18: Ordering of vortices in BCS (left) and high-temperature superconductor (right) in dependence on magnetic field and temperature.

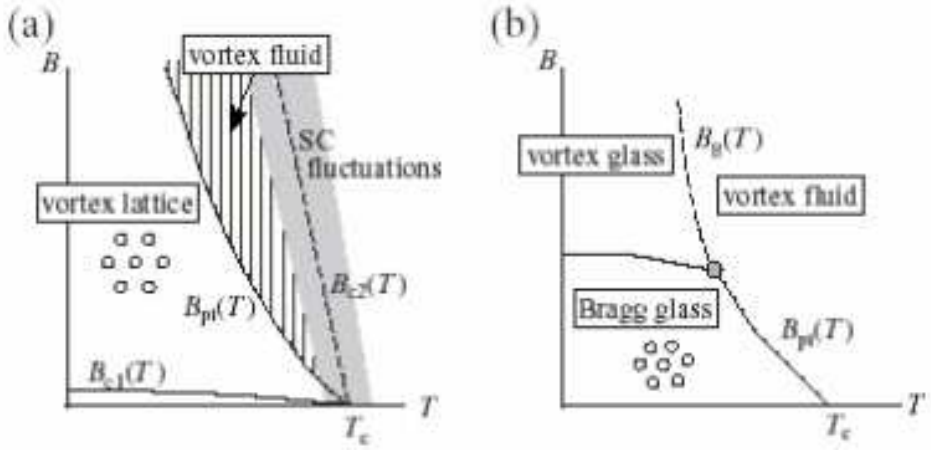

Fig. 19: The occurrence of vortex order/disorder in the case of ordered superconductor (a) and disordered superconductor (b).

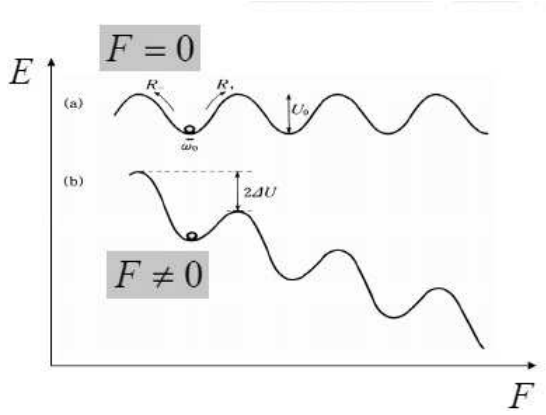

Fig. 20: Vortices can be pinned by the local pinning centers. The presence of external driving force and thermal force allows them to escape the local energetic minima after certain characteristic time.

5.3. Mathematical model of moving vortices in uJJ and FIJJ superconducting structures

We would like to describe the transport properties of vortices in the case of uJJ and FIJJ structures as depicted in Fig. 21–25. At first we need to determine the landscape of the superconducting order parameter. so the solution of Ginzburg-Landau equations is obtained by the use of relaxation method. Such approach is described in the work on 'Possible existence of field induced Josephson junctions' [2] and by work [4]. Then the superconductor is placed in the external magnetic field generating the superconducting vortices in the direction z perpendicular to surface of the uJJ structure. In the next step the small dc or ac perturbative current is send *via* the structure with certain voltage drop less than value of superconducting gap divided by electron charge. This allows for vortex movement with average constant velocity in the direction of the electric field. This movement of vortices generates the dissipation, which is reflected in the current-voltage characteristic of the sample. The contribution of vortex movement to the measured resistance can be determined. The experimental verification of the movement of vortices can be given for example by the work of A. Maeda and his collaborators described in [3].

5.4. Role of vortex pinning centers in superconductor in current-voltage characteristics

If the pinning centers are distributed in the whole superconductor structure and superconducting vortices are present it can happen that they cannot escape the pinning potential. If we apply the electric time dependent current *via* the structure or time-dependent electric field or we subject the system to microwave radiation the vortices will move around its pinning centers in the cyclic manner. In such case they

will generate the dissipation which is proportional to the time-dependent harmonic frequencies and their amplitude. Dissipation is also proportional to the number of superconducting vortices and depends on the size of superconducting core.

6. Concept of temperature induced unconventional Josephson junction

Let us consider the physical system in the same architecture as unconventional Josephson junction depicted in the left Fig. 9. It is possible to obtain the physical structure of uJJ, where nonsuperconducting strip generates heat as by sending the external dissipative current *via* this element in the proximity to uJJ or by connecting nonsuperconducting element of uJJ to the external source of heat. In such case the temperature gradient is introduced in the superconductor as it is depicted in Fig. 21 and Fig. 22. The higher the temperature the more intense reduction of the superconducting order parameter magnitude is achieved. Therefore the impact of the temperature in the reduction of superconducting order parameter is similar to the impact of the magnetic field. The temperature can be recognized as factor destroying both singlet and triplet superconducting order parameter in similar manner. This is not exactly the case of magnetic field. This is because the uniform magnetic field destroys singlet superconductivity while the triplet superconducting phase might remain unaffected. Non-uniform magnetic field destroys both singlet and triplet superconducting order parameter. On another hand in triplet superconductor the non-zero gradient of the magnetic field can destroy the order of aligned spins in one Cooper pair and thus lowering the superconducting order parameter. The concept of temperature induced Josephson effect was introduced by Zgirski and by K. Pomorski.

Currently the implementation of the temperature induced Josephson junction is being developed by simple experimental techniques as by evaporating one material on the top of another layer. In similar way as before we can construct arrays and matrices of such Josephson junctions. However it should be underlined that the usage of the Ginzburg-Landau approach in analysis of such structures is not fully justified theoretically. More sophisticated formalisms as the non-equilibrium Green function techniques needs to be employed in order to provide more rigorous form of description and extraction of the specific physical properties. Thus it is the subject of future work.

Fig. 21 describes 3 architectures of Josephson junctions. The first architecture (I) presents the concept of asymmetric temperature induced Josephson junction. The second architecture (II) describes the combination of the temperature induced Josephson junction and unconventional Josephson junction. The 3rd case (III) depicts the unconventional Josephson junction scheme, which is presented at the beginning of this paper. It should be underlined that the concept of temperature induced Josephson junction can be merged with the concept of magnetic field induced

Josephson junction or electric field induced Josephson junction. However due to the presence of the temperature gradient such structure cannot function in very low temperature range. Therefore temperature induced Josephson junction should not be used in implementation of superconducting qubit, since the heat source brings very strong decoherence to the system. It is unclear to what extent the temperature induced Josephson junction can be used in superconducting electronics. The basic expectation is that SQUID made of such structure will have very big noise component and thus its true application value is rather small. The superconducting order parameter distribution is depicted in Fig. 21 with the same $\alpha(x, y)$ distribution for 2 different topologies of the mesoscopic structure. The conclusion is that the Josephson effect is expected to occur in the given structure at certain temperature.

Another interesting case is the situation when unconventional Josephson junction is placed in external temperature gradient, but not coming from the one point like heat source as studied before. The presented solution is achieved in long times so the Ginzburg-Landau equation becomes nearly-time independent. It is conducted by considering equations of the form:

$$\alpha(x,y,t)\psi(x,y,t) + \beta(x,y)|\psi(x,y,t)|^3 - \frac{\hbar^2}{2m}\left(\frac{d^2}{dx^2} + \frac{d^2}{dy^2}\right)\psi(x,y,t) = \gamma\frac{d}{dt}\psi(x,y,t) \tag{12}$$

$$\alpha(x,y,t) = \alpha_0(x,y) + a\alpha_1(x,y)\exp(-kt) \tag{13}$$

with proper boundary conditions that are time independent.

Such dependence of the α coefficient on time reflects the reduction of the temperature gradient in time. This assumption also reflects the fact that the system evolution in time towards the equilibrium state can be represented by TDGL equation. This is by far only approximative description since the system under consideration is not exactly in equilibrium state. Although the system is in non-equilibrium state we assume that it is not far from equilibrium and its dynamics can be described by equilibrium formalism as Ginzburg-Landau formalism. More rigorous treatment requires the use of Keldysh contour or Kadanoff-Baym approach. It is by far much more complicated especially in superconducting structures and therefore it is the subject of the future work.

One of conclusions of this work is that in various studied cases the solutions of time independent GL equation are similar to the solutions of nearly time independent Ginzburg-Landau equation.

In the presented work various distributions of the superconducting order parameter in different types of superconducting structures are obtained by means of TDGL theory. Once the distribution of the superconducting order parameter by TDGL is known the determination of the transport properties with use of Bogoliubov-de Gennes equations or more advanced formalisms as Usadel or Eilenberger theory be-

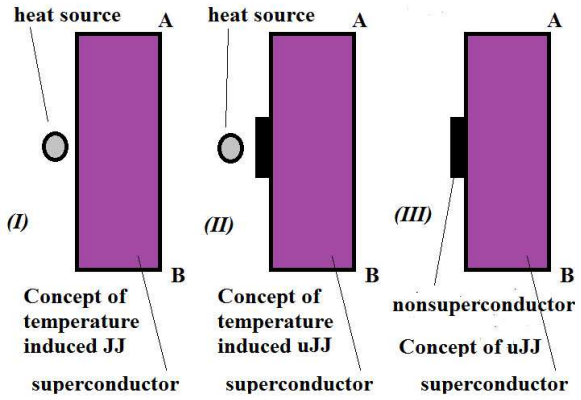

Fig. 21: 3 ways to modulate the superconducting order parameter in uJJ structures as by usage of the temperature gradient (I), combination of normal strip and the temperature gradient (II) and the usage of the non-superconducting strip (III).

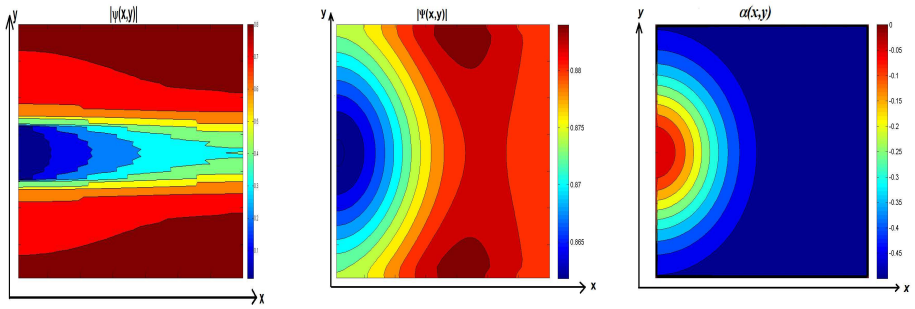

Fig. 22: Distribution of the SCOP in case of temperature induced Josephson junction (left) and uJJ with extra temperature gradient (right).

comes more realistic. The structures depicted in [37] can be studied with presented methodology.

In this work the study of unconventional Josephson junctions in *s*-wave and *d*-wave superconductors is conducted by means of nearly time independent Ginzburg-Landau formalism. Particular attention should be paid to *d*-wave superconductors and devices built of them. They have the biggest potential for applications since some of them can operate in the temperature of liquid nitrogen. The presence of nearly-time independent temperature gradients was accounted in the numerical computations. It turns out that the temperature gradient in certain situations becomes useful factor in modulation of the magnitude of the superconducting order parameter. The presence of such temperature gradient makes possible to modulate the superconducting order parameter much further as it can be achieved by use of the

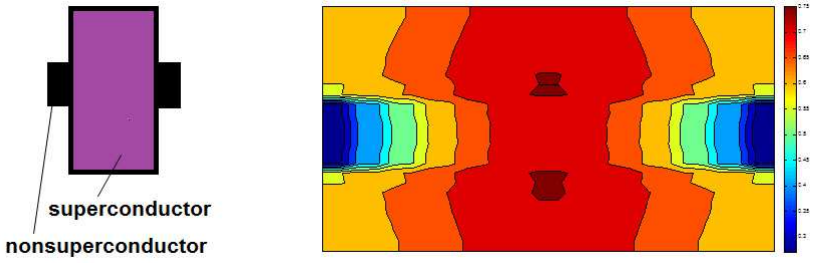

Fig. 23: Architecture and distribution of superconducting order parmeter in symmetric unconventional Josephson junction.

nonsuperconducting strip on the top of superconducting strip. To our knowledge the main idea was presented first time by Zgirski from IFPAN in Warsaw. It will also be the subject of future work.

7. Conclusion

The presented description of transport phenomena in superconductors is very phenomenological and is quasiclassical simplification of processes taking part in superconductor. However it seems to be very useful before applying the usage of Bogoliubov-de Gennes, Usadel, Eilenberger and Keldysh techniques. The experimental confirmation of the studied models of vortex transport is expected to come from Luis Gomez work, which was partly expressed in the experimental work presented in [3]. The extended calculations of transport properties of uJJ structures is needed to match the possible experimental results.

Acknowledgment

We would like to thank to professor Julian Ławrynowicz and to professor Andrzej Majhoffer and to doctor Adam Bednorz for helpful discussions and comments.

References

[1] A. A. Abrikosov, *The magnetic properties of superconducting alloys*, Journal of Physics and Chemistry of Solids **2**, no. 3 (1957), 199–208.

[2] K. Pomorski and P. Prokopow, *Possible existence of field induced Josephson junction devices*, Physica Status Solidi B **249**, no. 9(2012), 1805–1813.

[3] A. Maeda, et al., *Experimental studies to realize Josephson junctions and qubits in cuprate and Fe-based superconductors*, Journal of Superconductivity and Novel Magnetism (2010).

[4] K. Pomorski and P. Prokopow, *Towards the determination of properties of the unconventional Josephson junction made by putting non-superconducting strip on the top of superconducting strip*, Electronic Journal of Theoretical Physics **7**, no. 23 (2010), 85–121.

[5] X. B. Xu, et al., *Vortex dynamics for low-κ type-II superconductors*, Physical Review B **84**(2011).

[6] K. Pomorski, *Prediction of new physical phenomena in superconductors and superconducting structures*, Master of Science Thesis, University of Łódź (2007) (in Polish).

[7] G. Blatter, *Vortices in high-temperature superconductors*, Review of Modern Physics **66**, no. 4 (1994), 11251388.

[8] R. P. Simões, *Role of interstitial pinning in the dynamical phases of vortices in superconducting films*, Journal of Superconductivity and Novel Magnetism **26**, no. 6, (2013), 2277–2279.

[9] S. K. H. La, *Observation of thermally activated flux creep in $YBa_2Cu_3O_{7-y}$ microbridges*, Superconducting Science and Technology **11** (1998), 11771180.

[10] A. Irie and G. Oya, *Thermally assisted vortex motion in intrinsic Josephson junctions*, Journal of Physics Conference Serie **97** (2008).

[11] S. Kim, *A numerical study of steady-state vortex configurations and vortex pinning in type-II superconductors*, Texas A and M Univeristy, PhD Dissertation (2004).

[12] J. G. Bednorz, et al., *Possible high Tc superconductivity in the BaLaCuO system*, Z. Phys. **64** (1986), 189–193.

[13] E. Brandt and Shi-Ping Zhou, *Viewpoint-Attractive vortices*, Physics **2**, no. 22 (2009).

[14] Movie on youtube by Hitachi, *Movement of vortices in Niobium* (youtube movies).

[15] G. E. Volovik, *The Universe in helium droplet*, OUP, Oxford 2009.

[16] M. A. Silaev, *Self-consistent electronic structure of multiquantum vortices in superconductors at $T < T_c$*, Journal of Physics: Condensed Matter **25**, no. 22 (2013).

[17] J. Bardeen and J. Stephen, *Theory of the Motion of Vortices in Superconductors*, Physical Review **140**, no. 4A (1965), 1197–1207.

[18] N. Kopnin, Theory of Nonequilibrium superconductivity, Oxford Science Publications, Oxford 2001.

[19] J. Sosnowski, *Dynamic vortex motion in anisotropic HTc superconductors*, Materials Science-Poland **23**, no. 3 (2005), 613–624.

[20] B. D. Josephson, *Possible new effects in superconducting tunnelling*, Physical Letters **1** , no. 7 (1962), 251–253.

[21] A. Barone, G. Paterno, *Physics and Applications of the Josephson Effect*, John Wiley and Sons Inc., 1982.

[22] M. Ziese, *Percolative vortex motion in high-temperature superconductors*, Physical Review B **53**, no. 18 (1995), 12422–12429.

[23] L. Freitag, et al., *New techniques for pararell simulation of high temperature superconductors*, Proceedings of IEEE Scalable High-Performance Computing Conference, (1994), 726–733.

[24] R. P. Simões, et al., *Role of interstitial pinning in the dynamical phases of vortices in superconducting films*, Journal of Superconductivity and Novel Magnetism **26**, no. 6 (2013), 2277–2279.

[25] Y. Yamada and K. Nakajima, *RF eesponses and in-phase Josephson vortex motion in an intrinsic Josephson junction system with a periodic pinning potential*, Journal of the Korean Physical Society **48**, no. 5 (2006), 1053–1056.

[26] P. Barrozo, *Model of overdamped motion of interacting magnetic vortices through narrow superconducting channels*, Physical Review B **80**, no. 10 (2009), 104513–104517.

[27] M. A. Silaev, *Self-consistent electronic structure of multiquantum vortices in superconductors at $T < T_c$*, (2013), arxiv: 301.5909.

[28] A. E. Koshelev and M. J. W. Dodgson, *Josephson vortex lattice in layered superconductors*, (2013), arxiv:1304.6735.

[29] G. Berdiyorov, *Vortex Structure and Critical Parameters in Superconducting Thin Films with Arrays of Pinning Centers.*

[30] Y. Morita, M. Kohmoto, and K. Maki, *Aspects of a single vortex in d-wave superconductors*, International Journal of Modern Physics B (1998).

[31] C. Caroli, P. G. de Gennes, and J. Matricon, *Quasiparticle states in the vortex core*, Phys. Lett. **9** , no. 307 (1964).

[32] P. Martinoli et al., *Mean-field model of vortex motion*, Physica B **165** (1990), 166.

[33] P. W. Anderson and Y. B. Kim, *Hard superconductivity: theory of the motion of Abrikosov flux lines*, Review of Modern Physics **36**(1964).

[34] M. Nohara, M. Isshiki, F. Sakai, and H. Takagi, *Quasiparticle Density of States of Clean and Dirty s-Wave Superconductors in the Vortex State*, (1999), http://arxiv.org/abs/cond-mat/9902264v1.

[35] N. B. Kopnin and G. E. Volovik, *Flux-flow of d-wave superconductor (analytical calculation)*, Physical Review Letters **79**, no. 7 (1997), 1377–1380.

[36] V. A. Kashurnikov, A. N. Maksimova, and I. A. Rudnev, *Ferromagnetic nanoparticles as efficient bulk pinning centers in HTSC*, conference EUCAS 2013.

[37] K. Pomorski and P. Prokopow, *Perspective on basic architectures and properties of unconventional and field induced Josephson junction devices*, International Journal of Microelectronics and Computer Science (2013).

[38] C. Caroli, P. G. de Gennes, and J. Matricon, Phys. Lett. **9**, no. 307 (1964).

[39] S. Savel'ev and F. Nori, *Experimentally-realizable devices for controlling the motion of magnetic flux quanta in anisotropic superconductors*, Nature Materials **1** (2002), 179–185.

University of Warsaw
Faculty of Physics
Institute of Theoretical Physics
Hoża 69, Warsaw, Poland
and
Jagiellonian University
Institute of Physics
Reymonta 4, Kraków
Poland
e-mail: kdvpomorski@gmail.com

Computational Biomechanics Unit
The Institute of Physical
and Chemical Research (RIKEN)
2-1, Hirosawa, Wako, Saitama 351-0198
Japan
e-mail:przem@post.pl

Presented by Julian Ławrynowicz at the Session of the Mathematical-Physical Commission of the Łódź Society of Sciences and Arts on December 6, 2012

NUMERYCZNE ROZWIĄZANIA PRAWIE NIEZALEŻNYCH OD CZASU RÓWNAŃ GINZBURGA-LANDAUA DLA RÓŻNYCH NADPRZEWODZĄCYCH STRUKTUR

II. METODOLOGIA OKREŚLENIA ROZMAITYCH WŁASNOŚCI TRANSPORTU STRUKTUR NADPRZEWODZĄCYCH NA PODSTAWIE ROZWIĄZAŃ RÓWNAŃ GINZBURGA-LANDAU'A PRAWIE NIEZALEŻNYCH OD CZASU

S t r e s z c z e n i e

W pracy zaprezentowano własności transportowe układów nadprzewodzących.

Rozwiązania prawie niezależnego od czasu równania Ginzburga-Landaua w różnych nadprzewodzących strukturach jest użyte do okreslenia własności transportowych struktur nadprzewodzących. Dysypacja w takich układach jest pokazana na przykładzie ruchu kwaziczą stek i poruszania się wirów pola magnetycznego.

PL ISSN 0459-6854

B U L L E T I N

DE LA SOCIÉTÉ DES SCIENCES ET DES LETTRES DE ŁÓDŹ

2013 Vol. LXIII

Recherches sur les déformations no. 2

pp. 129–137

Agnieszka Niemczynowicz

MODEL OF COUPLED HARMONIC OSCILLATOR IN A ZWANZIG-TYPE CHAIN. MAGNON APPROACH

Summary

We sum up the problem of model of coupled harmonic oscillations in one-dimensional *finite* chain in the relation to the magnons representation. In this model we are concerned of the concept proposed by Zwanzig [7]. Therefore the aims of our paper is the effort to extend our previous work to the case describing the spin wave resonance by means of Zwanzig trajectories.

Keywords and phrases: coupled harmonic oscillation, spin wave, resonance spin wave

1. Introduction

The aims of the present paper is to continue our previous consideration [1–3] about coupled harmonic oscillator in Zwanzig - type chain from the magnons point of view.

In classical mechanics the Hamiltonian of a one-dimensional harmonic oscillator reads [4]

$$\mathcal{H} = \frac{1}{2m}p_x^2 + \frac{k}{2}x^2, \tag{1}$$

where m is the mass of the particle and k the spring constant. Classical equations describe the motion of the particle can be expressed in the terms of Hamiltonian, which are known as the Hamiltonian equations

$$\dot{p}_x = -\frac{\partial \mathcal{H}}{\partial x}, \quad \dot{x}_x = \frac{\partial \mathcal{H}}{\partial p_x}. \tag{2}$$

As usually, p_x stands for a momentum of a considered particle and x for a position, dot over the symbol denotes a time derivative.

The above mentioned the one-dimensional oscillator defines basic physical law and is useful research tool in many branches of physics, chemistry, engineering and biology [5]. Because of its mathematical simplicity, in many cases, the models are reduced to the problem of coupled oscillators.

In quantum mechanics harmonic oscillator is describe by one of the fundamental equations, namely, the Schrödinger equation, which takes the form [5]

$$\left(\frac{\hbar}{2m}\frac{d^2}{dx^2} - \frac{\omega^2}{2}x^2 + E\right)\Psi(x) = 0. \tag{3}$$

The wave function $\Psi(x)$ describes the amplitudes of harmonic oscillations and $\hbar$ stands for the Planck constant, ω denotes the basic frequency of the considered oscillator, E is energy.

Continuing our research [1–3] we study dynamical behavior between an atom and a surface represented as *a finite* linear chain of oscillators, in the terms of magnons. In our consideration we undertake formulate our problem with assumptions proposed by Zwanzig [7].

The paper is organized as follows. In Section 2 we formulate the details of our model. In Section 3 we present the extension of Zwanzig's formulae in relation to the spin waves resonance. In the next Section 4 the classical formalism is developed to spin wave resonance theory. Finally, a conclusion is given in Section 5.

2. The model

We introduce the model of the sample in the form of a ferromagnetic thin film which is described by the Hamiltonian [2]

$$\mathcal{H} = \frac{1}{2}\sum_{\nu}\frac{p_\nu^x}{m} + \frac{1}{2}\sum_{(\nu,\nu_\prime)} K\left(x_{\nu_\prime} - x_\nu\right)^2 + \sum_{\nu}\kappa_\nu x_\nu, \tag{4}$$

where K denote the harmonic forces and m is the mass of the atom localized in the position ν, κ_ν is the effective external force and the symbol $\sum_{(\,,\,)}$ denotes a sum containing each pair of atoms once only. In this model the sample is characterized by the magnetization $M(z,t)$ along the easy magnetization axes z parallel to the quantization direction. The sample is immersed in a static magnetic field $\overrightarrow{H}$ and rf alternative field h oscillating perpendicularly to $\overrightarrow{H}$.

In order to consider the magnons properties in thin film we rewrite the Hamiltonian in the terms of spin operator variables $S_\nu^x,\ S_\nu^y,\ S_\nu^z$, namely

$$\mathcal{H} = -J\sum_{(\nu,\nu')}\vec{S}_{\nu j}\vec{S}_{\nu' j} - \sum_{\nu j}A_{\nu j}^0 S_{\nu_j}^z S_{\nu_j}^z - \sum_{\nu j}A_{\nu j}^s S_{\nu j}^z - \mu_B H\sum_{\nu j}S_{\nu j}^z. \tag{5}$$

The terms of above Hamiltonian corresponding to the exchange term, the anisotropy term and the Zeeman term. The surface anisotropy is taken into account where $A_{\nu j}^0$ corresponding to the homogenous volume anisotropy and $A_{\nu j}^s$ is the surface anisotropy.

In our consideration we take into account the properties of spin waves resonance spectrum, which depends on the sample characteristics. The resonance effect in the system described by the Hamiltonian $\mathcal{H}$ and perturbed by $h(t) = Mh_0 \cos \omega t$, considered in the terms of the perturbation which influences the time-dependent solution describing the magnetization $M(t)$. The Schrödinger equations

$$i\hbar \frac{\partial \Psi}{\partial t} = (\mathcal{H} + Mh_0 \cos \omega t)\, \Psi \tag{6}$$

has no stationary solutions. In order to find solution in the form of the spin waves function we transform (6) into the interaction image. For this propose we take the wave function in the form

$$\Psi = \sum_n a_n(t) \psi_n \exp\left(-\frac{i}{\hbar} E_n t\right), \tag{7}$$

where E_n and ψ_n are the energy eigenvalues and eigenfunctions, respectively, and they are described by the Hamiltonian $\mathcal{H}$.

Next we assume that the perturbation appears only in the time interval $(0, t_0)$. This means that the boundary conditions

$$\psi_i = \psi_m \exp\left(-\frac{t}{\hbar} E_m\right), \quad \text{i. e.} \quad a_n(t) = S_{nm}, \text{ for } t < 0 \tag{8}$$

and

$$\psi_f = \sum_n a_{nm}(t) \psi_n \exp\left(-\frac{t}{\hbar} E_m\right) \text{ for } t > t_0, \tag{9}$$

which should be satisfied the probabilities $|a_{nm}(t)|^2$ of the distribution related to the finite eigenstate n.

Assuming that $\psi_f = \psi_f(m, \nu; t)$ denotes the wave function in the Zwanzig's representation, we can compere it with the nonstationary functions represented by the collection of eigenfunctions $T_{\nu\tau}$.

3. Reference to Zwanzig's formulae and their extension

The use of Zwanzig's approach to the spin waves resonance is based on the analogy between the spin operators described in the harmonic approximation and the harmonic operators which refer to the model of lattice vibrations.

Using this analogy we can see that the spin operators (the Holstein-Primakoff transformation in the harmonic approximation)

$$S_\nu^x = \sqrt{2S}(a_\nu^+ + a_\nu^-), \quad S_\nu^y = \sqrt{2S}(a_\nu^+ - a_\nu^-) \tag{10}$$

express by the magnon creation a_ν^+ and annihilation a_ν^- operators in the harmonic approximation, correspond to the lattice vibration operators, namely, the position operator

$$x_\nu = \frac{1}{2}\left(a_\nu^+ + a_\nu^-\right) \tag{11}$$

for those operator, and momentum operator

$$p_\nu = \frac{1}{2i}\left(a_\nu^+ - a_\nu^-\right) \tag{12}$$

which is canonically conjugated to x_ν. In the orginal consideration performed by Zwanzig [7] we can recall his Hamiltonian and his equation of motion for the phonon operators $x_\nu,\ p_\nu$ to (4) and

$$\frac{dx_\nu}{d\tau} = \frac{1}{2}u_{2\nu}, \quad \text{and} \quad x_\nu - x_{\nu+1} = u_{2\nu+1} \quad \text{for} \quad \nu = 1, 2, ..., n \tag{13}$$

with

$$\frac{dx_0}{d\tau} = \frac{1}{2\mu}F(x_1), \quad \frac{dx_2}{d\tau} = -\frac{1}{2\mu}[F(x_1) + x_3] \tag{14}$$

and the resolvent function [7]

$$\Theta(z,\tau) = \left[\exp\frac{1}{2}\left(z - \frac{1}{z}\right)\right]\Theta(z,0)$$

$$+\frac{1}{2}\int_0^\tau \left\{\left(1-z^2\right)u_1(s) + zu_0(s) - z^2F[u_1(s)]\right\}\left[\exp\frac{1}{2}\left(z-\frac{1}{z}\right)(\tau - s)\right]ds, \tag{15}$$

where $\tau = 2\omega t$ and F denote the reduced time and reduced force, respectively.

In the case of application of Zwanzig model we start from the Hamiltonian (5) for magnons described by the equation of motion

$$\begin{aligned} -i\hbar\frac{\partial}{\partial t}S_\nu^y &= [S_x^\nu, \mathcal{H}],\ \nu = 1, 2, ..., n, \\ \hbar\frac{\partial}{\partial t}S_\nu^x &= [S_y^\nu, \mathcal{H}],\ \nu = 1, 2, ..., n, \end{aligned} \tag{16}$$

and (cf. [3] for details):

$$B'(\nu)T_{qr} - 2JS\sum_{\nu'\neq\nu} T_{q\nu'} = \omega_q T_{q\nu} \tag{17}$$

so that, in particular

$$B(\nu)T_{q\nu} + 2JS\left[z(\nu)T_{q\nu} - \sum_{\nu'\neq\nu} T_{q\nu'}\right] = \omega_\nu T_{q\nu} \tag{18}$$

with

$$B(\nu) := \mu_B H + A_\nu^s + 2A_\nu^0 + 2JSz(\nu),$$

which agrees with the formulae (15) in [8]. Here we assume that $r = (\nu, \overrightarrow{j}) \mapsto q = (\tau, \overrightarrow{k})$, and $A_r^0 = A^0$ corresponding to the homogenous *volume anisotropy* A^0, A_r^s corresponding to the *surface anisotropy* A_ν^s. In general the relation (18) has to be replaced by

$$B(r)T_{\tau k\nu j} + 2JS\left[z(r)T_{\tau k\nu j} - \sum_{\nu' j' \neq \nu j}\sum_{\nu,j} T_{\tau k\nu' j'}\right] = \omega_{\tau k}T_{\tau k\nu j}. \tag{19}$$

The equation (18) is linear with respect to T_{qr} and describes spin waves propagating perpendicularly to the surface. We introduce the new notation $\sum_{j'\in j}$ which means the summation with respect to the nearest planes (monoatomic layers) and modify (18) and (19) correspondingly $\nu - 1$, $\nu = \nu'$, $\nu + 1$. Therefore

$$\begin{aligned} T_q = \left(\sum_r T_{qr}\right)^2 &= \left[\sum_\nu \sum_j T^k_{\nu\tau} e^{i(k_x j_x + k_y j_y)}\right]^2 \\ &= \left(\sum_\nu T^k_{\nu\tau} \sum_{j_x} e^{ik_x j_x} \sum_{j_y} e^{ik_y j_y}\right)^2 = \left(\sum_\nu T^{(k=0)}_{\nu\tau}\right)^2 \end{aligned} \tag{20}$$

for $\vec{q} = (\tau, \vec{k})$, and $\vec{r} = (\nu, \vec{j})$.

4. Reference to classical approach and its modification

Taking into account the properties of spin waves we can see that [11–16]:

(i) Spin waves resonance exist for the waves perpendicular to the surface ($k = 0$);

(ii) Spin waves resonance is an event existing in a thin film only. We have to take into account the surfaces and the fact that the event applies to thin films only;

(iii) In consequence the difference equation for T_{qr} is subjected to boundary conditions which also determine eigenfrequencies ω_r for $\omega(\tau, h) = \omega(\tau, 0)$.

Let us take the case where the surface anisotropy $A^s_\nu = A^s(\delta_{1\nu} + \delta_{n\nu})$ and $A^0_\nu = A^0$ is the volume anisotropy for $r = \nu = 1, 2, ..., n$, we have the following system of equations

$$\begin{aligned} 2JST_{1\tau} &:= B(1)T_{1\tau} \quad \text{for} \quad \nu = 1, \\ 2JST_{\nu\tau} &:= B(\nu)T_{\nu\tau} \quad \text{for} \quad \nu \in (2, n-1), \\ 2JST_{n\tau} &:= -B(n)T_{n\tau} \quad \text{for} \quad \nu = n. \end{aligned}$$

Taking into account the above properties of the spin waves frequencies spectrum we consider the dispersion relation in the case of the *sc* lattice with the surface orientation *sc*(100). In this case the equation (17) can be written in the form

$$2JST_{\nu\tau} - (\mu_B H + 2SA^0 - \omega_\tau)T_{\nu\tau} = 0 \tag{21}$$

with the boundary condition

$$\begin{aligned} 2JST_{1\tau} - (\mu_B H + 2SA^0 + A^s - \omega_\tau)T_{1\tau} = 0 \\ 2JST_{n\tau} + (\mu_B H + 2SA^0 + A^s - \omega_\tau)T_{n\tau} = 0. \end{aligned}$$

We introduce the notation

$$y_\tau = (\mu_B H + 2SA^0 - \omega_\tau)/2JS$$

so that

$$\begin{aligned} &T_{1\tau} - \left(y_\tau + \frac{A^s}{2JS}\right) T_{1\tau} = 0, \\ &T_{\nu\tau} - y_\tau T_{\nu\tau} = 0 \ \text{ for } \ \nu = 2, ..., n-1, \\ &T_{n\tau} + \left(y_\tau + \frac{A^s}{2JS}\right) T_{n\tau} = 0. \end{aligned} \tag{22}$$

We can see that the resonance frequency ω_{res} can be tuned by eigenfrequency value characterized by the variable representing the constant magnetic field H instead of tuning by means of the frequency of the alternative field

$$h = h^0 \exp(i\omega_{\text{res}} t). \tag{23}$$

The eigenvalues of the frequency spectrum depend on the surface parameter A^s introduced by the boundary condition. In other words, it means that the anisotropy parameter defined the resonance frequency: $\omega(\tau, 0) = \omega_{\text{res}}$. The reduced surface anisotropy parameter is

$$A = A^s/2JS. \tag{24}$$

If, in particular, $A = 0$, then the analog (22) reads

$$\begin{aligned} &T_{1\tau} = T_{2\tau} - T_{1\tau} = y_\tau T_{1\tau} \\ &T_{\nu\tau} = y_\tau T_{\nu\tau} \ \text{ for } \ \nu = 1, 2, ..., n-1, \\ &T_{n\tau} = T_{n\tau} - T_{n-1,\tau} = y_\tau T_{n\tau}. \end{aligned} \tag{25}$$

Finally we can write

$$\omega_\tau = \mu_B H + 2SA^0 + 2JS(2 - y_\tau), \tag{26}$$

where y_τ is a solution of the equation (the Corciovei-type determinant [9])

$$\begin{vmatrix} y_\tau & 1 & 0 & \dots \\ 1 & y_\tau & 1 & \dots \\ 0 & 1 & y_\tau & \dots \\ \dots & \dots & \dots & \dots \\ \dots & \dots & 1 & y_\tau \end{vmatrix} = 0. \tag{27}$$

We can see that, in accordance with the formulae (20) we have

$$T_{\nu\tau} = N_\tau \cos\left[\alpha_\tau\left(\nu - \frac{n+1}{2}\right) + \frac{\pi(\tau-1)}{2}\right],$$

$$T_\tau = \frac{\left\{\sum\limits_\nu \cos\left[\alpha_\tau\left(\nu - \frac{n+1}{2}\right) + \frac{\pi(\tau-1)}{2}\right]\right\}^2}{\sum\limits_\nu \cos^2\left[\alpha_\tau\left(\nu - \frac{n+1}{2}\right) + \frac{\pi(\tau-1)}{2}\right]},$$

$$N_\tau^2 = \frac{1}{\sum\limits_\nu \cos^2\left[\alpha_\tau\left(\nu - \frac{n+1}{2}\right) + \frac{\pi(\tau-1)}{2}\right]}, \tag{28}$$

$$T_{\nu\tau} - \frac{\mu_B H + 2SA^0 - \omega_\tau}{2JS} T_{\nu\tau} = 0,$$

$$y_\tau = \frac{\mu_B H + 2SA^0 - \omega_\tau}{2JS} T_{\nu\tau},$$

so that

$$(A - 2\cos\alpha_\tau)\cos\left[\alpha_\tau\left(\nu - \frac{n+1}{2}\right) + \frac{\pi(\tau-1)}{2}\right]$$

$$+ \cos\left[\left(2 - \frac{n+1}{2}\right) + \frac{\pi(\tau-1)}{2}\right] = 0. \tag{29}$$

The system of equation (25) can be rearange to a recurrence form

$$T_{2\tau} + (1 - 2\cos\alpha_\tau) = 0, \tag{30}$$

$$T_{\nu+1,\tau} + T_{\nu-1,\tau} - 2\cos\alpha_\tau T_{\nu,\tau} = 0 \quad \text{for} \quad \nu = 2, ..., n-1, \tag{31}$$

$$T_{\nu-1,\tau} + (1 - 2\cos\alpha_\tau) T_{n\tau} = 0. \tag{32}$$

and

$$T_{\nu\tau} = (-1)^\tau T_{n+1-\nu,\tau}, \tag{33}$$

$$T_{n-1,\tau} = (-1)^\tau T_{2\tau}, \tag{34}$$

$$T_{n\tau} = (-1)^\tau T_{1\tau}. \tag{35}$$

Substituting (34) and (35) in (32) we obtain (30), so we have the symmetry with respect to the both boundary surfaces.

In general we solve the system

$$T_{2\tau} + (1 + A^s - 2\cos\alpha_\tau T_{1\tau}) = 0,$$

$$T_{\nu\tau} = N_\tau \cos\left[\alpha_\tau\left(\nu - \frac{n+1}{2} + \frac{\pi}{2}(\tau-1)\right)\right],$$

where A^s is the surface anisotropy and N_τ corresponds to the amplitude of a spin wave. Taking into account the above relations and $\beta_\tau = -\frac{n+1}{2}\alpha_\tau + \frac{\pi}{2}(\tau - 1)$ we obtain

$$N_\tau = \left[\sum_\nu \cos^2(\alpha_\tau \nu + \beta_\tau)\right]^{-\frac{1}{2}},$$

and

$$\omega_\tau = \mu_B H + 2SA^0 + 2JS(1 - \cos\alpha_\tau).$$

In particular, $\omega_\tau = \mu_B H + 2SA^0 + JS\alpha_\tau^2$. For examples and experimental data we refer to [10].

5. Conclusions

The quantum mechanics adsorption approach leads to the basic form for the adsorption formulae

$$P_{0\to 1}^{\tau h} = \frac{2\pi}{\hbar}|\langle 1_{\tau h}|W|0\rangle|^2 \delta(\omega_{\tau h} - \omega_{\text{res}}) \tag{36}$$

where the operator W describes the interaction energy between the rf field and the magnetic moment operator

$$W = M^x(t) h_0^x \cos\omega t \tag{37}$$

with

$$M^x(t) = \mu_B \sum_{\nu_j} S_{\nu_j}^x(t) \tag{38}$$

where μ_B standing for the product of the gyromagnetic factor and the Bohr's magneton. The spin operator $S_{\nu_j}^x(t)$ is considered in its harmonic representation as the deviation from the easy magnetization direction z. For further investigation it is natural to ask, what conditions of the adsorption power function should to be fulfil in order to obtain it by means of Zwanzig's trajectories?

Acknowledgment

The author should like to express their cordial thanks to Professors Julian Ławrynowicz and Leszek Wojtczak for numerous helpful and stimulating discussions. This paper was supported by the European Union within the European Social Found.

References

[1] A. Niemczynowicz, *A model of coupled harmonic oscillator in Zwanzig-type chain. Phonon approach*, Bull. Soc. Sci. Lettres Łódź Sér. Rech. Déform. **62**, no. 1 (2012), 193.

[2] —, *The diagonal form of the Hamiltonian in a Zwanzig - type chain*, Bull. Soc. Sci. Lettres Łódź Sér. Rech. Déform. **61**, no. 3 (2011), 115.

[3] —, *On spin waves damping frequency eigenvalues*, Bull. Soc. Sci. Letters Łódź **59** Sér. Rech. Déform. **58** (2009), 111.

[4] L. D. Landau and E. M. Lifszyc, *Quantum Mechanics*, Pergamon Press, Oxford 1974.

[5] B. Gaveau, J. Ławrynowicz, and L. Wojtczak, *Solitons in Biological Membranes*, Open Sys. Inf. Dyn. **2**, no. 3 (1994), 287.

[6] A. S. Dawydow, *Quantum Mechanics*, Pergamon Press, Oxford 1965.

[7] R. W. Zwanzig, *Collision of a gas atom with a cold surface*, J. Chem. Phys. **32**, no. 4 (1960), 1173.

[8] L. Wojtczak and H. Gärtner, *Spin wave resonance profiles*, in: Deformations of Mathematical Structures II (ed. by J. Ławrynowicz), Kluwer Academic, Dordrecht (1994) 307.

[9] A. Corciovei, *Spin-wave theory of ferromagnetic thin films*, Phys. Rev. **130** (1963), 2223.

[10] H. Gärtner and H. K. Schmidt, Z. für Angew. Phys. **20** (1966), 344.

[11] H. Puszkarski, *Surface spin waves in hexagonal cobalt thin films*, Phys. Stat. Sol. (b) **22** (1967), 355.

[12] —, *Spin wave resonance in hexagonal cobalt thin film*, Acta Phys. Polon. **33** (1968), 769.

[13] —, *Surface mode and uniform mode in spin-wave resonance*, ibid. **38** (1970), K145.

[14] —, *Quantum theory of spin wave resonance in thin ferromagnetic films. Part I*, ibid. A **38** (1970), 217.

[15] —, *Quantum theory of spin wave resonance in thin ferromagnetic films. Part II*, ibid. A **38** (1970), 899.

[16] —, *Theory of surface states in spin wave resonance*, Progr. Surf. Sci. **9** (1979), 191.

Department of Relativity Physics
University of Warmia and Mazury in Olsztyn
Słoneczna 54, PL-10-710 Olsztyn,
Poland

Presented by Julian Ławrynowicz at the Session of the Mathematical-Physical Commission of the Łódź Society of Sciences and Arts on November 24, 2011

MODEL OSCYLATORA HARMONICZNEGO W ŁAŃCUCHU ATOMÓW TYPU ZWANZIGA. PODEJŚCIE MAGNONOWE

S t r e s z c z e n i e

Głównym celem tej pracy jest próba rozszerzenia wyniku poprzednich prac [1–3] na przypadek metody opisującej rezonans fal spinowych w terminach trajektorii Zwanziga. W pracy przedstawiono model oscylatora harmonicznego w jednowymiarowym skończonym łańcuchu typu Zwanziga w ujęciu magnonowym. Równania ruchu wyprowadzone za pomocą formalizmu Hamiltona opisują zachowanie się spinów zlokalizowanych w węzłach sieci w odniesieniu do teorii fal spinowych.

Rapporteurs – Referees

Richard A. Carhart (Chicago)
Fray de Landa Castillo Alvarado (México, D.F.)
Stancho Dimiev (Sofia)
Pierre Dolbeault (Paris)
Paweł Domański (Poznań)
Mohamed Saladin El Nashie (London)
Jerzy Grzybowski (Poznań)
Ryszard Jajte (Łódź)
Zbigniew Jakubowski (Łódź)
Tomasz Kapitaniak (Łódź)
Grzegorz Karwasz (Toruń)
Leopold Koczan (Lublin)
Dominique Lambert (Namur)
Andrzej Łuczak (Łódź)
Cecylia Malinowska-Adamska (Łódź)
Stefano Marchiafava (Roma)
Andrzej Michalski (Lublin)
Leon Mikołajczyk (Łódź)
Yuval Ne'eman (Haifa)
Adam Paszkiewicz (Łódź)
Krzysztof Podlaski (Łódź)
Yaroslav G. Prytula (Kyiv)
Henryk Puszkarski (Poznań)
Jakub Rembieliński (Łódź)
Carlos Rentería Marcos (México, D.F.)
Lino F. Reséndis Ocampo (México, D.F.)
Stanisław Romanowski (Łódź)
Monica Roşiu (Craiova)
Jerzy Rutkowski (Łódź)
Ken-Ichi Sakan (Osaka)
Hideo Shimada (Sapporo)
Józef Siciak (Kraków)
Józef Szudy (Toruń)
Luis Manuel Tovar Sánchez (México, D.F.)
Francesco Succi (Roma)
Massimo Vaccaro (Salerno)
Anna Urbaniak-Kucharczyk (Łódź)
Włodzimierz Waliszewski (Łódź)
Grzegorz Wiatrowski (Łódź)
Władysław Wilczyński (Łódź)
Hassan Zahouani (Font Romeu)
Lawrence Zalcman (Ramat-Gan)
Natalia Zorii (Kyiv)

CONTENU DU VOLUME LXIII, no. 3